

# Modeling three dimensional waves over topography



**David Eugenio Andrade Pérez**

Advisor: Prof. Dr. André Nachbin

Instituto Nacional de Matemática Pura e Aplicada

This dissertation is submitted for the degree of  
*Doctor of Philosophy*

March 2016

## **Acknowledgements**

The author gratefully acknowledges financial support from the following agencies: Conselho Nacional de Desenvolvimento Científico e Tecnológico CNPq and Agência Nacional do Petróleo ANP. The author also acknowledges IMPA for their investment in the computer cluster Tsunami3 and Tsunami4 where our computations were made.

# Table of contents

<b>List of figures</b>	<b>v</b>
<b>1 Water Waves</b>	<b>1</b>
1.1 Objectives and applications . . . . .	1
1.2 Background . . . . .	2
1.3 Mathematical Framework . . . . .	4
1.3.1 Flat Bottom Case . . . . .	5
1.3.2 Uneven Bottom Case . . . . .	7
1.4 Non-Local Formulation . . . . .	7
1.4.1 Solving Laplace's Equation . . . . .	8
1.5 Time evolution equations . . . . .	11
1.6 Scaling . . . . .	11
<b>2 Two Dimensional Simulations</b>	<b>13</b>
2.1 Periodic Non-Local Formulation . . . . .	13
2.1.1 Spectral O.D.E's . . . . .	15
2.2 Algorithm one . . . . .	16
2.2.1 Benchmarking the two dimensional case . . . . .	18
2.2.2 Simulation set up . . . . .	19
2.3 Bragg Resonance . . . . .	21
2.3.1 Simulation Set Up . . . . .	22
2.3.2 Fast Varying Periodic Topographies . . . . .	25
2.4 Ill-condition of the Numerical Scheme . . . . .	26
2.4.1 Reducing the number of equations . . . . .	29
2.4.2 Algorithm two . . . . .	31
2.4.3 Simulation set up . . . . .	33

---

<b>3</b>	<b>Three Dimensional Simulations</b>	<b>37</b>
3.1	Construction of the operator . . . . .	37
3.1.1	Spectral O.D.E's . . . . .	39
3.2	Algorithm three . . . . .	40
3.3	Refraction . . . . .	44
3.3.1	Convex lens . . . . .	45
3.3.2	Concave lens . . . . .	49
3.3.3	Ray Tracing . . . . .	50
<b>4</b>	<b>Related problems</b>	<b>63</b>
4.1	A Three Dimensional Boussinesq System with Topography . . . . .	63
4.2	The Bouncing Droplet Problem . . . . .	71
<b>5</b>	<b>Conclusions and Future Research</b>	<b>75</b>
5.1	Conclusions . . . . .	75
5.2	Future research. . . . .	76
5.2.1	Open questions . . . . .	76
	<b>References</b>	<b>78</b>
	<b>Appendix A</b>	<b>80</b>

# List of figures

2.1	Evolution of the velocity potential after 12 units of time. The solid line is the solution computed with the Non-Local Method and the crosses were computed with the Conformal Method. . . . .	20
2.2	Simulation at $t = 4.5$ . The underwater sine function oscillates three times per unit distance. . . . .	23
2.3	The red curves correspond to the reflected wave and its Fourier transform at $t = 4.5$ . The Blue lines correspond to the transmitted wave at $t = 4.5$ . . . .	24
2.4	Simulation at $t = 4.5$ . The underwater sine function oscillates five times per unit distance. . . . .	25
2.5	The red curves correspond to the reflected wave and its Fourier transform at $t = 4.5$ . The Blue lines correspond to the transmitted wave at $t = 4.5$ . . . .	26
2.6	Simulation at $t = 4.5$ . The underwater sine function oscillates twelve times per unit distance. . . . .	27
2.7	Red curve: Simulation without the topography. Blue curve: Actual simulation. Green curve: Simulation over the envelope of the bottom. . . . .	28
2.8	Relative errors between the Non-Local method and the Conformal method. The horizontal line represents error threshold 1%. The red point corresponds to the simulation with the smallest $N$ that satisfies $\text{sech}(2\pi N\mu/L_x)^2 < 10^{-10}$ . The vertical axis is on a logarithmic scale. . . . .	34
3.1	A Gaussian pulse over a trapezoid in the $\mu = 0.05$ regime. . . . .	43
3.2	Upper Figure: A Gaussian plane wave over a circular mountain in the $\mu = 0.1$ regime. Lower Figure: configuration of the underwater mountain. Only the central slice is shown. . . . .	46
3.3	Evolution of a Gaussian pulse over a Luneburg lens with parameters $\alpha = 1.22$ and height 0.4, in the $\mu = 0.1$ regime, at times $t = 3.1, 8.6, 13.6$ and 17. . .	55

3.4	Evolution of a Gaussian pulse over a Luneburg lens with parameters $\alpha = 0.8$ and height 0.52, in the $\mu = 0.1$ regime, at times $t = 3.1, 8.6, 13.6$ and 17. Note the strong focusing effect with the wave peaking in the third graph. . .	56
3.5	Evolution of a Gaussian pulse over a Parabolic lens with radius 4 and height 0.4, in the $\mu = 0.1$ regime, at times $t = 3.1, 8.6, 13.6$ and 17. . . . .	57
3.6	Evolution of a Gaussian pulse over a Parabolic lens with radius 4 and height 0.52, in the $\mu = 0.1$ regime, at times $t = 3.1, 8.6, 13.6$ and 17. . . . .	58
3.7	Evolution of a Gaussian pulse over a negative Luneburg lens with parameters $\alpha = 0.8$ and depth 1.48, in the $\mu = 0.1$ regime, at times $t = 3.1, 8.6, 13.6$ and 17. . . . .	59
3.8	Evolution of a Gaussian pulse over a negative Parabolic lens with radius 4 and depth 1.48, in the $\mu = 0.1$ regime, at times $t = 3.1, 8.6, 13.6$ and 17. .	60
3.9	Evolution of a Gaussian pulse over a Luneburg lens with parameters $\alpha = 0.8$ and height 0.52, in the $\mu = 0.1$ regime, at time 8.6. The black lines correspond to the rays. Notice that the rays are orthogonal to the level lines.	61
3.10	Evolution of a Gaussian pulse over a Luneburg lens with parameters $\alpha = 0.8$ and height 0.52, in the $\mu = 0.1$ regime, at time 13.6 . The black lines correspond to the rays. Notice that the wave field focuses on top of the point where the rays meet. . . . .	62
4.1	A walker in the $(2, 1)^2$ mode for $\Gamma = 3.5$ . . . . .	74
4.2	A walker in the $(2, 1)^2$ mode for $\Gamma = 3.8$ . . . . .	74

# Chapter 1

## Water Wave Equations

### 1.1 Objectives and applications

Water waves is an area in Fluid Dynamics and in Partial Differential Equations that is a great source of problems. Namely new applications arise together with new theoretical challenges as well as new numerical modeling. This work makes use of a new non-local formulation of the water wave problem which has never been explored before in its full capacity. Namely for a three dimensional (3D) dispersive wave problem in a variable depth configuration. We have well defined applications in mind which are outlined below. These consider three dimensional potential theory problems with linear dispersive water waves in the presence of quite general topographies.

Milewski [18] presented a Fourier based formulation for the 3D (potential theory/incompressible, irrotational) nonlinear water wave problem. The formulation is similar to the more recent work by Ablowitz, Fokas and Muslimani [1]. As an application Milewski explored computationally a reduced (Benney-Luke) long wave (weakly dispersive) model in which expansions and truncations are performed with the Fourier operators. This work revisits Milewski's [18] formulation for a fully general linear dispersive wave in the presence of highly variable topography.

Mathematically speaking our contribution regards the construction of a Dirichlet-to-Neumann operator (DtN) in the form of a matrix decomposition. For the linear wave problem this operator is defined along the undisturbed free surface ensuring that Dirichlet data of a 3D harmonic function is mapped onto its compatible Neumann data, without ever discretizing the fluid bulk. To the best of our knowledge this is the first characterization of a DtN operator in 3D in the presence of a highly variable topography, namely a highly variable boundary. In other words we obtain a DtN operator which has a spatial dependence, a mathematical object that has never been fully characterized in Analysis. Hopefully this work will call attention

for further research in Analysis. Through this DtN operator the 3D problem is reduced to a 2D problem along the free surface. The operator carries information from the vertical structure of the fluid domain. This is very interesting for simulations and therefore for many applications.

The applications we have in mind are waves in coastal regions and their interaction with large amplitude features of the topography. In 2D Nachbin [21, 13] has used successfully conformal mapping in the regime of rapidly varying depth features. This is a challenging domain configuration for the present non-local formulation. Therefore we choose some 2D cases with rapidly varying periodic topography to benchmark our DtN matrix decomposition scheme. The agreement with the conformal mapping technique is very good. Note that conformal mapping is restricted to 2D problems and therefore our new formulation is more far reaching. We then follow to explore the DtN operator in 3D with large amplitude depth variations that act as a “wave lens” focusing or defocusing wave energy. The expected (approximate) behavior is known in terms of Ray Theory.

A further application we have in mind is the problem of bouncing droplets on the surface of a vibrating fluid [19]. We have explored this formulation in the flat bottom regime, showing that the Faraday threshold and other bifurcation regimes are in a good range when compared to [19]. We plan to add topography in the future and study computationally problems related to tunneling, wave-droplet reflection on walls as well as wave-droplet dynamics through slits.

We have also deduced a Boussinesq system starting with a 3D potential theory formulation. The topography is in a 1D ridge-like configuration, say parallel to the coastline. We use conformal mapping to flatten the topography but since the problem is 3D the Laplacian is no longer invariant under the change of coordinates. A weakly nonlinear weakly dispersive asymptotic approximation is performed leading to a novel variable coefficient Boussinesq system along the 2D free surface. In the future we intend to explore this system numerically and compare it (in the linear regime) with the non-local formulation presented here. In certain regimes of the topography and the wave, we believe that this new Boussinesq system might be accurate and more efficient than the non-local model.

## 1.2 Background

The aim of this thesis is the study of wave propagation on the surface of a fluid such as water. This is a longstanding source of mathematical models and an active research field ever since the 19<sup>th</sup> century.

When it comes to the study of the motion of waves on the surface of a fluid one of the best known models is given by potential theory equations (1.1). In Whitham [25] is presented

a derivation of this model out of physical considerations:

$$\begin{aligned}
\Delta\varphi &= 0 \text{ in } -h < z < \eta(x,y). \\
\frac{\partial\varphi}{\partial\vec{n}} &= 0, \text{ on } z = -h. \\
\frac{\partial\eta}{\partial t} &= \frac{\partial\varphi}{\partial z} - \frac{\partial\varphi}{\partial x} \frac{\partial\eta}{\partial x} - \frac{\partial\varphi}{\partial y} \frac{\partial\eta}{\partial y}, \text{ on } z = \eta(x,y). \\
\frac{\partial\varphi}{\partial t} &= -g\eta - \frac{1}{2} \left( \frac{\partial\varphi^2}{\partial x} + \frac{\partial\varphi^2}{\partial y} + \frac{\partial\varphi^2}{\partial z} \right), \text{ on } z = \eta(x,y).
\end{aligned} \tag{1.1}$$

We have a three dimensional coordinate system in which  $z$  is in the vertical direction.

These equations model the motion of an inviscid and incompressible fluid of constant density and temperature whose flow is always irrotational and flows within the gravitational field of the earth.

These equations have two variables  $\eta$  and  $\varphi$ .  $\eta(x,y,t_0)$  denotes the surface height from the rest position of the fluid at the point  $(x,y)$  at time  $t_0$ , whereas the function  $\varphi(x,y,z,t_0)$ , known as the velocity potential, has the property that its gradient at the point  $(x,y,z)$  at time  $t_0$  gives the velocity vector of the fluid at that point.

From the mathematical point of view Potential Theory forms a *well posed* system. This means that existence, uniqueness and a continuous dependence between the solution and its initial data holds. In other words, it is always possible to determine how the fluid motion will be provided some given initial conditions. This is very important for it grants that our model in principle works (existence, uniqueness and continuous dependence). This important property was proved by Lannes [16] and Wu [27].

Despite the fact that a solution of (1.1) exists it is a challenging problem to actually compute a solution out of some given initial data. This is why we restricted even further to the linearized version of the system (1.1). The linearized system is the following:

$$\begin{aligned}
\Delta\varphi &= 0 \text{ in } -h < z < 0. \\
\frac{\partial\varphi}{\partial\vec{n}} &= 0, \text{ on } z = -h. \\
\frac{\partial\eta}{\partial t} &= \frac{\partial\varphi}{\partial z}, \text{ on } z = 0. \\
\frac{\partial\varphi}{\partial t} &= -g\eta, \text{ on } z = 0.
\end{aligned} \tag{1.2}$$

This system has to be supplemented with an initial wave profile  $\eta_0$  and an initial velocity potential  $\varphi_0$ .

The system (1.2) is the cornerstone of this work, and before we go any further we explore the mathematical properties and general facts of this system.

### 1.3 Mathematical Framework

The surface wave on top of the fluid is, at a first glance, a mere reflection of the more complex dynamics within the fluid. The dynamics inside the fluid are harder to grasp due to its three dimensionality. Nevertheless anything that happens inside the fluid produces a trace in the surface wave above it, and any change in the surface wave entails a change in the fluid motion beneath it.

What potential theory states is that there exists a correspondence between the motion of the surface wave and the motion of the fluid itself. Thus by studying the wave we are studying the whole fluid simultaneously.

The mathematical structure behind such a correspondence is hidden in an elliptic boundary value problem. In this section we will give a survey of the abstract properties of the elliptic boundary value problem. All the statements and results were proved by Lannes in [16].

Let

$$b(x, y) = -h - H(x, y), \quad x, y \in \mathbb{R},$$

be a  $\mathcal{C}^\infty$  parametrization of the bottom of the channel, and define

$$\Omega = \{(x, y, z) \in \mathbb{R}^3 \mid b(x, y) < z < 0\},$$

to be the fluid domain. We make the following assumptions on the function  $H$ :

$$|H(x, y)| < c < h, \quad |H_x(x, y)| < d \quad \text{and} \quad |H_y(x, y)| < d. \quad (1.3)$$

This means that no islands nor beaches exists inside the fluid domain and we rule out for example, vertical walls, as underwater obstacles. However we do not assume any further restrictions on the constant  $c$  and  $d$ .

Associated with the fluid domain we have the following elliptic boundary value problem:

$$\begin{aligned} \Delta \varphi &= 0 \quad \text{in} \quad -b(x, y) < z < 0. \\ \frac{\partial \varphi}{\partial \vec{n}} &= 0, \quad \text{on} \quad z = -b(x, y). \\ \varphi(x, y, 0) &= q(x, y), \quad \text{on} \quad z = 0. \end{aligned} \quad (1.4)$$

The problem consists in finding a harmonic function  $\varphi$  from its known boundary data at  $z = 0$ , namely the value of the function  $q$ , and from the Neumann boundary condition at the bottom.

The first important result that we borrow from [16] concerns the existence of solutions to (1.4). The result is very precise and it is given in terms of the Sobolev spaces  $H^k$  defined in Evans, see, [11]. The result states that for every  $k \in \mathbb{N}$  a solution  $\varphi$  of (1.4) exists provided that  $q \in H^{k+3/2}(\mathbb{R}^2)$  and in that case  $\varphi \in H^{k+2}(\Omega)$ . Notice the gain of  $1/2$  derivative from  $k + 3/2$  of the boundary value function  $q$  to  $k + 2$  of the corresponding harmonic function  $\varphi$ .

This result is very important for it allows us to define the main character of our thesis, the Dirichlet-to-Neumann operator which we define as follows.

For any  $k \in \mathbb{N}$ , given a function  $q \in H^{k+3/2}$  we denote by  $\varphi$  the corresponding solution of (1.2). The Dirichlet-to-Neumann operator is given by

$$\begin{aligned} G : H^{k+3/2}(\mathbb{R}^2) &\longrightarrow H^{k+1/2}(\mathbb{R}^2) \\ q &\longmapsto \frac{\partial \varphi}{\partial z}(x, y, 0). \end{aligned} \tag{1.5}$$

In this notation the evaluation at  $z = 0$  has to be understood as a composition with the corresponding trace operator defined in [11]. This Dirichlet-to-Neumann operator takes the Dirichlet data of the harmonic function  $\varphi$  and gives its compatible Neumann data along the surface  $z = 0$ .

In the absence of underwater topography,  $H = 0$ , we can represent this operator  $G$  as a pseudo differential operator, the computation is simple and sheds light on what is coming next.

### 1.3.1 Flat Bottom Case

We want to solve the following elliptic boundary value problem for any arbitrary  $\mathbf{k} \in \mathbb{R}^2$ .

$$\begin{aligned} \Delta \varphi &= 0 \text{ in } -h < z < 0. \\ \frac{\partial \varphi}{\partial \bar{n}} &= 0, \text{ on } z = -h. \\ \varphi(x, y, 0) &= Ae^{i\mathbf{k} \cdot \mathbf{x}}, \text{ on } z = 0. \end{aligned} \tag{1.6}$$

We use separation of variables to find a candidate for the solution.

Let  $\varphi(x, y, z) = X(x, y)Z(z)$ . A direct substitution of this ansatz into (1.6) gives

$$\frac{d^2 Z}{dz^2} = -\frac{\Delta_H X}{X} = k^2.$$

It is deduced that the horizontal function  $X$  must satisfy

$$\Delta_H X = \frac{\partial^2 X}{\partial x^2} + \frac{\partial^2 X}{\partial y^2} = -k^2 X.$$

Hence, by invoking the upper boundary condition we conclude that

$$X(x, y) = e^{i\mathbf{k}\cdot\mathbf{x}}/Z(0),$$

and so the separation constant must be  $k^2 = \|\mathbf{k}\|^2$ .

We normalize the  $Z$  function in such a way that  $Z(0) = 1$ . This normalization plus the bottom boundary condition forces the function  $Z$  to be

$$Z(z) = \frac{\cosh(k(z+h))}{\cosh(kh)}.$$

So we have that the solution to (1.6) is given by

$$\varphi(x, y, z) = A e^{i\mathbf{k}\cdot\mathbf{x}} \frac{\cosh(k(z+h))}{\cosh(kh)}.$$

In this case the trace of the vertical derivative at  $z = 0$  can be computed to give

$$G(A e^{i\mathbf{k}\cdot\mathbf{x}}) = \frac{\partial \varphi}{\partial z}(x, y, 0) = k A e^{i\mathbf{k}\cdot\mathbf{x}} \frac{\sinh(kh)}{\cosh(kh)} = A e^{i\mathbf{k}\cdot\mathbf{x}} k \tanh(kh).$$

This monochromatic example can be used to study the more general problem by means of Fourier analysis.

$$\Delta \varphi = 0 \text{ in } -h < z < 0.$$

$$\frac{\partial \varphi}{\partial \vec{n}} = 0, \text{ on } z = -h. \quad (1.7)$$

$$\varphi(x, y, 0) = q(x, y), \text{ on } z = 0.$$

Fourier analysis lets us express  $q$  as a superposition of monochromatic waves

$$q(x, y) = \int_{\mathbb{R}^2} e^{i\mathbf{k}\cdot\mathbf{x}} \hat{q}(\mathbf{k}) d\mathbf{k}.$$

And our computation already lets us compute

$$G(q) = \int_{\mathbb{R}^2} e^{i\mathbf{k}\cdot\mathbf{x}} \hat{q}(\mathbf{k}) k \tanh(kh) d\mathbf{k}, \quad (1.8)$$

where  $k = \|\mathbf{k}\|$ . This is the result that we were looking for, an expression for the trace of the vertical velocity, computable solely in terms of the value of the velocity potential at  $z = 0$ .

Some interesting properties about the operator  $G$  that can be concluded directly from its Fourier representation (1.8): self-adjointness and positivity. Moreover we can conclude that the operator has order one, meaning that its symbol grows as fast as the function  $k$  or in terms of the Sobolev spaces  $H^k$ , that the operator is bounded from  $H^k \rightarrow H^{k-1}$ .

### 1.3.2 Uneven Bottom Case

In general when  $H \neq 0$  the situation is more complex because the operator  $G$  is a pseudo differential operator and its symbol gains a dependence on the physical variable  $\mathbf{x}$ .

For this kind of operators their action on a function  $q$  in the domain of  $G$  is given by

$$(Gq)(\mathbf{x}) = \int_{\mathbb{R}^2} e^{i\mathbf{k}\cdot\mathbf{x}} \hat{q}(\mathbf{k}) \sigma(\mathbf{x}, \mathbf{k}) d\mathbf{k}, \quad \text{for every } \mathbf{x} \in \mathbb{R}^2. \quad (1.9)$$

The problem we have with this point of view is that we do not know what the symbol  $\sigma(\mathbf{x}, \mathbf{k})$  of the operator  $G$  is. In spite of that, the work of Lannes, see [16], again sheds light and proves some general properties of the operator  $G$  that are true for smooth bottom configurations.

Among these properties we have that the operator remains self-adjoint and positive, as in the flat bottom case, and it is proved that the principal symbol of the operator is  $k$ .

These facts are general properties of the operator that remain unchanged when variations in the topography are included.

This mathematical introduction suggests that the operator we want to study belongs to the realm of pseudo differential operators, but no clue about its symbol is given. This is where some Fourier representation formulas come in handy. The formulas were first derived by Milewski in [18], then taken up by by Craig, Sulem, Guyenne and Nicholls in [6] and more recently in the work of Ablowitz, Fokas and Musslimani in [1].

## 1.4 Non-Local Formulation

We are on our quest of finding the symbol of the operator Dirichlet-to-Neumann operator  $G$ . For that we introduce an alternative formulation of the problem that will give us a clue about the missing symbol of the operator. This alternative formulation follows the steps of the computation of the Dirichlet-to-Neumann operator in the flat bottom case.

### 1.4.1 Solving Laplace's Equation

We revisit the related elliptic boundary value problem:

$$\begin{aligned}\Delta\varphi &= 0 \text{ in } -b(x,y) < z < 0. \\ \frac{\partial\varphi}{\partial\vec{n}} &= 0, \text{ on } z = -b(x,y). \\ \varphi(x,y,0) &= q(x,y), \text{ on } z = 0.\end{aligned}\tag{1.10}$$

We assume that  $q(x,y)$  is a given known function. This problem is similar to (1.7) except that, because of the non trivial geometry of the domain, no close formula for the solution exists. In spite of this fact, one of the dearest techniques in PDE, separation of variables and the principle of superposition of linear waves, gives us the following ansatz for the velocity potential:

$$\varphi(\mathbf{x},z) = \int_{\mathbf{k}\in\mathbb{R}^2} e^{i\mathbf{k}\cdot\mathbf{x}} \left[ \hat{f}(\mathbf{k}) \frac{\cosh(k(z+h))}{\cosh(kh)} + \hat{g}(\mathbf{k}) \frac{\sinh(k(z+h))}{k \cosh(kh)} \right] d\mathbf{k}.\tag{1.11}$$

We are following the steps of what we did in (1.7). First notice that each element in the integrand is a solution of Laplace's equation in free space with periodic boundary conditions in both  $x$  and  $y$  directions. Thus equation (1.11) consists of a superposition of basic solutions and by linearity of the problem it represents a harmonic function.

In the representation formula (1.11) there are two sets of coefficients given by  $\hat{f}(\mathbf{k})$  and  $\hat{g}(\mathbf{k})$  which play the role of Fourier coefficients in a Fourier expansion. This coefficients are related to the boundary conditions, for instance, when the coefficients  $\hat{f}(\mathbf{k})$  vanish

$$\varphi(\mathbf{x},-h) = \int_{\mathbf{k}\in\mathbb{R}^2} e^{i\mathbf{k}\cdot\mathbf{x}} \left[ \hat{g}(\mathbf{k}) \frac{\sinh(0)}{k \cosh(kh)} \right] d\mathbf{k} = 0,$$

the velocity potential satisfies a zero Dirichlet boundary condition at the bottom  $z = -h$ .

On the other hand when the set of coefficients  $\hat{g}(\mathbf{k})$  vanish the velocity potential satisfies a zero Neumann boundary condition at  $z = -h$  as the following computation shows

$$\varphi_z(\mathbf{x},-h) = \int_{\mathbf{k}\in\mathbb{R}^2} e^{i\mathbf{k}\cdot\mathbf{x}} \left[ \hat{f}(\mathbf{k}) \frac{k \sinh(0)}{\cosh(kh)} \right] d\mathbf{k} = 0.$$

Moreover along the free surface  $z = 0$ , we recover formula (1.8), since

$$\varphi_z(\mathbf{x},0) = \int_{\mathbf{k}\in\mathbb{R}^2} e^{i\mathbf{k}\cdot\mathbf{x}} \left[ \hat{f}(\mathbf{k}) \frac{k \sinh(kh)}{\cosh(kh)} \right] d\mathbf{k} = \int_{\mathbf{k}\in\mathbb{R}^2} e^{i\mathbf{k}\cdot\mathbf{x}} \hat{f}(\mathbf{k}) k \tanh(kh) d\mathbf{k}.$$

Because the bottom boundary condition of problem (1.10) must be satisfied along the bottom surface  $z = -h - H(x, y)$  we must take into account the contribution given by both the  $\hat{f}(\mathbf{k})$  and the  $\hat{g}(\mathbf{k})$  in the representation for the velocity potential  $\varphi$ .

In order to determine the value of the coefficients we invoke the boundary conditions of the problem. First, along the free surface  $z = 0$  we must have that

$$\varphi(\mathbf{x}, 0) = q(\mathbf{x}), \quad \text{for } \mathbf{x} \in \mathbb{R}^2,$$

so that in Fourier space the upper boundary condition becomes:

$$\hat{q}(\mathbf{k}) = \hat{\varphi}(\mathbf{k}, 0) = \hat{f}(\mathbf{k}) + \hat{g}(\mathbf{k}) \frac{\tanh(kh)}{k}, \quad \text{for } \mathbf{k} \in \mathbb{R}^2. \quad (1.12)$$

Replacing  $\hat{f}$  in (1.11) and differentiating under the integral sign yields the following formula for the bottom boundary condition:

$$\begin{aligned} \int_{\mathbf{k} \in \mathbb{R}^2} \hat{q}(\mathbf{k}) \nabla \cdot \left[ e^{i\mathbf{k} \cdot \mathbf{x}} \frac{\sinh(kH)}{\cosh(kh)} \frac{\mathbf{k}}{k} \right] d\mathbf{k} = \\ = \int_{\mathbf{k} \in \mathbb{R}^2} \hat{g}(\mathbf{k}) \nabla \cdot \left[ e^{i\mathbf{k} \cdot \mathbf{x}} \frac{\cosh(k(h+H))}{\cosh^2(kh)} \frac{\mathbf{k}}{k^2} \right] d\mathbf{k}. \end{aligned} \quad (1.13)$$

This equation linearly relates the given function  $\hat{q}(\mathbf{k})$  with the unknown coefficients  $\hat{g}(\mathbf{k})$ .

Differentiating  $\varphi$  with respect to  $z$  and evaluating at  $z = 0$  gives the following representation formula

$$\varphi_z(\mathbf{x}, 0) = \int_{\mathbf{k} \in \mathbb{R}^2} e^{i\mathbf{k} \cdot \mathbf{x}} [\hat{f}(\mathbf{k}) k \tanh(kh) + \hat{g}(\mathbf{k})] d\mathbf{k}.$$

Inserting the corresponding expressions for  $\hat{f}$ , we get that

$$\varphi_z(\mathbf{x}, 0) = \int_{\mathbf{k} \in \mathbb{R}^2} e^{i\mathbf{k} \cdot \mathbf{x}} [\hat{q}(\mathbf{k}) k \tanh(kh) + \hat{g}(\mathbf{k}) \operatorname{sech}^2(kh)] d\mathbf{k}, \quad (1.14)$$

where  $\hat{g}(\mathbf{k})$  is given implicitly by (1.13). This is the non-local formulation of the problem and it was first derived by Milewski in [18] in 1996.

In view of the theoretical results of [16] this formulation is remarkable. Formula (1.14) already displays a pseudo-differential operator of order one, the  $k \tanh(kh)$  term, plus a perturbation given by the set of coefficients  $\hat{g}(\mathbf{k})$ . This  $\hat{g}(\mathbf{k})$  is the missing part of the symbol of the operator  $G$  that we were looking for.

Now we define the following linear operators

$$(Aq)(\mathbf{x}) = \int_{\mathbf{k} \in \mathbb{R}^2} \hat{q}(\mathbf{k}) \nabla \cdot \left[ e^{i\mathbf{k} \cdot \mathbf{x}} \frac{\sinh(kH(x, y))}{\cosh(kh)} \frac{\mathbf{k}}{k} \right] d\mathbf{k},$$

and

$$(Bq)(\mathbf{x}) = \int_{\mathbf{k} \in \mathbb{R}^2} \hat{q}(\mathbf{k}) \nabla \cdot \left[ e^{i\mathbf{k} \cdot \mathbf{x}} \frac{\cosh(k(h + H(x, y)))}{\cosh^2(kh)} \frac{\mathbf{k}}{k^2} \right] d\mathbf{k}.$$

In terms of the operators  $A$  and  $B$  equation (1.13) becomes

$$Aq = Bg.$$

Notice that the missing terms  $\hat{g}(\mathbf{k})$  are given in an implicit way, hidden behind two pseudo-differential operators,  $A$  and  $B$ , which appear naturally as the left and right hand sides of equation (1.13) respectively.

The corresponding symbols of  $\sigma_A(x, y, D)$  of  $A$ , and  $\sigma_B(x, y, D)$  of  $B$  are ,

$$\begin{aligned} \sigma_A(x, y, D) &= -ik \frac{\sinh(kH(x, y))}{\cosh(kh)} + (\mathbf{k}_1 H_x(x, y) + \mathbf{k}_2 H_y(x, y)) \frac{\cosh(kH(x, y))}{\cosh(kh)}, \\ \sigma_B(x, y, D) &= -i \frac{\cosh(k(h + H(x, y)))}{\cosh^2(kh)} \\ &\quad + (\mathbf{k}_1 H_x(x, y) + \mathbf{k}_2 H_y(x, y)) \frac{\sinh(k(h + H(x, y)))}{\cosh^2(kh)}. \end{aligned} \quad (1.15)$$

There is a technical detail here worth noticing. The variable depth function always satisfies that  $|H(x, y)| < c < h$ , for a constant  $c$ . This assumption, plus the boundedness on the derivatives of  $H$ , makes that both symbols are bounded functions of  $x, y$  and  $\mathbf{k}$ . In other words the pseudo differential operators  $A$  and  $B$  are of order zero. This highlights the theoretical result of [16] that principal symbol of the Dirichlet-to-Neumann operator is of order one, and topographic effects account for a zero order perturbation.

The second important technical detail is that the pseudo-differential operator  $B$  is in fact invertible. This is an important contribution proved by Craig, Sulem, Guyenne and Nicholls in [6].

To summarize things up, we began this section looking for a symbol of the operator  $G$  but what we found was that the operator is given by the flat bottom Dirichlet-to-Neumann operator plus a zeroth order perturbation given by the action of two operators  $A$  and  $B$ . The whole picture can be written as

$$G = K + B^{-1}A,$$

where  $K$  denotes the flat bottom Dirichlet-to-Neumann operator with symbol  $k \tanh kh$ . Now we proceed to the study of equations (1.2). From now on we will refer to this type of representation formula for  $G$  a non-local representation formula.

## 1.5 Time evolution equations

In this section we derive a simpler system of equations to that of (1.2). The key observation that leads to such a simplification is that the velocity potential lies completely determined by its value on the surface  $z = 0$ .

So by defining

$$q(\mathbf{x}, t) = \varphi(\mathbf{x}, 0, t),$$

we transform system (1.2) into the following much more compact system

$$\begin{aligned}\eta_t(\mathbf{x}, t) &= \varphi_z(\mathbf{x}, 0, t) = G(q), \\ q_t(\mathbf{x}, t) &= \varphi_t(\mathbf{x}, 0, t) = -g\eta.\end{aligned}\tag{1.16}$$

Notice that we have dropped two equations, the ones corresponding to the elliptic problem (1.4), and we were able to do so because the Dirichlet-to-Neumann operator takes  $q$ , determines  $\varphi$  throughout the fluid domain and computes its corresponding Neumann data  $\varphi_z$ .

So we did not drop the first and second equations of the system (1.2) but we are incorporating them inside the operator  $G$ . Another advantage of this simplification is that both  $q$  and  $\eta$  are functions defined on  $z = 0$  only, thus reducing the dynamics of the fluid to the surface. And by doing so we got rid of the vertical structure of the fluid, it is implicit in the operator  $G$ .

## 1.6 Scaling

It is convenient to have a non-dimensional form of the equations. This is accomplished by replacing all the original dependent and independent variables in (1.1) by prime variables and then the following substitution is made:

$$\begin{aligned}x' &= lx, \quad y' = ly, \quad z' = hz, \quad t' = \frac{l}{\sqrt{gh}}t, \\ \eta' &= a\eta, \quad \varphi' = a\sqrt{gh}\frac{l}{h}\varphi, \quad H' = hH.\end{aligned}\tag{1.17}$$

Then we define

$$\mu = \frac{h}{l}.$$

This transformation of the variables yields the following equation where the only parameter involved is  $\mu$ . This is the ‘‘shallowness’’ or dispersion parameter. When  $\mu \ll 1$  we are in the shallow water or long wave regime; when  $\mu \approx 1$  we are deep water or short wave regime.

The dimensionless equations are

$$\begin{aligned}
\mu^2(\varphi_{xx} + \varphi_{yy}) + \varphi_{zz} &= 0, & \text{in } -(1+H) < z < 0, \\
\frac{\partial \varphi}{\partial \vec{n}} &= 0, & \text{on } z = -(1+H), \\
\frac{\partial \eta}{\partial t} &= \frac{1}{\mu^2} \frac{\partial \varphi}{\partial z}, & \text{on } z = 0, \\
\frac{\partial \varphi}{\partial t} &= -\eta, & \text{on } z = 0.
\end{aligned} \tag{1.18}$$

And the non dimensional form of (1.16) becomes

$$\begin{aligned}
\eta_t &= \frac{1}{\mu^2} G(q), \\
q_t &= -\eta.
\end{aligned} \tag{1.19}$$

From now on we always use the dimensionless form of the equations. In our simulations we always considered the width of the initial pulse as our reference length scale  $l$  in (1.17). This yields a pulse of width one in dimensionless form.

The speed of a wave that moves over a plane of constant depth  $h$  is  $\sqrt{gh}$ . In dimensionless form this speed is always set to one. Thus if no bottom variations are present, a simulation that lasts 12 units of time for example is actually a simulation where the wave had enough time to move as much as 12 times its own initial width. This simple remark is actually useful to determine at first glance if the topography increased or not the propagation of the wave, for example.

## Summary

In this chapter we introduced the linearized potential theory equations as our model for the study of wave propagation and the Dirichlet-to-Neumann operator  $G$  as the key mathematical object behind the equations.

The formulation of the problem in Fourier space showed us a way to determine the operator  $G$  as a pseudo-differential operator of order one plus a perturbation term given by the operators  $A$  and  $B$ . Although we know that  $B$  is invertible we do not know how the inverse of  $B$  looks like, and it is our plan for the next chapter to use the computer to accomplish such a task.

# Chapter 2

## Two Dimensional Simulations

This chapter is all about numerical simulations in the case of a two dimensional fluid domain. We intend to give an algorithm that is capable of computing the operator  $G$  and thus capable of simulating the solutions of (1.19) out of an initial data. The method we propose uses the non-local formulation for the operator  $G$  and so we will simply call our method as a *non-local method*.

We have chosen to begin our simulations in the two dimensional case because we want to benchmark our method with the conformal mapping technique of Nachbin, see [21] which is only available in the two dimensional case. This is our testing ground before going to the much more interesting three dimensional case.

It is important to point out that in the literature, to the best of our knowledge, there is only one reference where a non-local method, similar to ours, has been used for the simulation of water waves over topography, it is the work of Deconinck and Vasan [24] where the wave-topography interaction is simulated in order to study what they called the inverse bathymetry problem.

Although we are not the first ones in simulating waves interacting with the topography in the two dimensional case with a non-local method the type of highly variable topographies that we are going to simulate has certainly never been tried out before.

### 2.1 Periodic Non-Local Formulation

We adapt the formulation explained in the previous chapter to the case of periodic functions, the main difference is that we use Fourier series instead of Fourier integrals and the procedure is entirely analogous. The details are as follows. We represent the velocity potential  $\varphi$  as:

$$\varphi(x, z, t) = \sum_{k \in \Lambda} e^{ikx} \left[ \hat{f}(k, t) \frac{\cosh(\mu k(z+1))}{\cosh(\mu k)} + \hat{g}(k, t) \frac{\sinh(\mu k(z+1))}{k \cosh(\mu k)} \right]. \quad (2.1)$$

This representation is similar to (1.11), however the lateral boundary conditions allows us to change the integral by a series. In this series representation  $\Lambda = (2\pi\mathbb{Z}/L_x)$  is the Fourier spectrum. The parameter  $L_x$  is the corresponding length in the horizontal direction. This representation immediately implies that

$$\hat{q}(k, t) = \hat{\varphi}(k, 0, t) = \hat{f}(k, t) + \hat{g}(k, t) \frac{\tanh(\mu k)}{k}, \quad k \in \Lambda. \quad (2.2)$$

Equation (2.2) provides a linear relation for the two unknown coefficients  $\hat{f}$  and  $\hat{g}$  at time  $t$ . The idea is to use the impermeability boundary condition to close the system for  $\hat{f}$  and  $\hat{g}$ . We drop the  $t$  dependence on the coefficients simplicity in the equations.

The impermeability boundary condition is

$$\frac{\partial \varphi}{\partial \vec{n}} = 0 \quad \text{on } z = -1 - H(x). \quad (2.3)$$

Computing all the derivatives involved in this formula gives rise to the following equation

$$0 = \sum_{k \in \Lambda} \hat{f}(k) \partial_x \left[ e^{ikx} \frac{\sinh(\mu k H(x))}{\cosh(\mu k)} \right] - \hat{g}(k) \partial_x \left[ e^{ikx} \frac{\cosh(\mu k H(x))}{k \cosh(\mu k)} \right]. \quad (2.4)$$

Substitution of (2.2) into this equation (2.4) yields

$$\begin{aligned} \sum_{k \in \Lambda} \hat{q}(k) \partial_x \left[ e^{ikx} \frac{\sinh(\mu k H(x))}{\cosh(\mu k)} \right] &= \\ &= \sum_{k \in \Lambda} \hat{g}(k) \partial_x \left[ e^{ikx} \frac{\tanh(\mu k) \sinh(\mu k H(x))}{k \cosh(\mu k)} \right] \\ &+ \sum_{k \in \Lambda} \hat{g}(k) \partial_x \left[ e^{ikx} \frac{\cosh(\mu k H(x))}{k \cosh(\mu k)} \right] \\ &= \sum_{k \in \Lambda} \hat{g}(k) \partial_x \left[ e^{ikx} \frac{\cosh(\mu k (1 + H(x)))}{k \cosh^2(\mu k)} \right]. \end{aligned} \quad (2.5)$$

These are the corresponding periodic counterparts of the operators  $A$  and  $B$ , explained in chapter one, responsible for the topographic effects, by providing the following a linear relation between  $\hat{q}$  and  $\hat{g}$ .

$$A\hat{q} = B\hat{g} \iff \hat{g} = B^{-1}A\hat{q}. \quad (2.6)$$

In Fourier space the expression that represents the operators are

$$\begin{aligned}\widehat{A}\hat{q}(l) &= \int_{T^2} e^{-ilx} \sum_{k \in \Lambda} \hat{q}(k) \partial_x \left[ e^{ikx} \frac{\sinh(\mu k H(x))}{\cosh(\mu k)} \frac{k}{k} \right] dx, \text{ for } l \in \Lambda \\ \widehat{B}\hat{q}(l) &= \int_{T^2} e^{-ilx} \sum_{k \in \Lambda} \hat{g}(k) \partial_x \left[ e^{ikx} \frac{\cosh(\mu k (1 + H(x)))}{\cosh^2(\mu k)} \frac{k}{k^2} \right] dx, \text{ for } l \in \Lambda.\end{aligned}$$

The expressions for the operators  $\widehat{A}$  and  $\widehat{B}$  can be simplified further by using integration by parts. The simplified formulas are

$$\begin{aligned}\widehat{A}\hat{q}(l) &= \sum_{k \in \Lambda} il\hat{q}(k) \int_{T^2} e^{-i(l-k)x} \left[ \frac{\sinh(\mu k H(x))}{\cosh(\mu k)} dx \right], \\ \widehat{B}\hat{g}(l) &= \sum_{k \in \Lambda} il\hat{g}(k) \int_{T^2} e^{-i(l-k)x} \left[ \frac{\cosh(\mu k (1 + H(x)))}{k \cosh^2(\mu k)} dx \right].\end{aligned}\tag{2.7}$$

Once the set of coefficients  $\hat{g}(k)$  are determined, from (2.6) the trace of the vertical velocity at  $z = 0$ , in Fourier space, is given by

$$\hat{\phi}_z(k, 0) = \widehat{G}\hat{q}(k) = \mu\hat{q}(k)k \tanh(\mu k) + \mu\hat{g}(k) \operatorname{sech}^2(\mu k).\tag{2.8}$$

This is the corresponding non-local representation formula for the Dirichlet-to-Neumann operator in the two dimensional periodic case, and deriving this formula was our purpose of this section.

### 2.1.1 Spectral O.D.E's

What we need to do now is to derive the corresponding periodic version of the system of evolution equations (1.19). This is accomplished by using a Fourier series representation,

$$\begin{aligned}\hat{\eta}_t &= \frac{1}{\mu^2} \widehat{G}\hat{q}, \\ \hat{q}_t &= -\hat{\eta}.\end{aligned}\tag{2.9}$$

We use formula (2.8) to obtain

$$\begin{aligned}\hat{\eta}_t(k) &= (\hat{q}(k)k \tanh(\mu k) + \hat{g}(k) \operatorname{sech}^2(\mu k))/\mu, \\ \hat{q}_t(k) &= -\hat{\eta}(k).\end{aligned}\tag{2.10}$$

Using the linear relation between  $\hat{q}$  and  $\hat{g}$  given in (2.6) we can close the system of equations (2.10) in terms of  $\hat{q}$  only:

$$\begin{aligned}\hat{\eta}_t(k) &= (\hat{q}(k)k \tanh(\mu k) + (\hat{B}^{-1} \hat{A} \vec{q})(k) \operatorname{sech}^2(\mu k)) / \mu, \\ \hat{q}_t(k) &= -\hat{\eta}(k).\end{aligned}\tag{2.11}$$

This system is what we were looking for. It is a system of ordinary differential equations in Fourier space, the equations are coupled by the action of the linear operators  $A$  and  $B$  and it depends only on the value of the quantities  $\eta$  and  $q$ .

### Special case $H = 0$

We consider, as a consistency test, the easiest possible case where the bottom topography is flat,  $H = 0$ . In this case equation (2.5) reads as

$$0 = \sum_{k \in \Lambda} \hat{g}(k) \partial_x \left[ e^{ikx} \frac{1}{k \cosh(\mu k)} \right] = i \sum_{k \in \Lambda} e^{ikx} \hat{g}(k) \frac{1}{\cosh(\mu k)},$$

and this can happen only if  $\hat{g}(k) = 0$  for every  $k$ . So the system (2.11) decouples and simplifies to

$$\begin{aligned}\hat{\eta}_t(k) &= (\hat{q}(k)k \tanh(\mu k)) / \mu, \\ \hat{q}_t(k) &= -\hat{\eta}(k).\end{aligned}\tag{2.12}$$

This is the classical system in Fourier space for the water wave problem. See [2].

## 2.2 Algorithm one

So far we have derived the corresponding non-local representation formulas for the water wave problem, i.e. we obtained formulas for the operators  $A$  and  $B$  responsible for the topographic effects, the operator  $G$  and the system of evolution equations in Fourier space.

Our aim is to develop an algorithm that will let us compute the operators  $\hat{A}$ ,  $\hat{B}$  and  $G$  defined in (2.9) and therefore present this novel characterization of the variable bottom DtN operator.

Devising an efficient algorithm we made an attempt to keep the number of arithmetic operations as low as possible and take advantage of the fast Fourier transform, this first version of the algorithm works on the two dimensional case and it was used to benchmark our computations.

The strategy is to compute the operators  $A$  and  $B$  first and then use them to compute the operator  $G$ . We present the full computation of the matrix that represents the operator  $\hat{A}$ , the procedure for the operator  $B$  is completely analogous.

1. Allocate a matrix  $M$  of size  $N_x \times N_x$  where  $N_x$  denotes the total number of points, and Fourier modes, in physical space.
2. When using the fast Fourier transform algorithm the set of Fourier modes available are given in the following order

$$\frac{2\pi}{L_x} \left[ 0, 1, 2, \dots, \frac{N_x}{2}, 1 - \frac{N_x}{2}, \dots, -2, -1, \right].$$

This ordering acts like a map that will tell us how allocate the entries of the matrix  $\hat{A}$ . We want the entry  $A(i, j)$  to correspond with the complex number

$$\hat{A}(l, k) = (lk) \int_0^{L_x} e^{-i(l-k)x} \frac{\sinh(\mu k H(x_m))}{k \cosh(\mu k)} dx,$$

where the Fourier mode  $l$  is the  $i$ -th wave number that appears on the ordering of the spectrum and  $k$  is the  $j$ -th wave number in the spectrum.

3. Choose a column of the matrix  $M$  and let  $k$  denote the corresponding wave number associated with that column. Fill the selected column with the numbers,

$$\frac{\sinh(\mu k H(x_m))}{k \cosh(\mu k)},$$

where  $x_m$  is the  $m$ -th physical point. The order of the elements of the column must follow the usual ordering of the point  $x_m$ .

4. Compute, using the *fft* command, the Fourier coefficients of the periodic function that is temporarily stored in the column of the matrix  $M$ . Store this column vector back in the corresponding column of the matrix  $M$ .
5. Let  $j$  denote the column of the Matrix in question, the one associated with the wave number  $k$ . Let  $m$  be the wave number associated with the  $m$  entry of the column  $j$ . Under this configuration the new value of the entry  $M(m, j)$  is given by approximately by

$$M(m, j) = N_x \int_0^{L_x} e^{-imx} \frac{\sinh(\mu k H(x))}{k \cosh(\mu k)} dx.$$

However this is no what we need. What we are looking for is that the  $M(m, j)$  entry contains the complex number

$$M(m, j) = N_x \int_0^{L_x} e^{-i(m-k)x} \frac{\sinh(\mu k H(x))}{k \cosh(\mu k)} dx.$$

Notice the difference in the complex exponential. So in order to achieve this, we permute the elements in the column until we get the desired result.

6. Repeat steps 3 to 5 in every column.
7. Finally we compute a matrix with all the possible inner products of wave number and perform an entry wise multiplication. This final matrix will represent the operator  $\hat{A}$ .
8. We repeat the same steps for the operator  $\hat{B}$ . Notice that the only difference occurs at step 3 where we must compute the following expression

$$\frac{\cosh(\mu k(1 + H(x_m)))}{k \cosh(\mu k)^2}.$$

9. This step is the most expensive one. We compute the matrix inversion and multiplication

$$\hat{B}^{-1}\hat{A}.$$

10. We need two diagonal matrices  $D_1 = \text{diag}(k \tanh(\mu k))$  and  $D_2 = \text{diag}(\text{sech}^2(\mu k))$ .

$$\hat{G} = D_1 + D_2\hat{B}^{-1}\hat{A}.$$

This algorithm is used to compute the pseudo-differential operators  $A$ ,  $B$  and  $G$  in Fourier space. However it does not involve the time step integration of the evolution equations (2.11). So in order to complete the simulation of the potential theory equations we used Matlab's numerical routine *ode113*.

### 2.2.1 Benchmarking the two dimensional case

“Del dicho al hecho hay mucho trecho”

---

Spanish proverb

When topography variations are included in equations (1.2), no close analytical formula exists for the solution. This forces us to implement a different numerical method and compare both solutions in order to benchmark our algorithm.

The chosen numerical technique, capable of simulating waves that propagate over complex topographies, has been extensively used in the literature in particular in the work of Nachbin, see for example [21]. This method makes use of the theory of complex variables and conformal mappings. It is a remarkably elegant and accurate technique, though it is constrained to the two dimensional case.

### Conformal mappings

The method of Nachbin for the water wave problem in two dimensions is based on the construction of a conformal mapping from a uniform strip onto the fluid domain. In general, the determination of the conformal mapping that flattens out the physical fluid domain is a difficult task however in the case of arbitrary polygonal topographies. This is achieved with the aid of the Schwarz-Christoffel toolbox, see Driscoll [9].

With the conformal mapping at hand the orthogonal coordinate lines in the  $\xi$ - $\zeta$  space are mapped into a family of orthogonal lines that provides a coordinate system for the fluid domain. In this curvilinear coordinates the potential theory equations are written as

$$\begin{aligned} \varphi_{\xi\xi} + \varphi_{\zeta\zeta} &= 0, \quad \text{in } -\mu < \zeta < 0. \\ \varphi_{\zeta} &= 0, \quad \text{on } \zeta = -\mu. \\ M(\xi)\eta_t - \varphi_{\zeta}/\mu &= 0, \quad \text{on } \zeta = 0. \\ \varphi_t + \eta &= 0, \quad \text{on } \zeta = 0. \end{aligned} \tag{2.13}$$

In this system of equations (2.13) the topography no longer appears in the impermeability condition but as a variable coefficient  $M(\xi)$  which is readily available from the Schwarz-Christoffel toolbox. This allows to compute the vertical velocity of the fluid  $\varphi_{\zeta}$  analytically with the aid of the flat bottom operator  $G$  as in (1.8).

#### 2.2.2 Simulation set up

In order to benchmark our method we have chosen to simulate the motion of a wave that moves in a region of constant depth and then passes over a submerge obstacle. The obstacle will be given by a trapezoid so we can use the conformal mapping technique.

We list the parameters used in the simulation:

- The length of the channel  $L_x = 20$ .
- The number of equally spaced points is  $N_x = 2^{10}$ .
- The value of the parameter  $\mu = 0.05$ .
- The final time is  $T_f = 12$ .
- The initial velocity potential is given by the equation

$$\varphi_0(x) = e^{-\frac{1}{2}\left(\frac{x-c}{\sigma}\right)^2}. \tag{2.14}$$

This Gaussian is centered at  $c = 8$  and has a standard deviation of  $\sigma = 1/6$ .

- The initial wave profile is given by

$$\hat{\eta}_0(k) = \left( \frac{k \tanh(k\mu)}{\mu} \hat{\phi}_0(k) \right). \quad (2.15)$$

This choice of initial wave allows for unidirectional dynamics in the flat bottom channel, i.e, both the wave and the potential move to the right only.

- The underwater trapezoid has height 0.4, length of the base 4 and length of top phase 3.6.
- For the time step integration we used Matlab's ode113 routine and we set the relative and absolute tolerances to  $10^{-6}$ .

The initial configuration of the experiment is shown in Figure (2.1) with the green dashed line. We show the graph of the potential only.

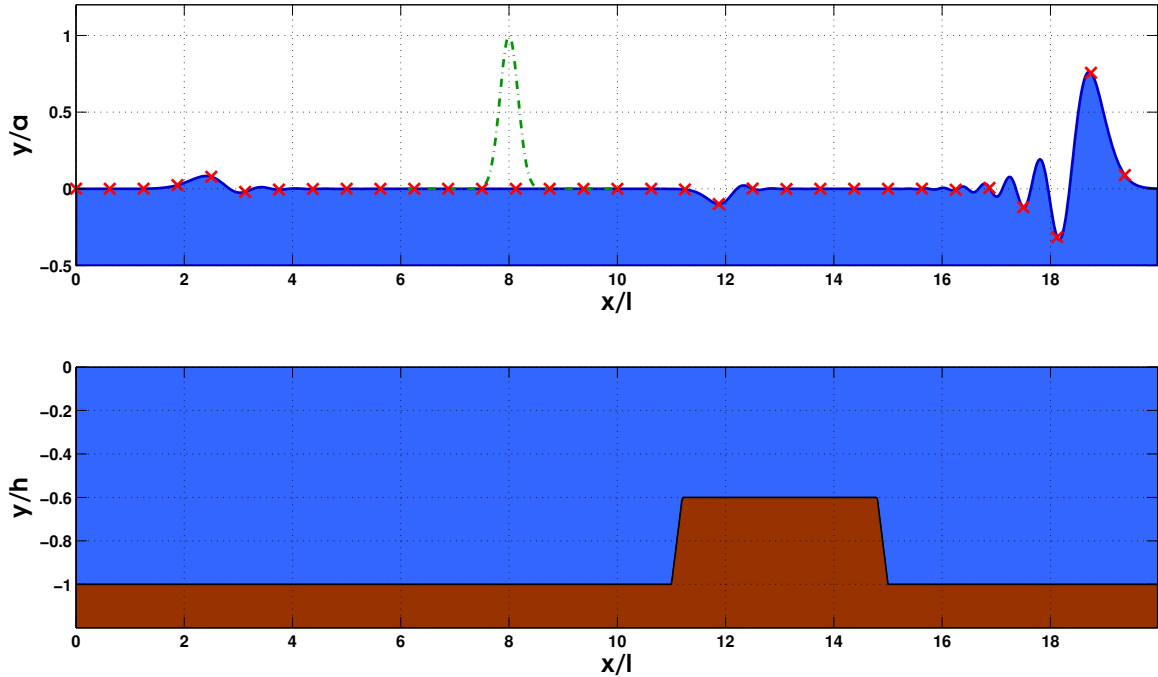


Fig. 2.1 Evolution of the velocity potential after 12 units of time. The solid line is the solution computed with the Non-Local Method and the crosses were computed with the Conformal Method.

Figure (2.1) displays a great deal of qualitative properties of wave propagation worth mentioning. First look at the head of the wave train. Where there was a pulse, now we have a

train of smaller waves. This is the effect of dispersion. Notice that the smaller waves appear behind the wave front, because shorter waves have a smaller propagation speed and also have a smaller amplitude in this case.

The head of the train has stopped, in our reference frame, between 18 and 19. However, over a flat horizontal bottom, the speed of the head of the train was nearly 1 and it moved for 12 unit of time thus having enough time to reach the right end of the domain, so it is clear that the obstacle has slowed down the wave.

Notice the two smaller bumps, one positive and one negative. The positive one is near the left end of the domain and the negative one is over the obstacle. These bumps are reflected waves that appear when the wave passes over the left and right edges of the obstacle, respectively.

In Figure (2.1) the blue line corresponds to the simulation performed with our algorithm whereas the red crosses correspond to the simulation carried out with equations 2.13. All the qualitative features already mentioned plus the fact that the global relative error, of  $6.275 \times 10^{-4}$  less than 0.06%, successfully benchmarks our numerical routine.

## 2.3 Bragg Resonance

This section is devoted to the simulation of Bragg Resonance which studies the interaction between a wave and a periodic underwater topography that varies within a length scale comparable to the wavelength.

When variations on the underwater topography are comparable with the wavelength an obstacle transmits and reflects part of the wave. As every one of the newly created transmitted and reflected waves encounters a new obstacle it undergoes this splitting process again.

In terms of the Fourier modes that build up the wave, we may think that one of the effects of the interaction with the topography is the change of direction of propagation of some Fourier modes. Those Fourier modes that underwent a change in its direction of propagation comprise what is called a reflected wave. All the other Fourier modes compose the transmitted wave.

As each obstacle carries out this transmission-reflection process the overall scattering mechanism seems to lead to a complicated wave field at a first glance. However instead of an unorganized pattern a general macro structure arises on the reflected wave. This macro structure is characterized by having a wavelength twice as large as the wavelength of the underwater sequence of obstacles.

This is where the word resonance comes in, the periodic sequence of obstacles sustains this organized coherent macro structure on the reflected wave.

This resonance interaction has been studied in the linear setting by [17] and references therein. Then it was extended to the non linear case by [5]. Both references show that when the conditions for resonance are met the description of the transmitted and reflected wave can be given as a linear Klein Gordon equation in the linear case, and as a system of coupled KdV equations in the weakly non-linear case.

In order to investigate this resonance process numerically we set up the following simulation, we are going to investigate how a gaussian pulse propagates into a region that has an oscillatory underwater topography. Due to the highly variable nature of the problem we need to use a low pass filter as it will be further discuss in the next section.

### 2.3.1 Simulation Set Up

The parameter used in this simulation were the following

- The length of the channel  $L_x = 10$ .
- The number of equally spaced points is  $N_x = 2^{10}$ .
- The value of the parameter  $\mu = 0.1$ .
- The final time is  $T_f = 4.5$ .
- The initial velocity potential is given by the equation

$$\varphi_0(x) = e^{-\frac{1}{2}\left(\frac{x-c}{\sigma}\right)^2}. \quad (2.16)$$

This Gaussian is centered at  $c = 4$  and has a standard deviation of  $\sigma = 1/6$ .

- The initial wave profile is given by

$$\hat{\eta}_0(k) = \left( \frac{k \tanh(k\mu)}{\mu} \hat{\varphi}_0(k) \right). \quad (2.17)$$

- The underwater periodic structure is given by

$$H(x) = \begin{cases} -1 - \frac{1}{2} \sin(-6\pi(x-5)), & \text{for } 5 < x < 9.5, \\ 0, & \text{for } x < 5 \text{ or } x > 9.5. \end{cases} \quad (2.18)$$

This sinusoid oscillates three times in a interval of length 1, the pulse length.

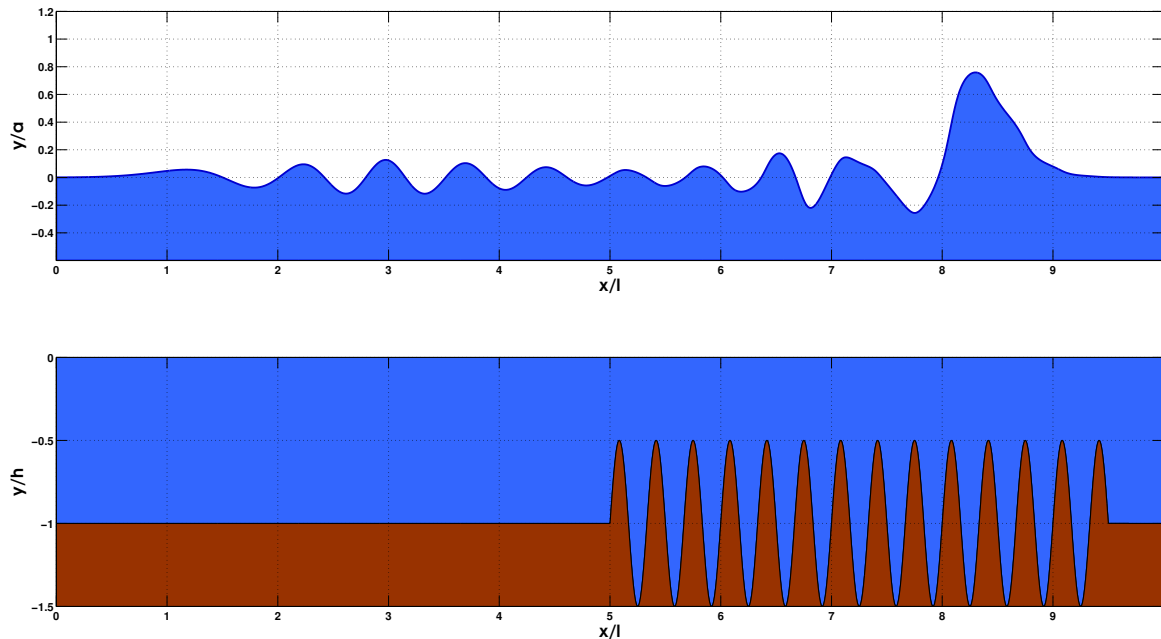


Fig. 2.2 Simulation at  $t = 4.5$ . The underwater sine function oscillates three times per unit distance.

In Figure (2.2) we have the simulation at the final time  $t = 4.5$ . As we can see the train of waves has spread out from the incoming initial pulse. During the simulation the head of the wave moved up and down like a wheel that goes up and down a hilly surface, or as trying to drive in Bogota. A trace of this assertion is still evident at the head of the train, where the wave front is no longer convex.

Behind the wave front we have a tail that somehow resembles a sine function. We must not confuse this tail with the reflected wave.

What the Bragg theory says is that the reflected wave has a wave length about twice as large as the wave length of the bottom. What we are seeing in Figure (2.2) corresponds to the superposition of the transmitted and reflected wave. So in order to show that our method was able to simulate what the theory anticipated we must find out what the reflected wave is. This task was achieved as follows.

In general to each Fourier mode we associate a complex number, the Fourier coefficient, and in general the complex amplitude and the phase are functions of time. As the phase varies with time we may imagine that the Fourier mode is spinning in the complex plane either clockwise or counter clockwise. A clockwise rotation means that the corresponding plane wave is moving forward and a counter clockwise rotation corresponds to the plane wave moving backwards.

So in order to find the reflected wave we must find the direction of the propagation of the Fourier modes at a given instant and then select the reflected, right going, modes. This is exactly what we did in Figure (2.3). Now this is what the theory of Mei in [17] and many others anticipated, the Fourier transform of the reflected wave is tightly localized about the wave number 9.42 which happens to be exactly half of the wave number of the bottom 18.22.

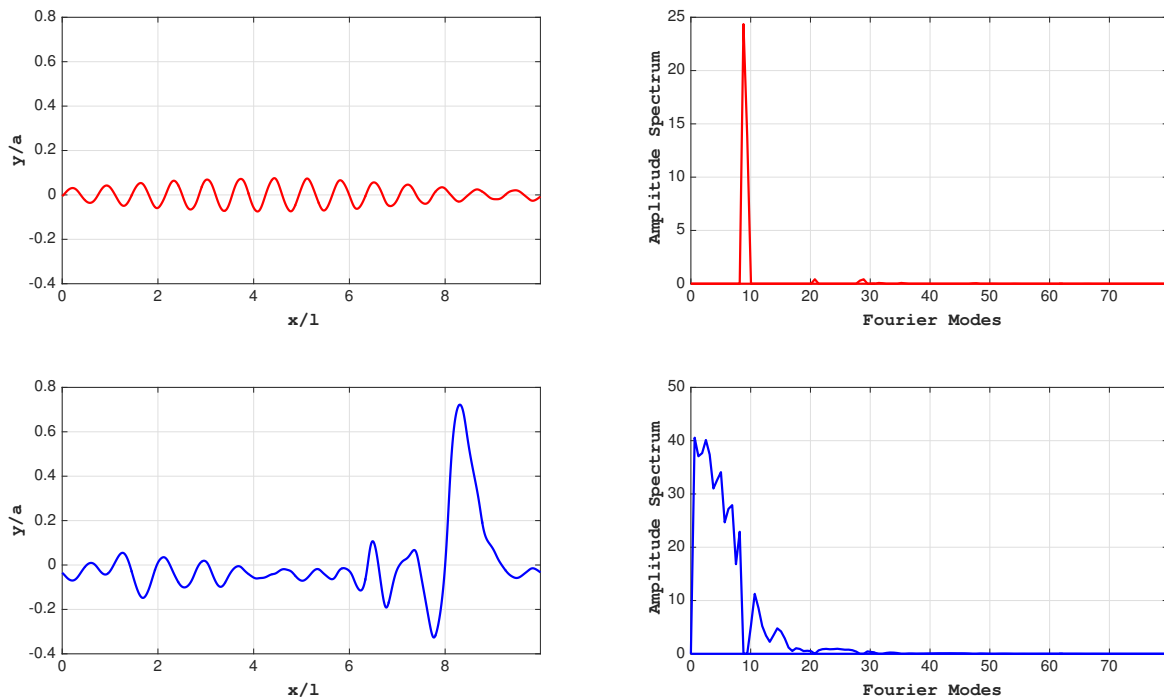


Fig. 2.3 The red curves correspond to the reflected wave and its Fourier transform at  $t = 4.5$ . The Blue lines correspond to the transmitted wave at  $t = 4.5$ .

We performed a second simulation where the only modification was the sine function of the bottom. We increased its frequency from 3 oscillations per unit of distance as in Figure (2.2) to 5 in Figure (2.4).

We have a similar effect as the one already discussed. Look at the head of the wave train in Figure (2.4). It experienced a smaller vertical vibration when compared to the one in Figure (2.2). Again the analogy with the driver comes in handy because this would correspond as driving over an unpaved road where you feel a vibration but you can go through. The tail looks smaller in amplitude in this case and it also resembles that of a sine function.

In Figure (2.5), we can actually see that the amplitude of the reflected wave is smaller than in Figure (2.3). The higher peak in the absolute spectrum of the reflected wave corresponds to the wave number 15.07 whereas the wave number of the underwater sine function corresponds to 30.78. Again our simulation matches with the theory.

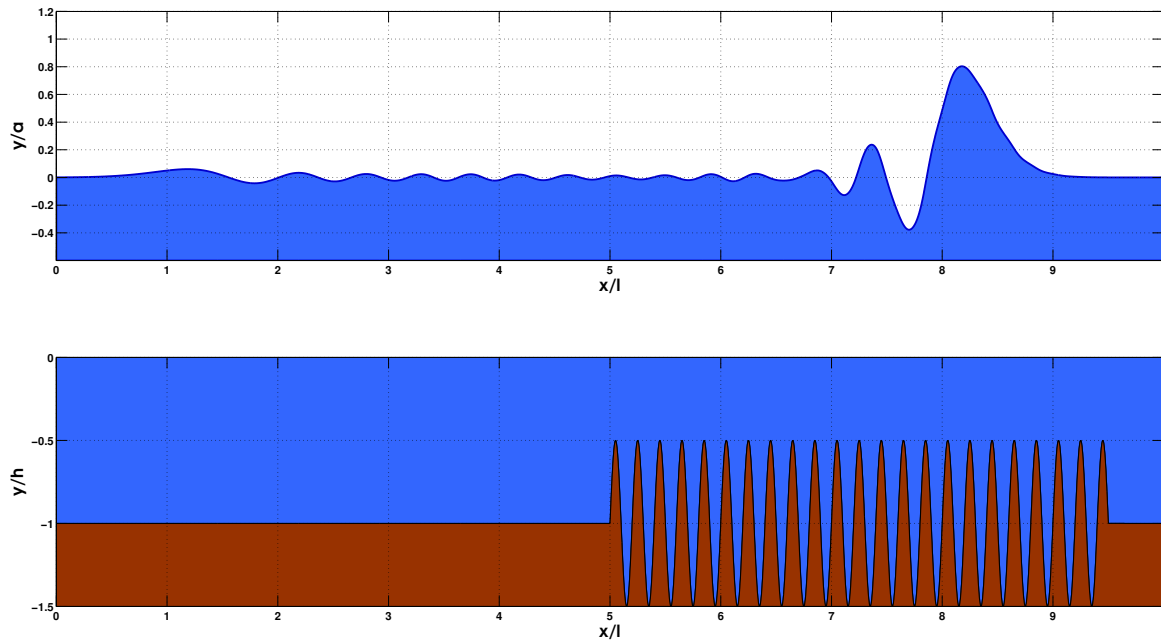


Fig. 2.4 Simulation at  $t = 4.5$ . The underwater sine function oscillates five times per unit distance.

### 2.3.2 Fast Varying Periodic Topographies

We continue this experiment by going one step forward and choosing a sine function that varies even faster with respect to the pulse width. We increased the number of oscillations per unit of distance from 3 and 5 in the previous sections to 12. What we obtained is shown in the following Figure (2.6).

We see that the reflected harmonic wave has faded away. This is known as homogenization, is as if the wave were on a homogeneous flat bottom again. The small reflected wave near the left end of the figure is due to the abrupt change of media and has nothing to do with the phenomena under discussion. Notice that such a tail is present also in (2.2) and (2.4).

When a wave interacts with a highly variable bottom there is an asymptotic theory available first investigated by [23]. There, they used the method of multiple scales expansion to study this homogenization. In order to show what this theory foretells we made the following Figure (2.7).

In the Figure (2.7) we have three different wave profiles. The red one corresponds to the solution without the topography. The blue one correspond to the solution computed with the non-local method and the green one correspond to the solution of a wave that interacts with the envelop of the topography, a rectangle in this case.

In any case we see that no almost harmonic reflected tail is generated (we are ignoring the reflected wave due to the change of media) and the wave spread out into similar wave

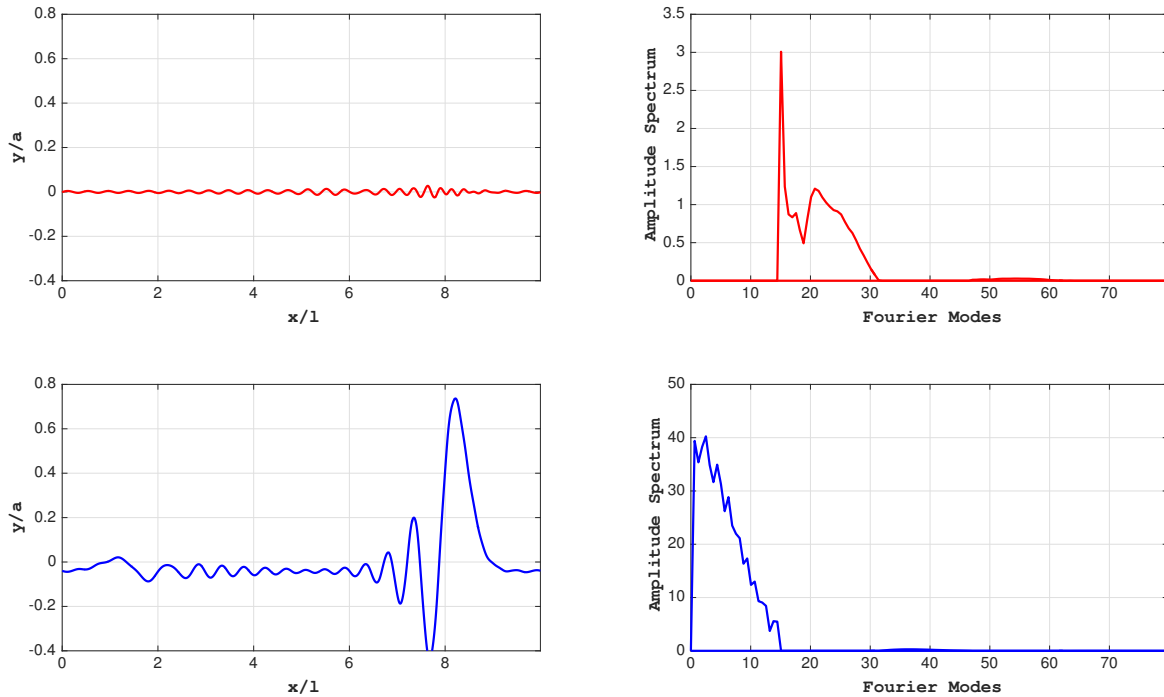


Fig. 2.5 The red curves correspond to the reflected wave and its Fourier transform at  $t = 4.5$ . The Blue lines correspond to the transmitted wave at  $t = 4.5$ .

trains. However, and this is the main thing anticipated by the theory in [23], each wave has a different *speed*, thus the difference in position.

The computed speeds are 0.68 for the green wave, 0.82 for the blue wave and 0.94 for the red wave. Although the blue wave seems to be on a homogeneous media it is neither the flat or the envelop media, it is somewhere in between.

## 2.4 Ill-condition of the Numerical Scheme

In our first simulation the dispersion parameter was set to  $\mu = 0.05$ , physically speaking this represents a pulse that is 20 times larger than the reference depth of the channel, and for the Bragg resonance we set  $\mu = 0.1$ , a wave 10 times larger than the depth, in either case we employed long waves. So what we tried to do next was to study our method with different values of the parameter  $\mu$ .

As we tried higher values of the parameter  $\mu$  we encounter some numerical instabilities with our method. We would like to further discuss what is presented in the work of Deconinck, Vasan, Oliveras and Wilkening in [7, 24, 26] about numerical instabilities regarding non-local numerical routines.

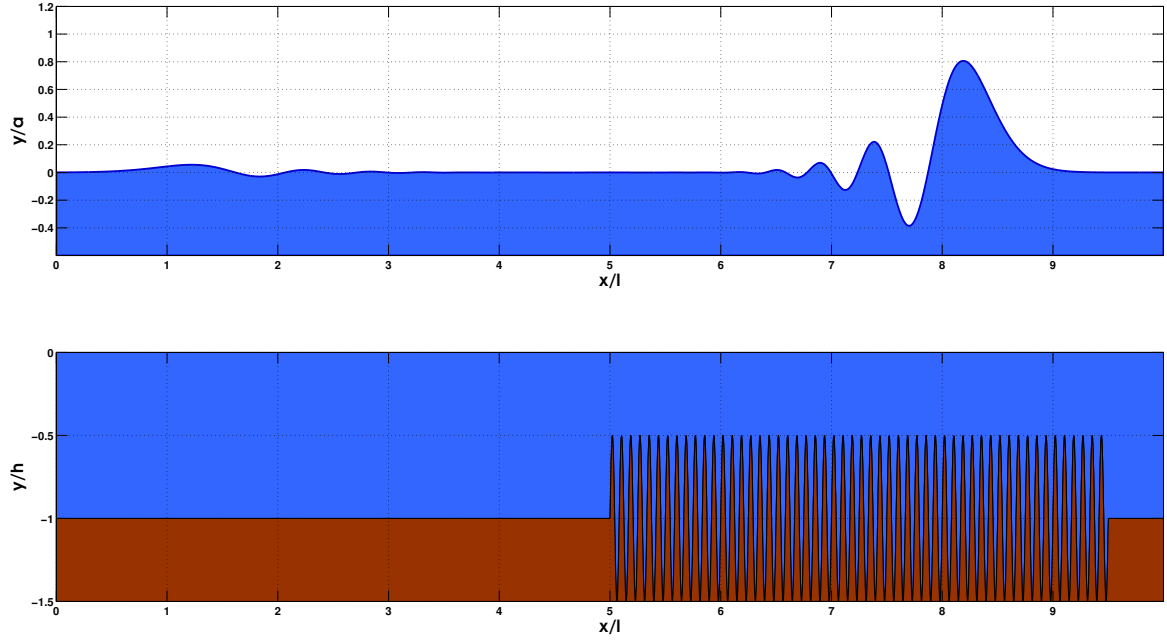


Fig. 2.6 Simulation at  $t = 4.5$ . The underwater sine function oscillates twelve times per unit distance.

Our reason for this conundrum is related with the exponential decay rate of the functions that comprises the matrices that represent the operators  $A$  and  $B$ , the situation is the following:

For each  $x$  and  $\mu$  the decay rate of the functions

$$\begin{aligned} f(k) &= \frac{\sinh(\mu k H(x))}{\cosh(\mu k)}, \\ g(k) &= \frac{\cosh(\mu k (1 + H(x)))}{\cosh^2(\mu k)}, \end{aligned} \quad (2.19)$$

as  $k \rightarrow \infty$ , can be estimated as follows.

First, in order to suppress the dependence on  $x$  the hypothesis on the fluid domain, that variations must be bounded by

$$|H(x)| < c < 1,$$

allows us to bound the function  $f$  and  $g$  uniformly in  $x$  by

$$\begin{aligned} |f(k)| &= \left| \frac{\sinh(\mu k H(x))}{\cosh(\mu k)} \right| < \frac{\cosh(\mu k c)}{\cosh(\mu k)}, \\ |g(k)| &= \left| \frac{\cosh(\mu k (1 + H(x)))}{\cosh^2(\mu k)} \right| < \frac{\cosh(\mu k c)}{\cosh(\mu k)}. \end{aligned} \quad (2.20)$$

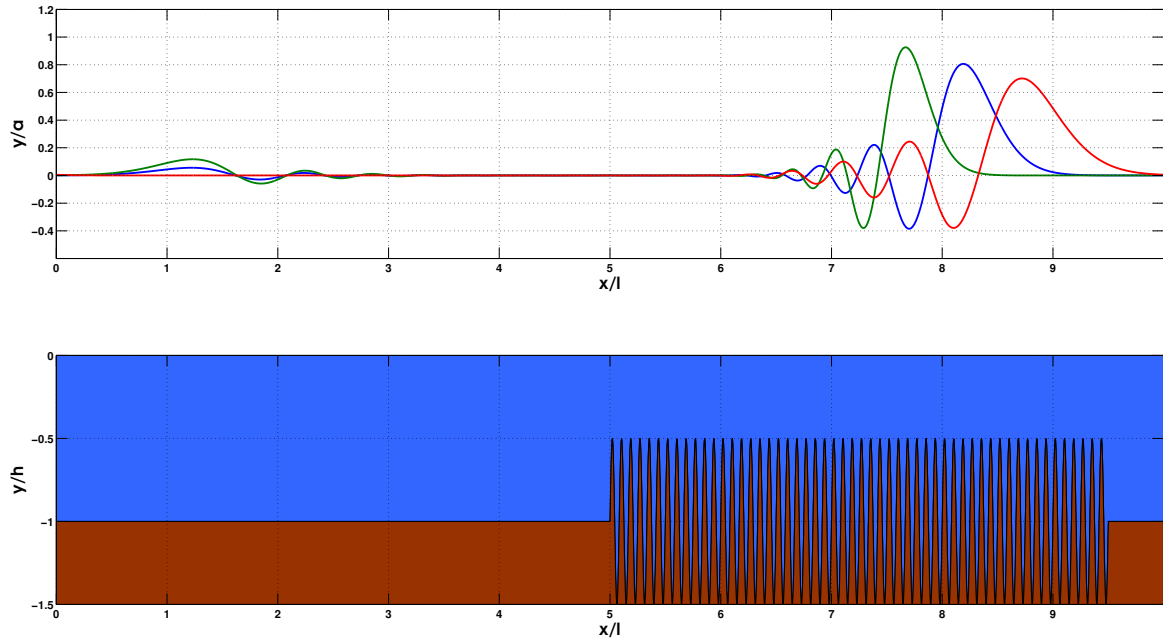


Fig. 2.7 Red curve: Simulation without the topography. Blue curve: Actual simulation. Green curve: Simulation over the envelope of the bottom.

The following inequality completes the estimate

$$\frac{\cosh(\mu kc)}{\cosh(\mu k)} < e^{-\mu k(1-c)}. \quad (2.21)$$

The ill-conditioning of the problem comes from the following reason.

The matrices  $A$  and  $B$  are computed in a column-wise fashion by our algorithm (2.2). When we attempt to compute the columns of the matrix that corresponds to a higher values of  $k$  the effect of the parameter  $\mu$  gets in the way causing the following problems.

For higher values of  $\mu$ , ( $\mu$  close to one for instance) the exponential decay of the quantities involved end up in very small numbers that get stored in the columns of the matrix  $A$  and  $B$ , this is the point of the estimate (2.21) to show that there is an exponential decay in  $k$  that gets stronger when  $\mu$  is larger.

As our algorithm attempts to invert the matrix  $B$ , in order to compute the operator  $G$ , the smaller numbers stored in the columns of the matrix makes the inversion of  $B$  unstable.

We found a way out of this problem and it will be explained the following section. The solution we figure out accomplished two things. The first one is that it avoids the computation of the columns that corresponds to higher values of  $k$ . The second one is that it reduces the size of the matrices involved.

### 2.4.1 Reducing the number of equations

Up to now the Non-Local Method and our numerical scheme has reached out our expectations for small values of  $\mu$ , and have raised a question about the possible ill-conditioning of the method when larger values of  $\mu$  are tried.

We will set aside the instabilities issues of the method for now and we turn into another aspect of the algorithm, the computational cost of the implementation of the algorithm.

In order to get an estimate on the computational cost of our algorithm, the first thing we need to reckon is the number of operations needed in the computation of the matrices  $\hat{A}$  and  $\hat{B}$  that represent the pseudo-differential operators  $A$  and  $B$ . Then we must add the number of operations needed in the inversion of  $\hat{B}$ .

As described in (2.2) the operator  $A$  is computed in essentially four steps.

- Compute a matrix of size  $N \times N$  that contains quantities like  $\sinh(\mu k H(x)) / (k \cosh(\mu k))$ . As the number of points  $x$  is  $N$  and the number of Fourier mode  $k$  is also  $N$ , this whole procedure takes about  $\mathcal{O}(N^2)$  operations.
- Compute the Fourier transform of each column. Each Fourier transform, using the FFT algorithm, needs  $\mathcal{O}(N \log(N))$  operations. Thus this step needs  $\mathcal{O}(N^2 \log(N))$  operations to be completed.
- Reordering the columns of the Matrix computed in the last step. Although this operation does not need arithmetic operations to be performed, it has to be done in each column so it adds  $\mathcal{O}(N)$  operations.
- Multiplication by the matrix of inner products  $kl$  accounts for some more  $\mathcal{O}(N^2)$  operations.

Adding up the number of operations needed to compute the matrix that represents the operators  $A$  and  $B$  requires about  $\mathcal{O}(N^2 \log(N))$  operations. In the simulation above, where  $N = 2^{10}$  was used, the number of operations needed in the computation of the matrices  $\hat{A}$  and  $\hat{B}$  is of order  $\mathcal{O}(2^{22})$ .

The most expensive part of the whole process is the computation of the matrix operation  $B^{-1}A$ . The algorithm used by Matlab to perform this kind of tasks resorts to an  $LU$  factorization with partial pivoting [14] then the  $L$  and  $U$  factors are used to compute  $\hat{B}^{-1}\hat{A}$ .

The cost of the  $LU$  factorization is  $\mathcal{O}(N^3)$ . According to [4] the cost of solving a linear system of the form  $\hat{B}X = Y$  is of order  $\mathcal{O}(2N^2)$  provided that the  $LU$  factors of  $\hat{B}$  are already known. So computing  $\hat{B}^{-1}\hat{A}$  amounts to solving  $N$  linear systems, one for each column of  $\hat{A}$ . Adding up we obtain that, the total number of operations needed to compute  $\hat{B}^{-1}\hat{A}$  is of order  $\mathcal{O}(N^3)$ , about  $\mathcal{O}(2^{30})$  operations!

The key point of this algorithm is the fact that such computation is done once and for all. The matrix  $B^{-1}A$  can be saved and reused in subsequent computations, having said so, every time we need to compute the right hand side of (2.10) in the process of time integration,  $\mathcal{O}(N^2)$  operations are going to be performed at each time step.

As the number of operations involved is high we made an attempt to reduced it as much as possible. The idea behind is motivated by the following physical intuition, shorter waves should not interact with the bottom. This plus the evidence that our method becomes “ill conditioned” when it comes to higher wave numbers, gave us the idea that we might be able to restrict the matrices  $\hat{A}$  and  $\hat{B}$  to the lower frequencies retaining the whole information.

Schematically we have the following situation in formula (2.5)

$$\begin{bmatrix} \dots\dots\dots \\ \dots \hat{G}(k,l) \dots \\ \dots\dots\dots \end{bmatrix} \begin{bmatrix} \dots \\ \hat{q}(k) \\ \dots \end{bmatrix} = \begin{bmatrix} \dots \\ \hat{g}(k) \\ \dots \end{bmatrix}.$$

There is a linear operator  $\hat{G}$  that maps the Fourier transform of the velocity potential  $\hat{g}(k)$  onto a vector  $\hat{q}(k)$  in Fourier space. This vector contains the information from the bottom boundary condition.

The dotted entires for the matrix and the vector in the schematic picture above represent the higher wave numbers. If we are to use the exponential decay of the term  $\text{sech}(\mu k)^2$  in formula (2.10) as an alibi for neglecting the higher wave number components of the vector  $\hat{g}$  and we also neglect the higher frequency components for the input vector  $\hat{q}$  then we can equally neglect the corresponding dotted entries of the matrix  $\hat{G}$ , thus obtaining a smaller block inside the diagonal.

It is important to keep in mind what the problem is. What we are trying to overcome lies not on the size of matrix  $\hat{G}$  itself but on the  $\mathcal{O}(N^3)$  number of intermediate computations that must be performed during the computation of the matrix. So we must take one step back to the matrices  $\hat{A}$  and  $\hat{B}$  and find a way to reduce their size as well. The relation between the  $\hat{A}$  and  $\hat{B}$  can be pictured as follows

$$\begin{bmatrix} \dots \hat{B}(k,l) \dots \\ \dots \hat{B}(k,l) \dots \\ \dots \hat{B}(k,l) \dots \end{bmatrix} \begin{bmatrix} \dots \\ \hat{g}(k) \\ \dots \end{bmatrix} = \begin{bmatrix} \dots \hat{A}(k,l) \dots \\ \dots \hat{A}(k,l) \dots \\ \dots \hat{A}(k,l) \dots \end{bmatrix} \begin{bmatrix} \dots \\ \hat{q}(k) \\ \dots \end{bmatrix}.$$

Again the dotted entries of the vectors represent the higher wave number components that we are neglecting. The dotted entries of the matrices are the entries that interact with the higher frequencies when the multiplication is carried out.

The first idea that came out was to consider an over determined system of equations. This is accomplished by chopping off the dotted entries of the matrices and the vectors involved obtaining in this way a rectangular system of equations. Then the idea was to find a minimum square solution to the problem.

This idea was explored by Wilkening and Vasan, in [26], in the context of nonlinear two dimensional waves. The idea worked out in their setting, but we refrained of doing so because in the three dimensional setting, our main objective, the size of the matrices involved is  $N^2$  where  $N = N_x N_y$  so, assuming  $N_x = N_y$  the size of the matrices is actually way larger,  $Nx^4$ , and this is still too much for the minimum squares algorithm.

In view of this panorama we employed the following trick, not only there are some columns of the matrix going to be deleted but we also are going to suppress the corresponding rows. Schematically we delete the dotted entries of the matrices and the vectors

$$\begin{bmatrix} \dots & \dots & \dots \\ \dots & \hat{B}(k, l) & \dots \\ \dots & \dots & \dots \end{bmatrix} \begin{bmatrix} \dots \\ \hat{g}(k) \\ \dots \end{bmatrix} = \begin{bmatrix} \dots & \dots & \dots \\ \dots & \hat{A}(k, l) & \dots \\ \dots & \dots & \dots \end{bmatrix} \begin{bmatrix} \dots \\ \hat{q}(k) \\ \dots \end{bmatrix}.$$

This gives us three things. The first one is a couple of smaller rectangular matrices. The second one is a lot of uncertainty because we have no clue about where to cut the matrices and what possible error this might introduce. The third one is a free parameter  $N$ , the size of the smaller block matrix, that we can choose such as to keep errors under control.

### 2.4.2 Algorithm two

This algorithm is a modification of the former (2.2), it includes the truncation of the matrices  $\hat{A}$  and  $\hat{B}$ , and thus it is more efficient.

1. Choose a positive integer  $N$ . This  $N$  will be the cut off parameter.
2. Preallocate a matrix  $M$  of size  $N_x \times (2N + 1)$ . Where  $N_x$  is the number of points in physical space.
3. We select the following Fourier modes in the following order:

$$\frac{2\pi}{L_x} [0, 1, 2, \dots, N, -N, \dots, -2, -1, ]$$

4. Choose a column of the matrix  $M$  and let  $k$  denote the corresponding wave number associated with that column. Fill the selected column with the numbers,

$$\frac{\sinh(\mu k H(x_m))}{k \cosh(\mu k)},$$

where  $x_m$  is the  $m$ -th physical point. The order of the elements of the column must follow the usual ordering of the point  $x_m$ .

5. Compute, using the *fft* command, the Fourier coefficients of the periodic function that is temporarily stored in the column of the matrix  $M$ . Store this column vector back in the corresponding column of the matrix  $M$ .
6. As explained in Algorithm (2.2) permute the elements of the column until the following relation holds

$$M(m, j) = N_x \int_0^{L_x} e^{-i(m-k)x} \frac{\sinh(\mu k H(x))}{k \cosh(\mu k)} dx.$$

7. Delete the entries of the column that correspond to wave numbers higher than  $2\pi N/L_x$  and wave numbers lower than  $-2\pi N/L_x$ .
8. Repeat steps 3 to 5 in every column.
9. Finally we compute a matrix with all the possible inner products of wave number and perform an entry wise multiplication. This final matrix will represent the truncated operator  $\hat{A}_N$ .
10. We repeat the same steps for the truncated operator  $\hat{B}_N$ . Notice that the only difference occurs at step 3 where we must compute the following expression

$$\frac{\cosh(\mu k(1 + H(x_m)))}{k \cosh^2(\mu k)}.$$

11. Compute the matrix inversion and multiplication

$$M_1 = \hat{B}^{-1} \hat{A}.$$

Notice that we reduce the size of the matrix to be inverted from  $N_x \times N_x$  to  $(2N + 1) \times (2N + 1)$ .

12. In a new zero matrix of size  $N_x \times N_x$  we encrust the matrix  $M_1$  as a diagonal block in the center of the matrix.
13. Finally, compute two diagonal matrices  $D_1 = \text{diag}(k \tanh(\mu k))$  and  $D_2 = \text{diag}(\text{sech}^2(\mu k))$ . The matrix representation of the truncated Dirichlet-to-Neumann operator given by

$$\hat{G}_N = D_1 + D_2(\hat{B}_N^{-1} \hat{A}_N).$$

This algorithm does not include the time step integration of the evolution equations. So we supplemented it with Matlab's ode113 numerical routine for the full simulation of equations (2.11).

The number of operations has been reduced from  $\mathcal{O}(N_x^3)$  needed in our first algorithm to  $\mathcal{O}((2N+1)^3)$ .

Before we use Matlab's ode113 numerical scheme to integrate the equations in time, there is a question that needs to be studied right away. Where should the matrix and the vectors be cut off in a way that information is preserved? There is already a candidate at hand, owing to the exponential decay of  $\text{sech}(\mu k)^2$  we just need to pick up wave numbers such that  $\mu k$  lies below a certain tolerance. We investigate this in the next simulation.

### 2.4.3 Simulation set up

In order to show that the filter proposed is a workaround the ill-conditioning problem, we repeated the simulation of (2.2.2), but with the matrix  $\hat{G}$  replaced by its truncated version  $\hat{G}_N$ . Because we want to know what are the possible outcomes that different cut-off parameters  $N$  might produce our simulation was repeated with 127 different values of the parameter  $N$ .

The results of our simulation are in Figure (2.8), where we measured the maximum, over all the collocation points, of the relative error of the solution computed with our method and the solution computed with the conformal mapping technique as function of the cut-off parameter  $N$ . What we want to show is how we can capture the solution of the problem by using an appropriate ideal filter.

In Figure (2.8), the blue line shows the relative error of the solution of the non-local method, as compared to the conformal-method, for different values of the cut-off parameter  $N$  and each panel displays the result for different values of  $\mu$ . The result is plotted on a logarithmic scale, and below the horizontal line we have relative errors below 1%. The red point represents a particular value of the cut-off parameter  $N$  chosen to satisfy the following prescription:  $\text{sech}(k\mu)^2 = 10^{-10}$ .

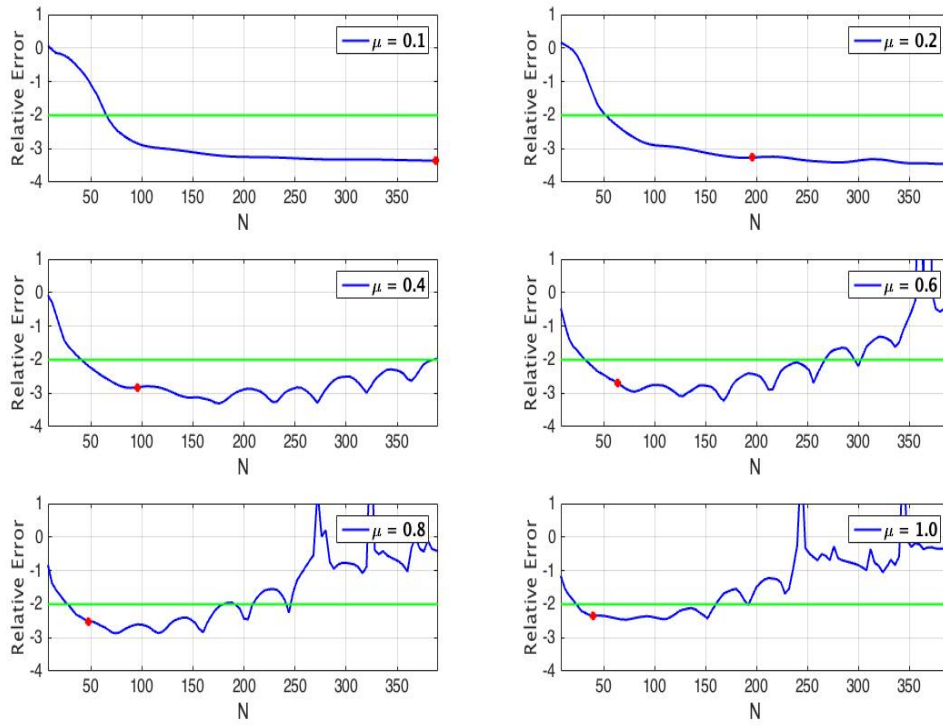


Fig. 2.8 Relative errors between the Non-Local method and the Conformal method. The horizontal line represents error threshold 1%. The red point corresponds to the simulation with the smallest  $N$  that satisfies  $\text{sech}(2\pi N\mu/L_x)^2 < 10^{-10}$ . The vertical axis is on a logarithmic scale.

There are several interesting conclusions regarding the ill-conditioning of the Non-Local Method that we can draw from Figure (2.8).

All the relative error curves begin with a fast decay followed by different behaviors. This initial decay can be explained as follows, when  $N = 0$ , no wave number was picked up by the algorithm so the matrix representation of the operator  $G$  has no information of the topography and so it merely solves the problem as in the flat bottom scenario. As the value of  $N$  increases progressively, more and more wave numbers are taking into account by the operator and so the relative error curve goes down.

Right after the relative error curve has reached the desired tolerance of 1%, there is always an interval of values for the parameter  $N$ , where it remains below the green line, although this interval of values depends on the parameter  $\mu$ , it is a positive point regarding the overall performance of the non-local method.

This interval shows two important things. The first one is that the interval begins at a certain number  $N$ , which is not so large, meaning that only those first  $N$  frequencies have

sufficient information to model the wave topography interaction accurately. The second important property about the interval is that as long as we choose a cut-off parameter  $N$  inside the interval, the simulation will remain accurate.

In the overall performance of the non-local method this interval reflects the stability properties of the algorithm, we can find an appropriate parameter cut-off parameter  $N$  and moreover such parameter can be modified without interfering with the output.

In the first two panels we see that after an initial transient the relative error curve saturates below the tolerance regime of 1%. This suggests that the exponential decay discussed in (2.2.2) did not take place, yet it seems to be no gain in considering a very large or the full system. This is coherent with our previous simulation where  $\mu = 0.05$  where we were able to handle the whole system with no difficulty.

In the last four panels the blue line behaves abnormally, jumping up and down until it finally escapes the green line and forms some abnormal peaks in the higher wave number region.

We have no clue about what is triggering this abnormal behavior yet the overall tendency to escape the green line we think is a consequence of the inversion of the ill conditioned matrix  $B$ . The fact that this erratic tendency becomes more evident where the value  $\mu$  gets closer to one reinforces our explanation of the exponential decay.

In the work of Vasan, Deconinck, see [24], and Oliveras, Deconinck, see [7], it is reported that some kind of numerical instability was also observed during their simulations. They also blame the exponential growth of the hyperbolic functions as triggering the instabilities, and in order to overcome such problem they propose that an arbitrary precision machine should be used in all the intermediate computations.

Those ideas were developed further in [26] where they study the numerical convergence, stability and instabilities of this type of Non-Local methods and compare them with other techniques. In [26] they propose a similar method of truncation of the operator to overcome such a difficulty however they always used an arbitrary precision machine during the computations.

## Summary

In this section we ended up with an efficient algorithm that is capable of simulating the motion of waves over topography in the two dimensional case. We benchmark our method with the conformal mapping technique, we always obtained relative errors below 1%.

We used our numerical routine to investigate the Bragg resonance and the homogenization effects, that arises with the interaction with periodic topographies.

Finally we implemented a low pass filter that allowed us to capture different wave regimes.

In the next section we take our non-local formulation and non-local numerical scheme one step forward by studying the three dimensional case.

# Chapter 3

## Three Dimensional Simulations

Most of what is known nowadays in the numerical modeling of wave-topography interaction on a three dimensional fluid domain is based on approximate equations of potential theory. Most of such approximate models are able to describe the wave-topography interaction when variations of the bottom topography are small. However there is almost nothing in the literature when it comes to the full simulation of potential theory equations, even in the linear case.

According to our bibliographical revision of the topic the only known reference where direct numerical simulation of a three dimensional wave-topography interaction, based on potential theory, is the work of Belibassakis and Athanassoulis [3]. In their work they study the wave pattern generated by a monochromatic point source that propagates over a topography that has level lines parallel to the  $y$  axis. Their work is based on the construction of a Green's function for the water wave problem. However their method does not generalize to the case of an arbitrary topography.

The reason why we began our research on Non-Local representations of the Dirichlet-to-Neumann operator was the possibility of simulating the wave-topography interaction on a three dimensional fluid domain, directly from the linearized potential theory equations.

In the literature, particularly in the work of [18], [6] and [1] it is shown how it would be possible to derive a non local representation for the Dirichlet-to-Neumann operator that includes the effects of the topography. However, so far, no one has ever actually done it.

### 3.1 Construction of the operator

We adapt the formulation explained in the first chapter for the case of doubly periodic functions. The main difference is that we use Fourier series instead of Fourier integrals and

the procedure is entirely analogous to the two dimensional case. In order to provide a brief and complete description we include some details.

We represent the velocity potential  $\varphi$  as:

$$\varphi(\mathbf{x}, z, t) = \sum_{\mathbf{k} \in \Lambda} e^{i\mathbf{k} \cdot \mathbf{x}} \left[ \hat{f}(\mathbf{k}, t) \frac{\cosh(\mu k(z+1))}{\cosh(\mu k)} + \hat{g}(\mathbf{k}, t) \frac{\sinh(\mu k(z+1))}{k \cosh(\mu k)} \right]. \quad (3.1)$$

This representation is similar to (1.11), however the lateral boundary conditions allows us to change the integral by a series, in which the Fourier spectrum  $\Lambda = (2\pi\mathbb{Z}/L_x) \times (2\pi\mathbb{Z}/L_y)$ . The parameters  $L_x$  and  $L_y$  are the corresponding lengths in the horizontal and vertical directions. This representation immediately implies that

$$\hat{q}(\mathbf{k}, t) = \hat{\varphi}(\mathbf{k}, 0, t) = \hat{f}(\mathbf{k}, t) + \hat{g}(\mathbf{k}, t) \frac{\tanh(\mu k)}{k}, \quad \mathbf{k} \in \Lambda. \quad (3.2)$$

Whenever the value of  $q(\mathbf{x}, t)$  is known equation, (3.2) provides a linear relation for the two unknown coefficients  $\hat{f}$  and  $\hat{g}$ . The idea is to use the impermeability boundary condition to close the system for  $\hat{f}$  and  $\hat{g}$ . We drop the  $t$  dependence on the coefficients for simplicity in the equations.

The impermeability boundary condition is

$$\frac{\partial \varphi}{\partial \vec{n}} = 0 \quad \text{on } z = -1 - H(x, y). \quad (3.3)$$

Computing all the derivatives involved in this formula gives rise to the following equation

$$0 = \sum_{\mathbf{k} \in \Lambda} \hat{f}(\mathbf{k}) \nabla \cdot \left[ e^{i\mathbf{k} \cdot \mathbf{x}} \frac{\sinh(\mu k H(\mathbf{x}))}{\cosh(\mu k)} \frac{\mathbf{k}}{k} \right] - \hat{g}(\mathbf{k}) \nabla \cdot \left[ e^{i\mathbf{k} \cdot \mathbf{x}} \frac{\cosh(\mu k H(\mathbf{x}))}{\cosh(\mu k)} \frac{\mathbf{k}}{k^2} \right]. \quad (3.4)$$

Substitution of (3.2) into this equation (3.4) yields

$$\begin{aligned} \sum_{\mathbf{k} \in \Lambda} \hat{q}(\mathbf{k}) \nabla \cdot \left[ e^{i\mathbf{k} \cdot \mathbf{x}} \frac{\sinh(\mu k H(\mathbf{x}))}{\cosh(\mu k)} \frac{\mathbf{k}}{k} \right] &= \\ &= \sum_{\mathbf{k} \in \Lambda} \hat{g}(\mathbf{k}) \nabla \cdot \left[ e^{i\mathbf{k} \cdot \mathbf{x}} \frac{\tanh(\mu k) \sinh(\mu k H(\mathbf{x}))}{\cosh(\mu k)} \frac{\mathbf{k}}{k^2} \right] \\ &+ \sum_{\mathbf{k} \in \Lambda} \hat{g}(\mathbf{k}) \nabla \cdot \left[ e^{i\mathbf{k} \cdot \mathbf{x}} \frac{\cosh(\mu k H(\mathbf{x}))}{\cosh(\mu k)} \frac{\mathbf{k}}{k^2} \right] \\ &= \sum_{\mathbf{k} \in \Lambda} \hat{g}(\mathbf{k}) \nabla \cdot \left[ e^{i\mathbf{k} \cdot \mathbf{x}} \frac{\cosh(\mu k (1 + H(\mathbf{x})))}{\cosh^2(\mu k)} \frac{\mathbf{k}}{k^2} \right]. \end{aligned} \quad (3.5)$$

This are the corresponding doubly periodic counterparts of the operator  $A$  and  $B$ , explained in chapter one, that account for the topographic effects and provides the following linear relation between  $\hat{q}$  and  $\hat{g}$ .

$$A\hat{q} = B\hat{g} \iff \hat{g} = B^{-1}A\hat{q}. \quad (3.6)$$

In Fourier space the expression that represents the operators are

$$\widehat{A}\hat{q}(\mathbf{l}) = \int_{T^2} e^{-i\mathbf{l}\cdot\mathbf{x}} \sum_{\mathbf{k}\in\Lambda} \hat{q}(\mathbf{k}) \nabla \cdot \left[ e^{i\mathbf{k}\cdot\mathbf{x}} \frac{\sinh(\mu k H(\mathbf{x}))}{\cosh(\mu k)} \frac{\mathbf{k}}{k} \right] d\mathbf{x}, \text{ for } \mathbf{l} \in \Lambda$$

And the Fourier transform of the left hand side of (3.5) is

$$\widehat{B}\hat{q}(\mathbf{l}) = \int_{T^2} e^{-i\mathbf{l}\cdot\mathbf{x}} \sum_{\mathbf{k}\in\Lambda} \hat{g}(\mathbf{k}) \nabla \cdot \left[ e^{i\mathbf{k}\cdot\mathbf{x}} \frac{\cosh(\mu k (1 + H(\mathbf{x})))}{\cosh^2(\mu k)} \frac{\mathbf{k}}{k^2} \right] d\mathbf{x}, \text{ for } \mathbf{l} \in \Lambda.$$

The expressions for the operators  $\widehat{A}\hat{g}$  and  $\widehat{B}\hat{q}$  can be simplified further by using integration by parts. The simplified formulas are

$$\begin{aligned} \widehat{A}\hat{q}(\mathbf{l}) &= \sum_{\mathbf{k}\in\Lambda} i(\mathbf{l}\cdot\mathbf{k}) \hat{q}(\mathbf{k}) \int_{T^2} e^{-i(\mathbf{l}-\mathbf{k})\cdot\mathbf{x}} \left[ \frac{\sinh(\mu k H(\mathbf{x}))}{k \cosh(\mu k)} d\mathbf{x} \right], \\ \widehat{B}\hat{g}(\mathbf{l}) &= \sum_{\mathbf{k}\in\Lambda} i(\mathbf{l}\cdot\mathbf{k}) \hat{g}(\mathbf{k}) \int_{T^2} e^{-i(\mathbf{l}-\mathbf{k})\cdot\mathbf{x}} \left[ \frac{\cosh(\mu k (1 + H(\mathbf{x})))}{k^2 \cosh^2(\mu k)} d\mathbf{x} \right]. \end{aligned} \quad (3.7)$$

These formulas form an “infinite system” of equations that determine the coefficients  $\hat{g}(\mathbf{k})$  in terms of the known coefficients  $\hat{q}(\mathbf{k})$ .

Once the set of coefficients  $\hat{g}(\mathbf{k})$  are determined, the trace of the vertical velocity at  $z = 0$ , in Fourier space, is given by

$$\hat{\phi}_z(\mathbf{k}, 0) = \mu \hat{q}(\mathbf{k}) k \tanh(\mu k) + \mu \hat{g}(\mathbf{k}) \operatorname{sech}^2(\mu k). \quad (3.8)$$

### 3.1.1 Spectral O.D.E's

In Fourier space the system (1.19) becomes,

$$\begin{aligned} \hat{\eta}_t &= \frac{1}{\mu^2} \widehat{G}\hat{q}, \\ \hat{q}_t &= -\hat{\eta}. \end{aligned} \quad (3.9)$$

We use formula (3.8) to obtain

$$\begin{aligned}\hat{\eta}_t(\mathbf{k}) &= (\hat{q}(\mathbf{k})k \tanh(\mu k) + \hat{g}(\mathbf{k}) \operatorname{sech}^2(\mu k))/\mu, \\ \hat{q}_t(\mathbf{k}) &= -\hat{\eta}(\mathbf{k}).\end{aligned}\tag{3.10}$$

Using the linear relation between  $\hat{q}$  and  $\hat{g}$  given in (3.6) we can close the system of equations (3.10) in terms of  $\hat{q}$  and  $\hat{\eta}$  only:

$$\begin{aligned}\hat{\eta}_t(\mathbf{k}) &= (\hat{q}(\mathbf{k})k \tanh(\mu k) + (\hat{B}^{-1}\hat{A}\vec{q})(\mathbf{k}) \operatorname{sech}^2(\mu k))/\mu, \\ \hat{q}_t(\mathbf{k}) &= -\hat{\eta}(\mathbf{k}).\end{aligned}\tag{3.11}$$

This is what we were aiming at, to formulate a system of ordinary differential equations in Fourier space, that are coupled by the action of the linear operators  $A$  and  $B$ , dependent only on the value of the quantities  $q$  and  $\eta$ .

### Special case $H = 0$

We consider now the easiest case where the bottom topography is flat,  $H = 0$ . In this case equation (3.5) reads as

$$0 = \sum_{\mathbf{k} \in \Lambda} \hat{g}(\mathbf{k}) \nabla \cdot \left[ e^{i\mathbf{k} \cdot \mathbf{x}} \frac{1}{\cosh(\mu k)} \frac{\mathbf{k}}{k^2} \right] = i \sum_{\mathbf{k} \in \Lambda} e^{i\mathbf{k} \cdot \mathbf{x}} \hat{g}(\mathbf{k}) \frac{1}{\cosh(\mu k)},$$

and this can happen only if  $\hat{g}(\mathbf{k}) = 0$  for every  $\mathbf{k}$ . So the system (3.11) decouples and simplifies to

$$\begin{aligned}\hat{\eta}_t(\mathbf{k}) &= (\hat{q}(\mathbf{k})k \tanh(\mu k))/\mu, \\ \hat{q}_t(\mathbf{k}) &= -\hat{\eta}(\mathbf{k}).\end{aligned}\tag{3.12}$$

This is the classical system in Fourier space for the water wave problem in three dimensions. See [25].

## 3.2 Algorithm three

Based on the three dimensional non local formulas for the water wave problem that we are currently investigating, and also based on our experience in the two dimensional case, we then take our algorithm to a further stage of development. This algorithm incorporates the truncation property that proved valuable in the two dimensional case allowing the modeling of different wave regimes efficiently.

The algorithm is:

1. Choose two positive integers  $M_x$  and  $M_y$ . These  $M_x$  and  $M_y$  will be the cut off parameters. We need two cut off parameters because we need to truncate in both the  $x$  wave numbers and the  $y$  wave numbers. The number of selected wave numbers is  $M = (2M_x + 1)(2M_y + 1)$ .
2. Allocate a matrix  $M_1$  of size  $N \times M$ . Where  $N$  is the total number of points in physical space.  $N = N_x N_y$  where  $N_x$  and  $N_y$  is the number of points in each direction respectively.
3. The Fourier modes in this case are given by 2–vectors of wave numbers  $\mathbf{k} = (k_1, k_2)$ . We choose them from the set

$$\left\{ \frac{2\pi}{L_x} [0, 1, 2, \dots, M_x, -M_x, \dots, -2, -1, ] \right\} \times \left\{ \frac{2\pi}{L_y} [0, 1, 2, \dots, M_y, -M_y, \dots, -2, -1, ] \right\},$$

and we use the lexicographic order to identify each Fourier mode with each column of the matrix  $M_1$ .

4. Choose a column of the matrix  $M_1$ ,  $\mathbf{k}$  denote its corresponding wave number. Using the *fft2* algorithm compute the two dimensional discrete Fourier transform of the function

$$\frac{\sinh(\mu k H(x_{m_1 m_2}))}{k \cosh(\mu k)}.$$

5. The output of step 4 is a  $N_y \times N_x$ ,  $M_2$  matrix. Use the usual lexicographic order to assign to each entry of the selected column of  $M_1$  its corresponding entry of  $M_2$ .
6. Permute the elements of the column until the following relation holds

$$M(m, j) = N \int_0^{L_y} \int_0^{L_x} e^{-i(\mathbf{m}-\mathbf{k}) \cdot \mathbf{x}} \frac{\sinh(\mu k H(\mathbf{x}))}{k \cosh(\mu k)} d\mathbf{x}.$$

where  $m$  is the corresponding index of the Fourier mode  $\mathbf{m}$ .

7. Delete the entries of the column that correspond to wave numbers outside the spectral limits given in step 2.
8. Repeat steps 3 to 5 in every column.
9. Finally we compute a matrix with all the possible inner products of wave number and perform an entrywise multiplication. This final matrix will represent the truncated operator  $\hat{A}_N$ .

10. We repeat the same steps for the truncated operator  $\hat{B}_N$ . Notice that the only difference occurs at step 3 where we must compute the following expression

$$\frac{\cosh(\mu k(1 + H(x_{m_1 m_2})))}{k^2 \cosh^2(\mu k)}.$$

11. Compute the matrix inversion and multiplication

$$M_3 = \hat{B}_N^{-1} \hat{A}_N.$$

12. In a new zero matrix of size  $N_x \times N_x$  we embed the matrix  $M_1$  as a diagonal block in the center of the matrix.

13. Finally, compute two diagonal matrices  $D_1 = \text{diag}(k \tanh(\mu k))$  and  $D_2 = \text{diag}(\text{sech}^2(\mu k))$ . The matrix representation of the truncated Dirichlet-to-Neumann operator given by

$$\hat{G}_N = D_1 + D_2(\hat{B}_N^{-1} \hat{A}_N).$$

### First simulation

The first simulation that we did represents a consistency test between the three dimensional algorithm (3.2) with the two dimensional one (2.4.2). We simulate a plane wave that passes over a submerged trapezoidal ridge in exactly the same configuration as in Figure (2.1). The trapezoidal ridge has level lines perpendicular to the direction of propagation, as well as the wave, so no transversal dynamics are involved. This simulation set up, although it is the easiest possible, is important because it is the only situation where we can compare our simulation with some other solution.

The parameters used in the simulation were the following:

- The dimensions of the domain are  $L_x = 20$  and  $L_y = 20$ .
- The number of points in each direction is  $N_x = N_y = 2^{10}$ .
- The value of the dispersion parameter is  $\mu = 0.05$ .
- The final time is  $T_f = 12$ .
- The initial velocity potential is given by the equation

$$\varphi_0(x, y) = e^{-\frac{1}{2} \left( \frac{x-c}{\sigma} \right)^2}. \quad (3.13)$$

This Gaussian is centered at  $c = 8$  and has a standard deviation of  $\sigma = 1/6$ .

- The initial wave profile is given by

$$\hat{\eta}_0(\mathbf{k}) = \left( \frac{k \tanh(k\mu)}{\mu} \hat{\phi}_0(\mathbf{k}) \right). \quad (3.14)$$

- The underwater trapezoid has height 0.4, length of the base 4 and length of top phase 3.6.
- The cut off parameters were set to  $M_x = 110$  and  $M_y = 10$ . The number of frequencies allowed in the  $x$  direction is the same as the one used in algorithm 2.4.2, however for the  $y$  axis we let a smaller number of wave numbers because no change in the  $y$  direction is expected.
- We used the classical Runge-Kutta of fourth order for the time integration with time step  $dt = 1/30$ .

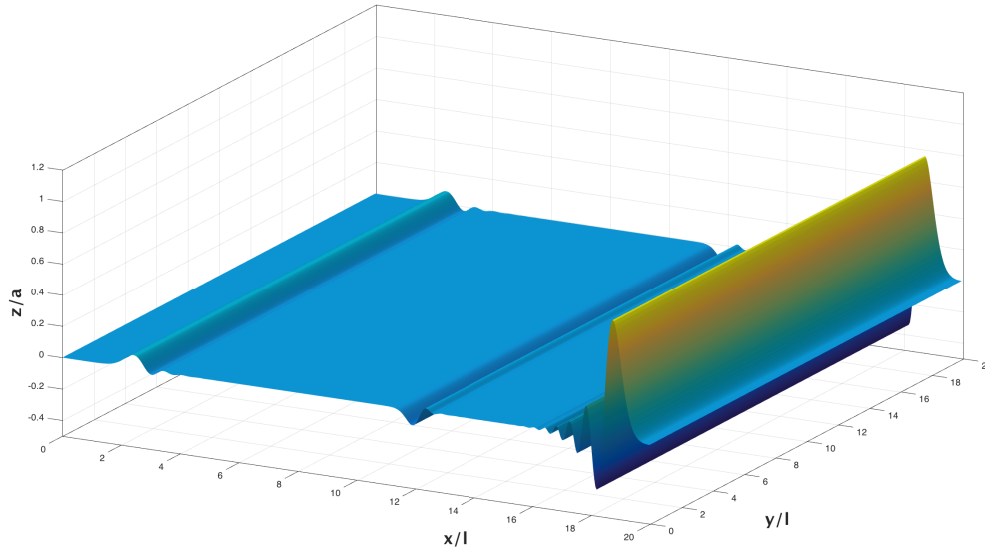


Fig. 3.1 A Gaussian pulse over a trapezoid in the  $\mu = 0.05$  regime.

It is clearly seen in Figure (3.1) that our Non-Local three dimensional algorithm behaved as expected, it reproduced the behavior of the two dimensional case, and a comparison between the central slice of the wave and the result of Figure (2.1) yielded an absolute

difference of  $3.31 \times 10^{-4}$ . This successfully benchmarks our three dimensional numerical routine in this case.

Now we turn into a fully three dimensional situation, we will simulate the motion of a plane, gaussian pulse, and its interaction with a circular underwater obstacle. As a product of the interaction with the obstacle we expect that a non trivial dynamics in the transversal direction will emerge giving rise to a refraction pattern.

### 3.3 Refraction

Refraction accounts for the following type of phenomenon: An observer is located on a coastal region, may observe that waves seem to break on a line nearly parallel to the shoreline, despite the fact that waves come from deep ocean in a rather unorganized way, but as they reach the shoreline wave crests align along parallel lines to the beach. This type of phenomenon, the change of direction of the propagation of a wave due to variations in the medium (from deep water to shallow water) is what is known as refraction.

In order to understand linear water waves over a *slowly varying* topography we make use of an asymptotic theory that predicts such behavior. This theory is known as ray theory because of its resemblance to light and optics, and it describes how the phase of the wave (the position of peaks and troughs) bends as the waves propagates from one medium to another.

If we denote by  $\theta$  the phase function of the wave then the equation that determines how the function bends is the Eikonal equation,

$$\theta_x^2 + \theta_y^2 = \sigma^2. \quad (3.15)$$

This equation determines the phase function  $\theta$  from the given function  $\sigma$  which contains the topographic information. In appendix A we explain how this equation is obtained out of potential theory equations.

This equation is a first order partial differential equation that can be solved by the method of characteristics. The characteristic lines of this equation are called rays and the Eikonal equation forces the level lines of the function  $\theta$  to be orthogonal to the rays.

As the rays propagate through the medium they bend according to the topographic variations of the bottom of the fluid and typically they form *caustics*. The problem with the approximate equations that comprises the theory of refraction is that they are no longer valid near caustics because the first order approximation of the amplitude tends to infinity near the caustics.

Our objective in the next sections is to use our three dimensional non-local method to simulate the refraction of a plane wave as it passes over a circular mountain and a circular cavity.

### 3.3.1 Convex lens

In this section we are going to use our Non-Local method to study the following situation. Set an initial Gaussian plane wave on a region of constant depth, let the plane wave evolve until it passes over a circular underwater mountain as in Figure (3.2), and discuss the changes undergone by the wave field.

The parameters of the simulation are the following:

- The dimensions of the domain are  $L_x = 20$  and  $L_y = 10$ .
- The number of points in each direction is  $N_x = N_y = 2^9$ .
- The value of the dispersion parameter is  $\mu = 0.1$ .
- The final time is  $T_f = 18.3$ . The simulation was actually originally longer but we have to stop it at this time to avoid interference with the periodic boundary.
- The initial velocity potential is given by the equation

$$\varphi_0(x, y) = e^{-\frac{1}{2}\left(\frac{x-c}{\sigma}\right)^2}. \quad (3.16)$$

This Gaussian is centered at  $c = 1$  and has a standard deviation of  $\sigma = 1/6$ .

- The initial wave profile is given by

$$\hat{\eta}_0(\mathbf{k}) = \left( \frac{k \tanh(k\mu)}{\mu} \hat{\varphi}_0(\mathbf{k}) \right). \quad (3.17)$$

- The cut off parameters were set to  $M_x = M_y = 110$ .
- For the time integration we used the fourth order Runge-Kutta algorithm with time step  $dt = 1/30$ .
- The circular mountain has a very specific shape for it corresponds to a modified *Luneburg* lens given by

$$H(r) = \begin{cases} \frac{\alpha^2}{\alpha^2 + 1 - \left(\frac{r}{r_0}\right)^2}, & \text{if } \|\mathbf{x}\| < r_0, \\ 0, & \text{if } \|\mathbf{x}\| \geq r_0. \end{cases}$$

In this function  $\alpha$  is a free positive parameter and  $r_0$  is the radius of the lens. This type of lens has the particular property that it focuses light in a single point outside or inside the lens depending on  $\alpha > 1$  or  $\alpha < 1$  respectively.

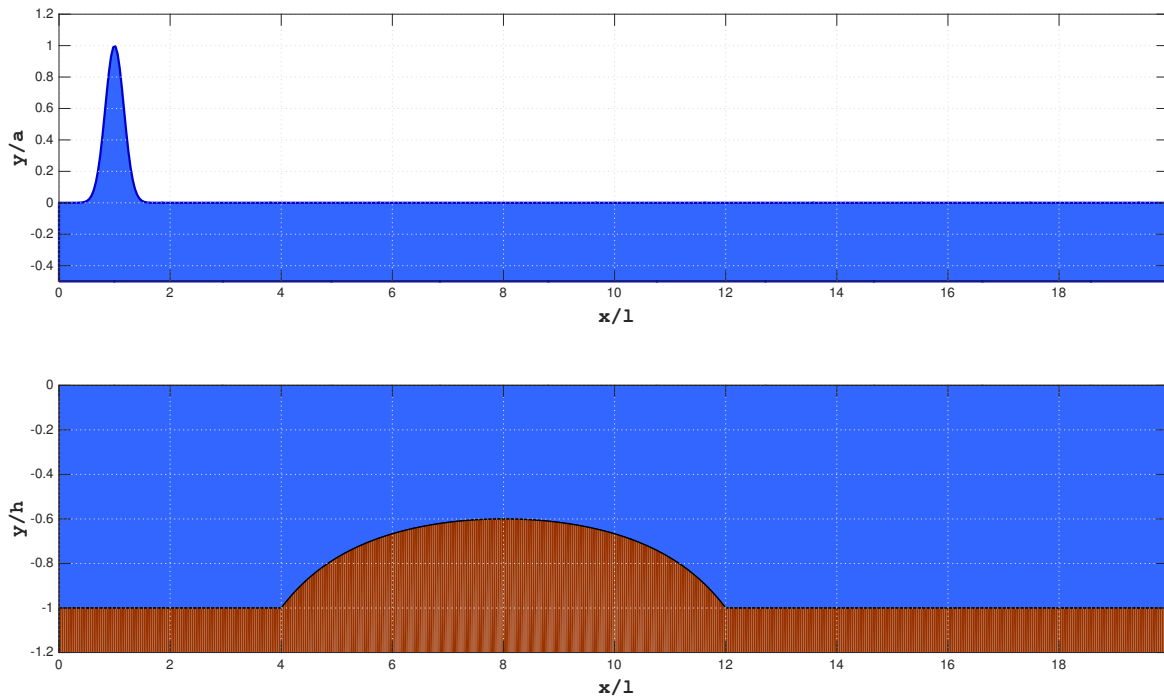


Fig. 3.2 Upper Figure: A Gaussian plane wave over a circular mountain in the  $\mu = 0.1$  regime. Lower Figure: configuration of the underwater mountain. Only the central slice is shown.

### Simulation one

In the following instances, see Figure (3.3), we set  $r_0$  to be 4 units of length and  $\alpha = 1.22$ . In Figure (3.3) we see how the bottom topography focuses water waves.

In the first row the panels display the solution at time  $t = 3.1$  together with a contour plot of its level lines and the red circle shows where the mountain is, at this time we see that the wave moved forward without any change while the interaction with the topography begins.

At time  $t = 8.6$  the interaction with the underwater topography becomes visible. We see how the middle part of the wavefront is lagging behind its lateral part, creating a distortion of the wave field.

Five units of time ahead, at time  $t = 13.6$ , the wavefront is focused by the topography generating a peak of high amplitude towards the end of the circular mountain. Moreover the

level lines show how the wavefront wraps around the focal point, whereas the lateral parts of the wave field keep moving forward.

This type of pattern is what the theory of refraction predicts with its Eikonal equation. The rays bend towards a point whereas the wave front wraps around the focal point. At the focal point, where the rays meet, a caustic begins and so the refraction theory no longer remains valid, this is where the simulation proves useful, for it allows us to appreciate the dynamics beyond the ray theory predictions.

At time  $t = 17$  the simulation was stopped in order to avoid the interference with the periodic boundary and the resulting wave field is shown in the fourth panel of Figure (3.3).

### Simulation two

When the parameter  $\alpha$  in the Luneburg lens is less than one, the focal point moves inside the lens and so in order to simulate this new focalization effect, we changed the value of  $\alpha$  from 1.22 to 0.8. This change in the parameter  $\alpha$  increases the height of the mountain from 0.4 to 0.52. In Figure (3.4) we display the result of the corresponding simulation.

The first panel, at time  $t = 3.1$ , is identical to that of Figure (3.3), where it is shown the motion of the wave before the interaction with the topography begins.

The second panel, at time  $t = 8.6$ , displays a much stronger deformation of the wave field due to its interaction with the underwater mountain.

At time  $t = 13.6$  we see how the wave front has been focused forming a large amplitude peak inside the red circle, showing the focusing property of the Luneburg lens, moreover the level lines show that the smaller waves behind the wave front also follow this focusing feature of the lens.

This high amplitude peak is forced to move down by gravity while the smaller waves focus behind it thus giving rise to a circular pattern that eventually dominates the form of the wave field, at time  $t = 17$ .

This two simulations show that the non-local method is able to simulate the refraction of waves due to interaction with the bottom. The refraction patterns obtained, qualitatively, match with our original intuition and so becomes an indication that we were able to simulate the focusing of waves due to the Luneburg lens.

### Simulation three

In order to appreciate the special refraction properties of the Luneburg lens we compare them with the refraction properties of the parabolic lens. A new simulation is carried out with

a parabolic mountain of circular base of radius  $r_0 = 4$  and its height, from the bottom, is  $h = 0.4$ . The parabolic obstacle is given by:

$$H(r) = \begin{cases} h \left(1 - \frac{\|\mathbf{x}\|^2}{r_0^2}\right), & \text{if } \|\mathbf{x}\| < r_0, \\ 0, & \text{if } \|\mathbf{x}\| \geq r_0. \end{cases} \quad (3.18)$$

We want to explore what differences may arise when the Luneburg lens focuses outside the lens and its corresponding parabolic analog. The result of the simulation is given in Figure (3.5).

Surprisingly, there is almost no difference between the parabolic lens and Luneburg lens. The first row, that displays the incoming wave is exactly the same as in Figure (3.3) and at time  $t = 8.6$  where similar refraction patterns are shown.

At time  $t = 13.6$  only small discrepancies, between the wave field of Figure (3.5) and Figure (3.3), appear, showing that the focalization effect is similar in both cases.

#### Simulation four

The last simulation for this section compares the Luneburg lens that focuses inside the lens, Figure (3.4), with its parabolic counterpart. The resulting simulation is shown in Figure (3.6).

We are in the same situation as in simulation three, where we got almost no difference between the refraction pattern of the wave field at time  $t = 3.1$  and  $t = 8.6$ , as shown in Figures (3.6) and (3.4).

The big difference that arises between both simulations is seen at time  $t = 13.6$  when the focusing takes place. In the Luneburg lens we have that the wave field focalizes around one single point inside the lens whereas in the parabolic case a sequence of peaks takes place inside the lens.

This comparison reveals that the focusing property, inside the lens, is a special characteristic of the Luneburg lens that is not present in the parabolic case.

#### Technical details of the simulations

All the previous simulations were performed with the Non-Local method with the truncations explained on the previous chapter. We used 512 equally spaced collocation points in physical space on both the  $x$  and  $y$  axis. And we truncated the Dirichlet-to-Neumann operator to the first 110 frequencies in both  $x$  and  $y$  directions.

This amounts to compute a matrix of size  $47960 \times 47960$  as already explained. The computation was performed using *Matlab*'s parallel toolbox that allows the computation of such a large matrices.

### 3.3.2 Concave lens

All the obstacles considered so far represented circular mountains. Now we investigate the possibility of an underwater hole rather than a mountain.

What we anticipate from our experience with water waves is that waves move faster in deeper regions, so we expect the wave front to bend forward in the direction of propagation. In this case the topography will speed up the wave, just the opposite of the previous section where the wave was slowed down by its interaction with the topography.

We did two simulations, one with the Luneburg lens and the other one with its corresponding parabolic analog. The parameters used in the simulations were:

- The dimensions of the domain are  $L_x = 20$  and  $L_y = 20$ .
- The number of points in each direction is  $N_x = N_y = 2^9$ .
- The value of the dispersion parameter is  $\mu = 0.1$ .
- The final time is  $T_f = 17$ . The simulation was actually originally longer but we had to stop it at this time to avoid interference with the periodic boundary.
- The initial velocity potential is given by the equation

$$\varphi_0(x, y) = e^{-\frac{1}{2}\left(\frac{x-c}{\sigma}\right)^2}. \quad (3.19)$$

This Gaussian is centered at  $c = 1$  and has a standard deviation of  $\sigma = 1/6$ .

- The initial wave profile is given by

$$\hat{\eta}_0(\mathbf{k}) = \left( \frac{k \tanh(k\mu)}{\mu} \hat{\varphi}_0(\mathbf{k}) \right). \quad (3.20)$$

- The cut off parameters were set to  $M_x = M_y = 110$ .
- For the time integration we used the fourth order Runge-Kutta algorithm with time step  $dt = 1/30$ .
- The Luneburg lens has  $\alpha = 0.8$  and maximum depth of  $H(0) = 1.48$ .
- The paraboloid had a maximum depth of 1.48 and the circular radius was  $r_0 = 4$ .

### Simulation five

The simulation corresponds to an inverted Luneburg lens and it is given in Figure (3.7) and the simulation corresponding to an inverted paraboloid is shown in Figure (3.8). This simulations turned out to be similar so we put them together and discuss their similarities.

At time  $t = 3.1$  we have the usual incoming plane wave that moves forward and still did not interact with the topography.

The first different and new feature arises at time  $t = 8.6$  where we see the refraction pattern happening in the opposite direction, the wavefront bends forward instead of lagging behind with respect to the lateral parts.

At time 13.6 we see in Figures (3.7) and (3.8), that the wave front has bent forward and has sped up as expected, whereas a sequence of peaks has appeared near the edge of the cavity and has propagated off the red circle along a straight line, in this sequence of peaks we encounter the regions of higher oscillations of the wave field, and notice that this region is not in front of the underwater cavity but it appeared towards the edges.

A second noticeable thing is the similarity between Figures (3.7) and (3.8), compared with their “positive” counter parts of Figures (3.4) and (3.6) respectively. This similarity suggests that the wave topography interaction is weaker in the case of a hole than in the case of a mountain.

This weaker interaction is to be expected because of the following reason, near the edge of the paraboloid, both the Luneburg and paraboloidal cavities are similar, being their differences more disparate as one approaches the maximum depth region. However deeper regions play a secondary role on wave propagation and thus the similarity between both simulations.

### 3.3.3 Ray Tracing

In this section we will study in detail the refraction pattern of the Luneburg lens from a theoretical point of view. Our approach follows that of Johnson and Dingemans, see [15, 8], and consists on a system of three equations that asymptotically determine the refraction pattern of a wave train as it propagates with a constant frequency  $w$ . Assume that the wave train is described as

$$\varphi(x, y, t) = a(x, y)e^{i(\theta(x, y) - wt)}. \quad (3.21)$$

Then the equations that determine the phase  $\theta$  and the amplitude  $a$  are:

$$\begin{aligned} w^2 &= \frac{\sigma}{\mu} \tanh(\mu(1 + H(x, y))\sigma), \\ \theta_x^2 + \theta_y^2 &= \sigma^2, \\ \nabla \cdot (\mathbf{c}_g a^2) &= 0. \end{aligned} \tag{3.22}$$

The first equation is an  $\mathbf{x}$  dependent dispersion relation that determines the function  $\sigma(\mathbf{x})$  which is then used to solve the Eikonal equation for the phase function  $\theta$  whereas the third equation determines the amplitude of the wave train. Because we are interested in the geometry of the wave field, which is determined by the phase, we will study the first and second equations of (3.21) only.

### Flat Bottom Case

We begin our study with the flat bottom case,  $H(x, y) = 0$ , and show that in this case certain solutions to the refraction equations coincide with the exact solutions to the linear water wave equations.

Assume that along a given straight line

$$k_1 x + k_2 y = c,$$

the amplitude and phase of the wave train (3.21) are constant, with values  $a_0$  and  $\theta_0$ . We want to solve the Cauchy problem for the refraction equations subject to these initial data.

From the first equation, when  $H = 0$ , we recover the usual dispersion relation that relates the norm of the wave number with the frequency,

$$w^2 = \frac{\sigma}{\mu} \tanh(\mu \sigma).$$

So the quantity  $\sigma$  is determined as the unique positive solution to this equation.

In general the Cauchy problem for the Eikonal equation can be solved with the method of characteristics, which in this case, reduces to the following systems of ordinary differential

equations

$$\begin{aligned}
\frac{dx}{d\tau} &= 2p, \quad \text{with } x(0, s) = x_0(s). \\
\frac{dy}{d\tau} &= 2q, \quad \text{with } y(0, s) = y_0(s). \\
\frac{dz}{d\tau} &= 2\sigma^2, \quad \text{with } z(0, s) = \theta_0. \\
\frac{dp}{d\tau} &= 0, \quad \text{with } p(0, s) = p_0(s). \\
\frac{dq}{d\tau} &= 0, \quad \text{with } q(0, s) = q_0(s).
\end{aligned} \tag{3.23}$$

In these equations the initial data must satisfy the following conditions:

$$\begin{aligned}
k_1 x_0(s) + k_2 y_0(s) &= c, \\
p_0^2(s) + q_0^2(s) &= \sigma^2, \\
p_0(s)x_0'(s) + q_0(s)y_0'(s) &= 0.
\end{aligned} \tag{3.24}$$

From these constraints on the initial data we can choose  $p_0(s) = k_1\sigma/\|(k_1, k_2)\|$  and  $q_0(s) = k_2\sigma/\|(k_1, k_2)\|$  as initial conditions for the system of O.D.E. system (3.23). These restrictions on the initial data are sufficient conditions that ensure that the solution of the system of O.D.E. is a solution to the Eikonal equation.

We can make one further simplification by letting the initial vector  $(k_1, k_2)$ , which defines the initial straight line, to have norm  $\|(k_1, k_2)\| = \sigma$ .

The characteristic lines, given parametrically as  $(x(\tau), y(\tau))$ , are straight lines with direction given by the vector  $(p_0, q_0)$ , which is parallel to the vector  $(k_1, k_2)$ , and it is orthogonal to the initial straight line. Integrating the O.D.E along each characteristic line, we determine the phase function:

$$\theta(x, y) = \theta_0 + p_0(x - x_0) + q_0(y - y_0) = (k_1x + k_2y) + \theta_0. \tag{3.25}$$

Along a ray the amplitude function  $a^2$  satisfies that

$$\frac{d}{d\tau} (a^2(x(\tau), y(\tau))) = \nabla(a^2) \cdot \left( \frac{dx}{d\tau}, \frac{dy}{d\tau} \right) = 2(k_1, k_2) \cdot \nabla(a^2) = 0, \tag{3.26}$$

because the vector  $\mathbf{c}_g$  is parallel to the direction of propagation  $(k_1, k_2)$ . So the amplitude remains constant along any ray.

Finally we obtain that the solution of the Cauchy problem for the refraction equations is

$$\varphi(x, y, t) = ae^{i(k_1x + k_2y + \theta_0 - \omega t)}. \tag{3.27}$$

If one multiplies (3.27) by  $\cosh(\mu\sigma(z+1))$  then the new function

$$\varphi(x, y, z, t) = a \cosh(\mu\sigma(z+1)) e^{i(k_1x + k_2y + \theta_0 - wt)}, \quad (3.28)$$

is a solution to the linear water wave problem (1.18).

### Uneven Bottom Case

What we do now is to solve the Cauchy problem to Eikonal equation, as described on the previous section, but now we allow  $H$  to be the Luneburg lens.

The Cauchy problem for the Eikonal equation consists in determining the phase function  $\theta$  from an initial constant data  $\theta_0$  along the  $y$  axis.

In order to solve the Eikonal equation we must determine first the function  $\sigma$  from the dispersion relation

$$w^2 = \frac{\sigma}{\mu} \tanh(\mu\sigma(1+H)). \quad (3.29)$$

Where the function  $H$ , that describes the topography, is given in polar coordinates as

$$H(r) = \begin{cases} \frac{\alpha^2}{\alpha^2 + 1 - (\frac{r}{r_0})^2}, & \text{if } \|\mathbf{x}\| < r_0, \\ 0, & \text{if } \|\mathbf{x}\| \geq r_0. \end{cases} \quad (3.30)$$

In our case  $r = \sqrt{(x-8)^2 + (y-5)^2}$ , and  $r_0 = 4$ . Notice that outside the circle  $r = r_0$ ,  $H$  vanishes in therefore in that region the solution to (3.29) is given by a constant  $\sigma_0$ .

Once the function  $\sigma$  is determined the characteristic equations are

$$\begin{aligned} \frac{dx}{d\tau} &= 2p, & \text{with } x(0, s) &= 0. \\ \frac{dy}{d\tau} &= 2q, & \text{with } y(0, s) &= s. \\ \frac{dp}{d\tau} &= \frac{\partial \sigma^2}{\partial x}, & \text{with } p(0, s) &= p_0(s). \\ \frac{dq}{d\tau} &= \frac{\partial \sigma^2}{\partial y}, & \text{with } q(0, s) &= q_0(s). \end{aligned} \quad (3.31)$$

In these equations the initial data must satisfy the following conditions:

$$\begin{aligned} p_0^2(s) &= \sigma_0^2, \\ q_0(s) &= 0. \end{aligned} \quad (3.32)$$

In Figure (3.9) and Figure (3.10) the black lines correspond to the rays computed from (3.31) using the classical fourth-order Runge-Kutta method. Notice how the rays focus into one point inside the lens represented by the red circle. This is the focusing property that distinguishes the Luneburg lens from other types of lens in optics.

Let  $\theta$  be a solution to the Eikonal equation, then from the characteristic equations, we have that the direction vector of the rays is always parallel to the vector  $\nabla\theta$ , therefore the rays are always parallel to the level curves of  $\theta$ .

In Figure (3.9) we plot the rays and the level curves of the solution of the water wave equations, computed with the Non-Local method, as shown in Figure (3.4). Notice that the rays and wave fronts are orthogonal as expected.

In Figure (3.10) we see the focusing of the wave field just on top of the point where the rays meet.

The point where the rays focus is  $(11.21, 5)$  whereas the wave field attains its maximum at the point  $(11.28, 5)$ , a difference of less than 0.07. Moreover the maximum value attained by the wave field is 1.59, about 60% higher than the initial amplitude.

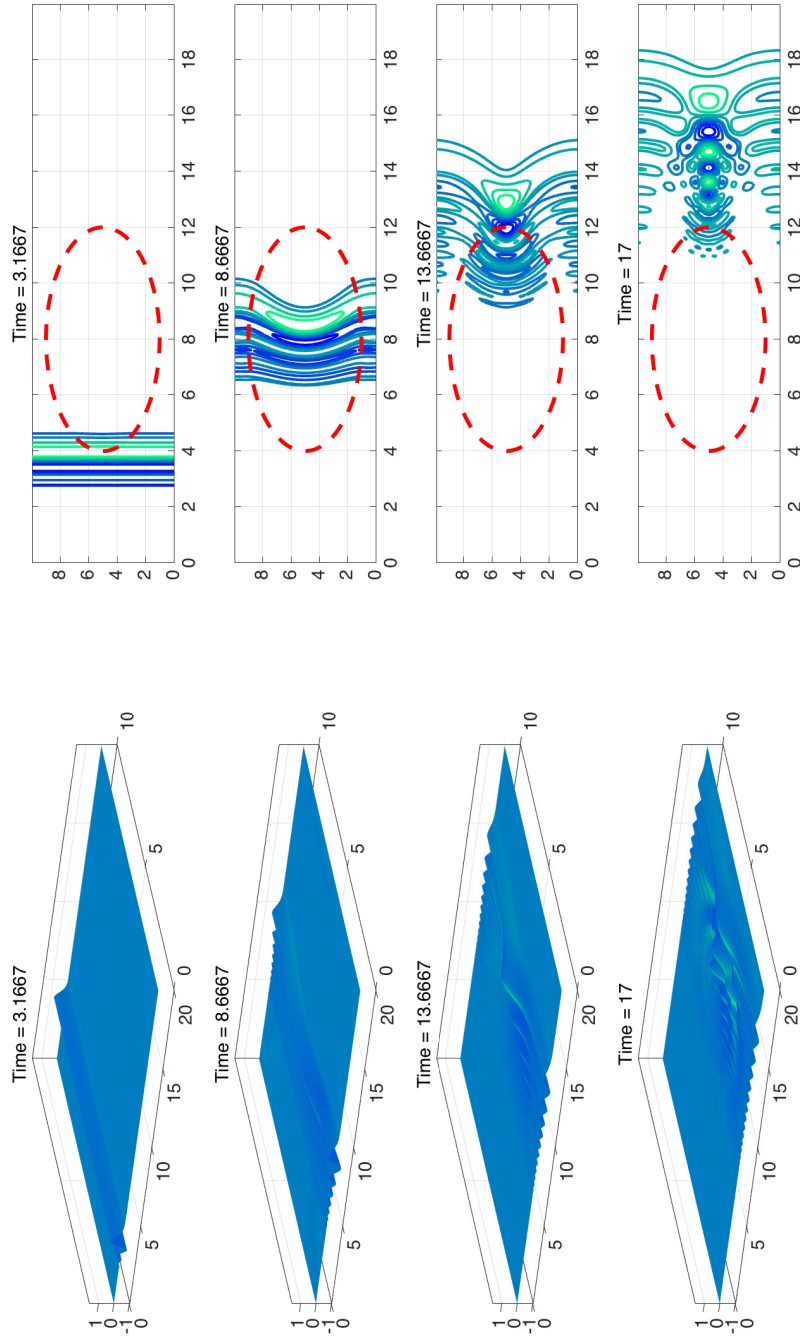


Fig. 3.3 Evolution of a Gaussian pulse over a Luneburg lens with parameters  $\alpha = 1.22$  and height  $0.4$ , in the  $\mu = 0.1$  regime, at times  $t = 3.1, 8.6, 13.6$  and  $17$ .

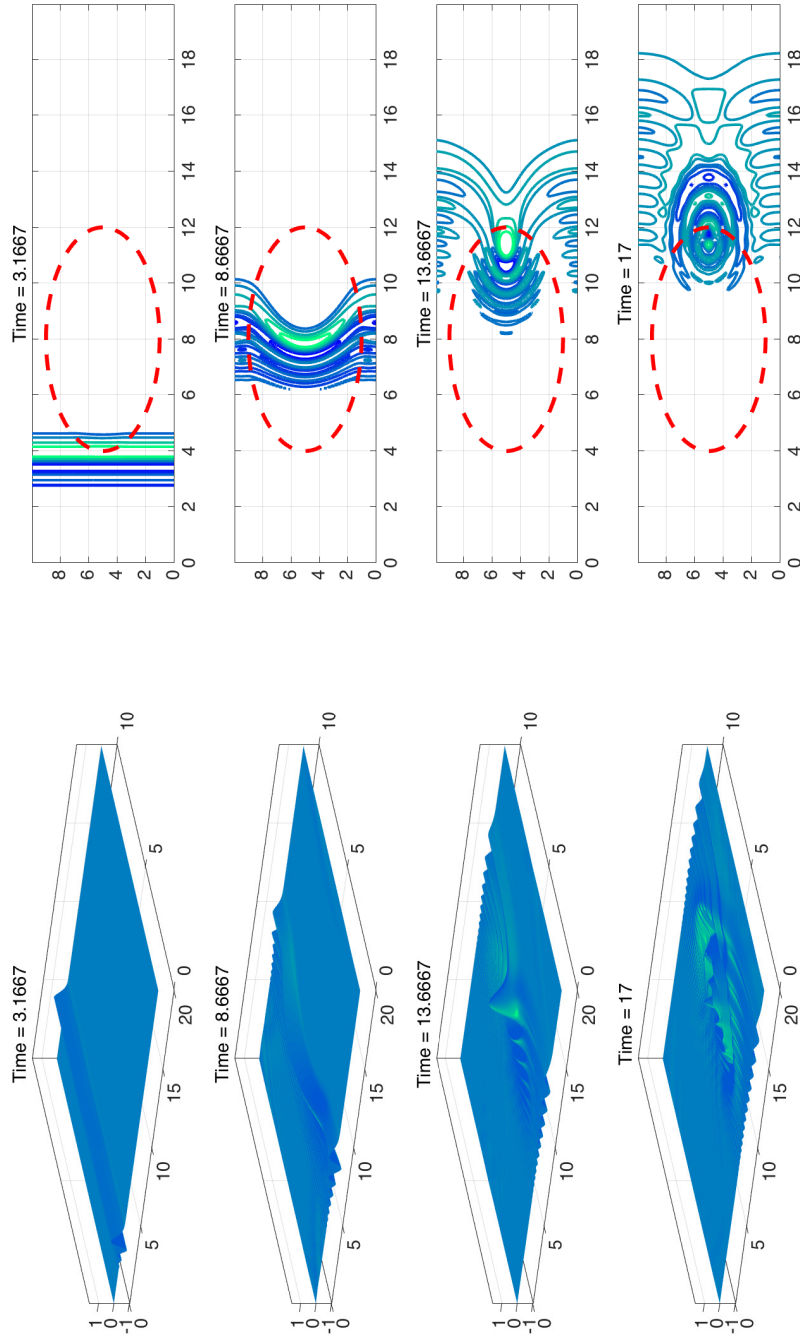


Fig. 3.4 Evolution of a Gaussian pulse over a Luneburg lens with parameters  $\alpha = 0.8$  and height  $0.52$ , in the  $\mu = 0.1$  regime, at times  $t = 3.1, 8.6, 13.6$  and  $17$ . Note the strong focusing effect with the wave peaking in the third graph.

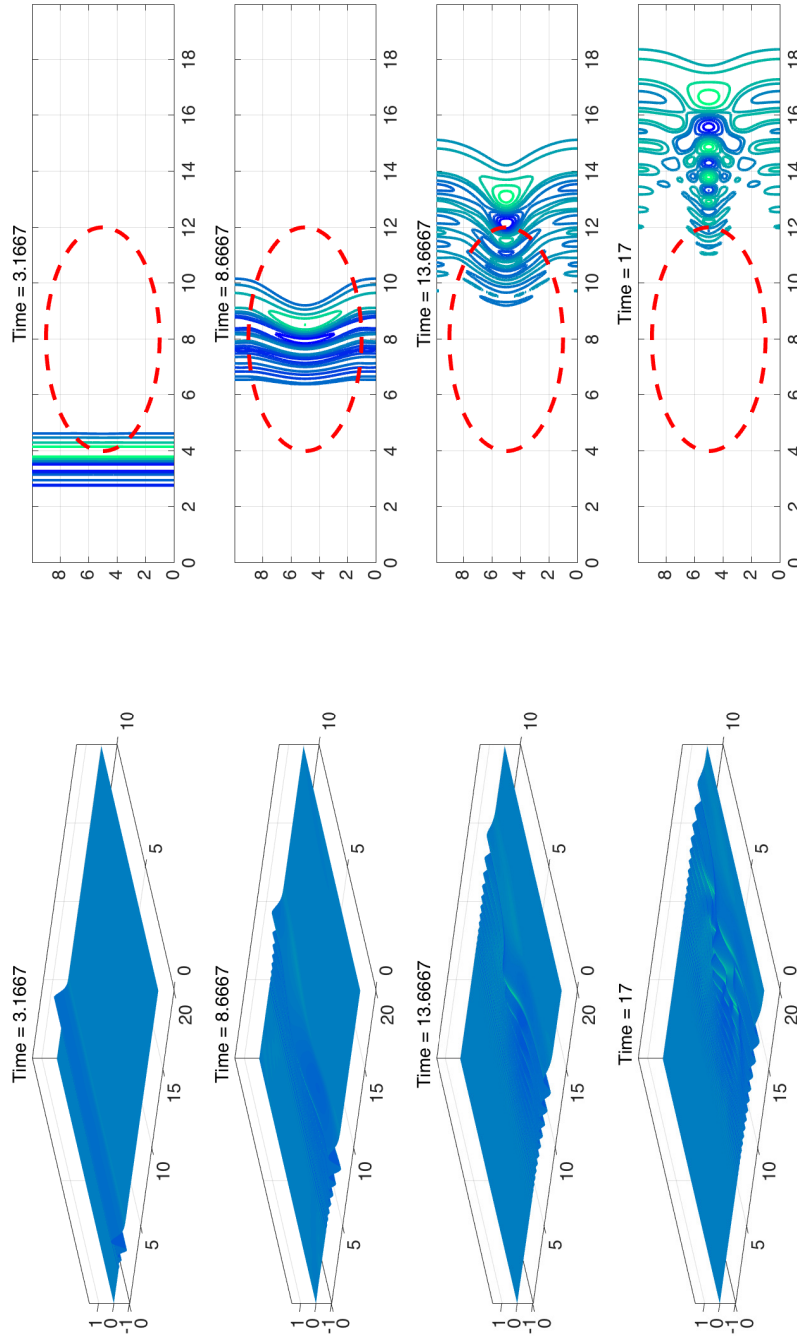


Fig. 3.5 Evolution of a Gaussian pulse over a Parabolic lens with radius 4 and height 0.4, in the  $\mu = 0.1$  regime, at times  $t = 3.1, 8.6, 13.6$  and  $17$ .

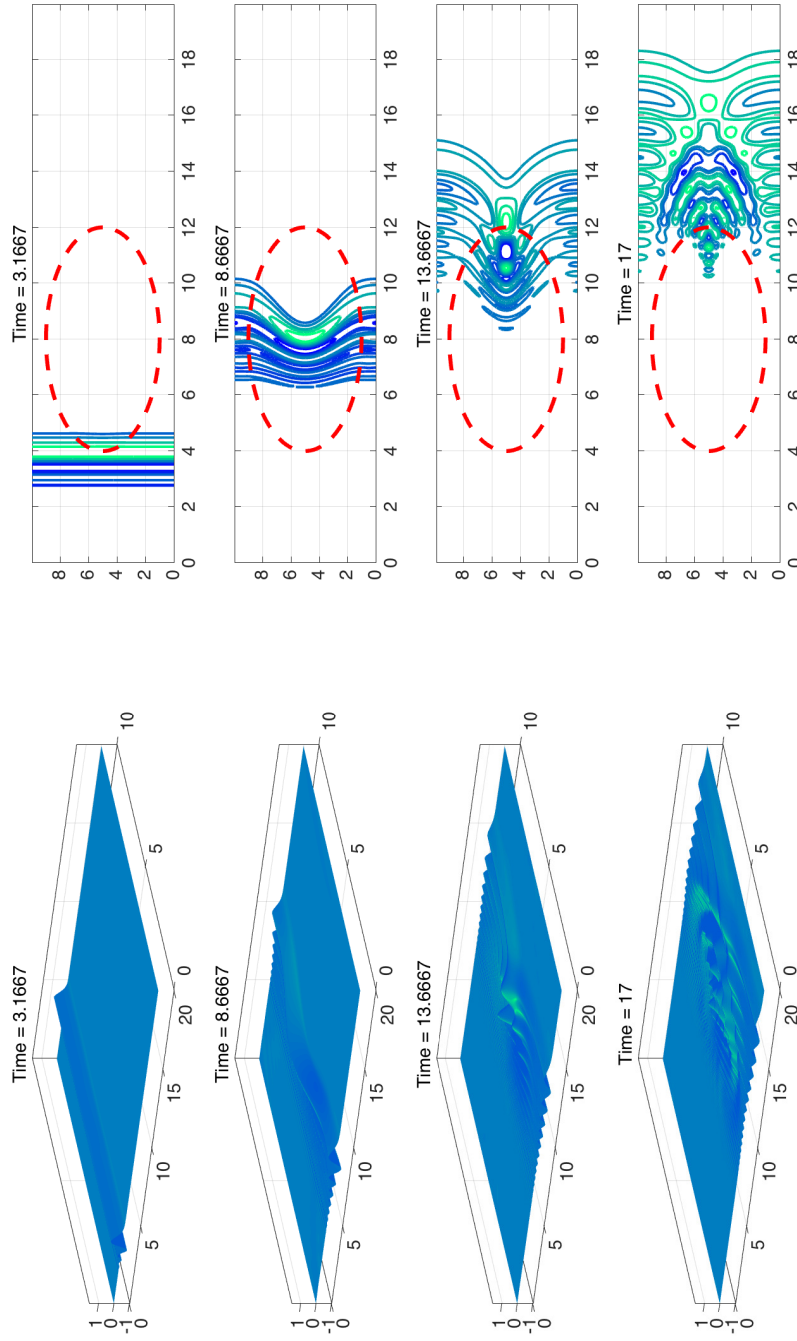


Fig. 3.6 Evolution of a Gaussian pulse over a Parabolic lens with radius 4 and height 0.52, in the  $\mu = 0.1$  regime, at times  $t = 3.1, 8.6, 13.6$  and  $17$ .

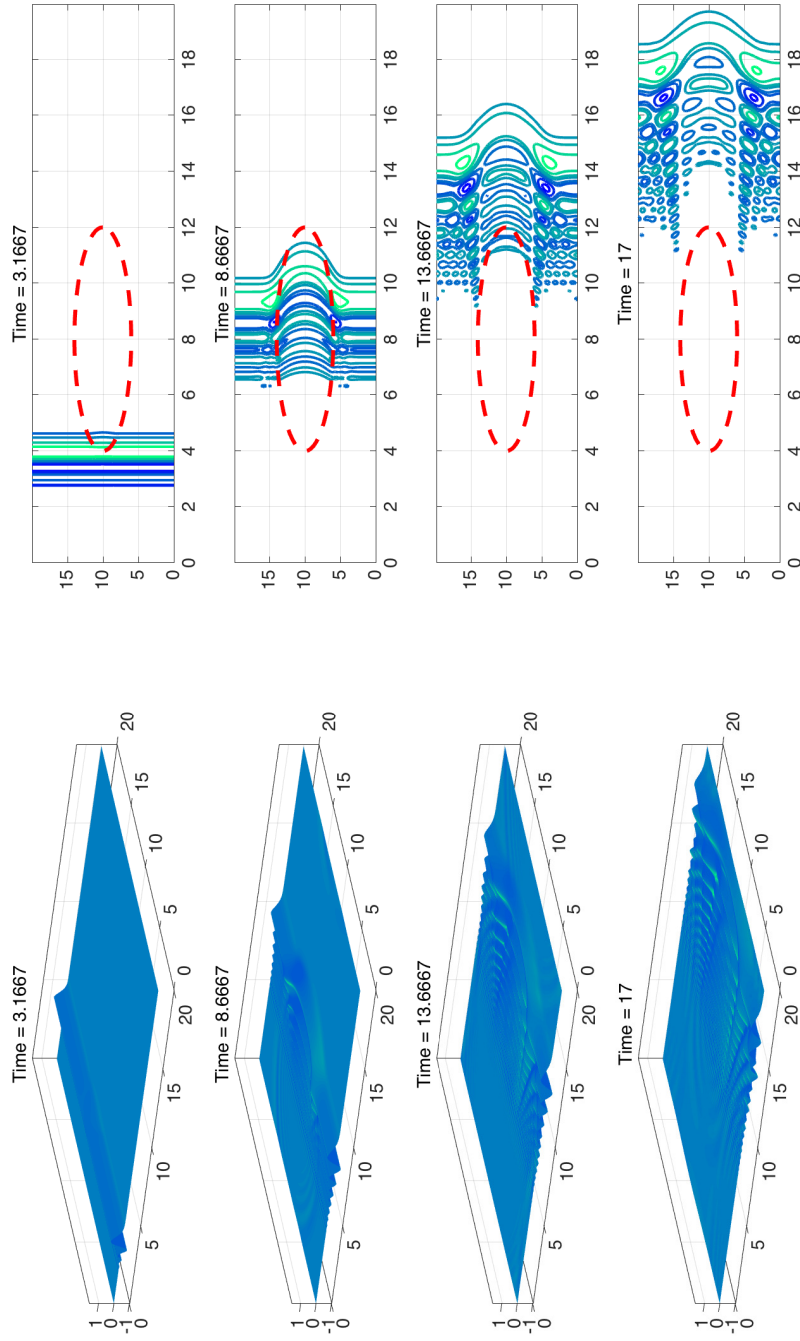


Fig. 3.7 Evolution of a Gaussian pulse over a negative Luneburg lens with parameters  $\alpha = 0.8$  and depth 1.48, in the  $\mu = 0.1$  regime, at times  $t = 3.1, 8.6, 13.6$  and  $17$ .

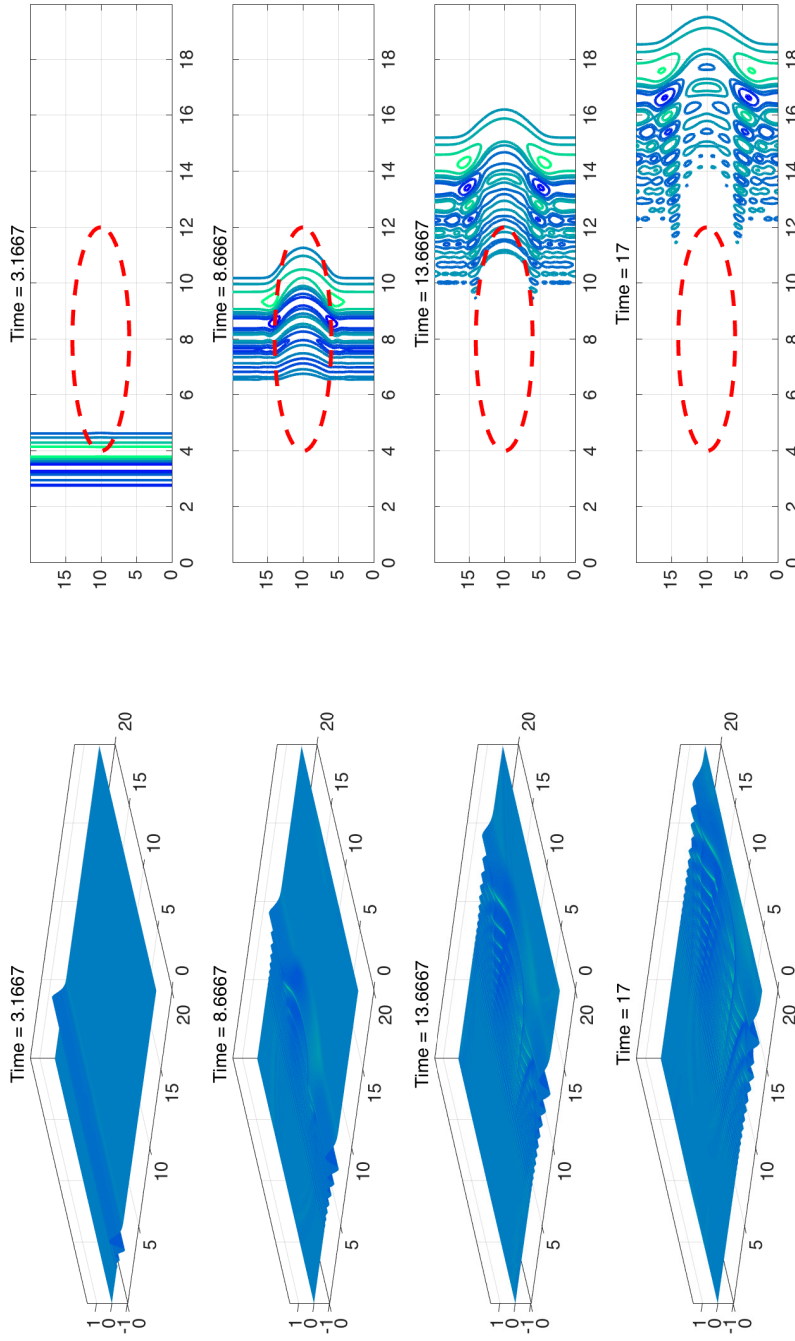


Fig. 3.8 Evolution of a Gaussian pulse over a negative Parabolic lens with radius 4 and depth 1.48, in the  $\mu = 0.1$  regime, at times  $t = 3.1, 8.6, 13.6$  and  $17$ .

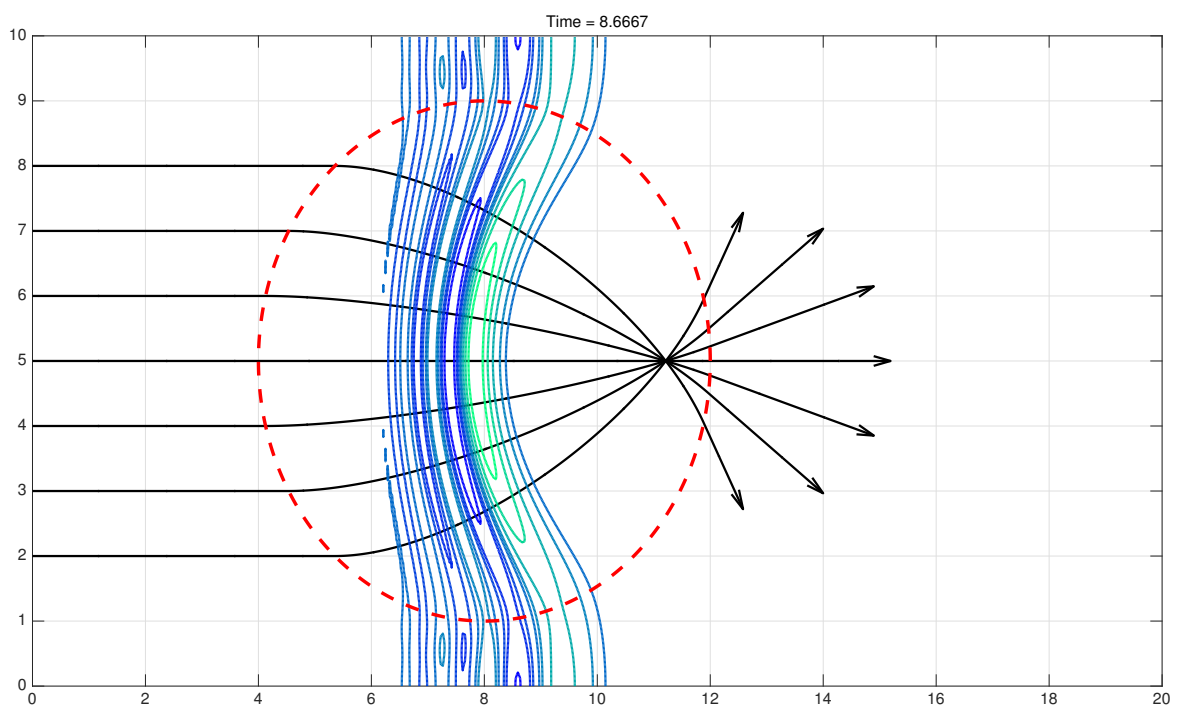


Fig. 3.9 Evolution of a Gaussian pulse over a Luneburg lens with parameters  $\alpha = 0.8$  and height 0.52, in the  $\mu = 0.1$  regime, at time 8.6. The black lines correspond to the rays. Notice that the rays are orthogonal to the level lines.

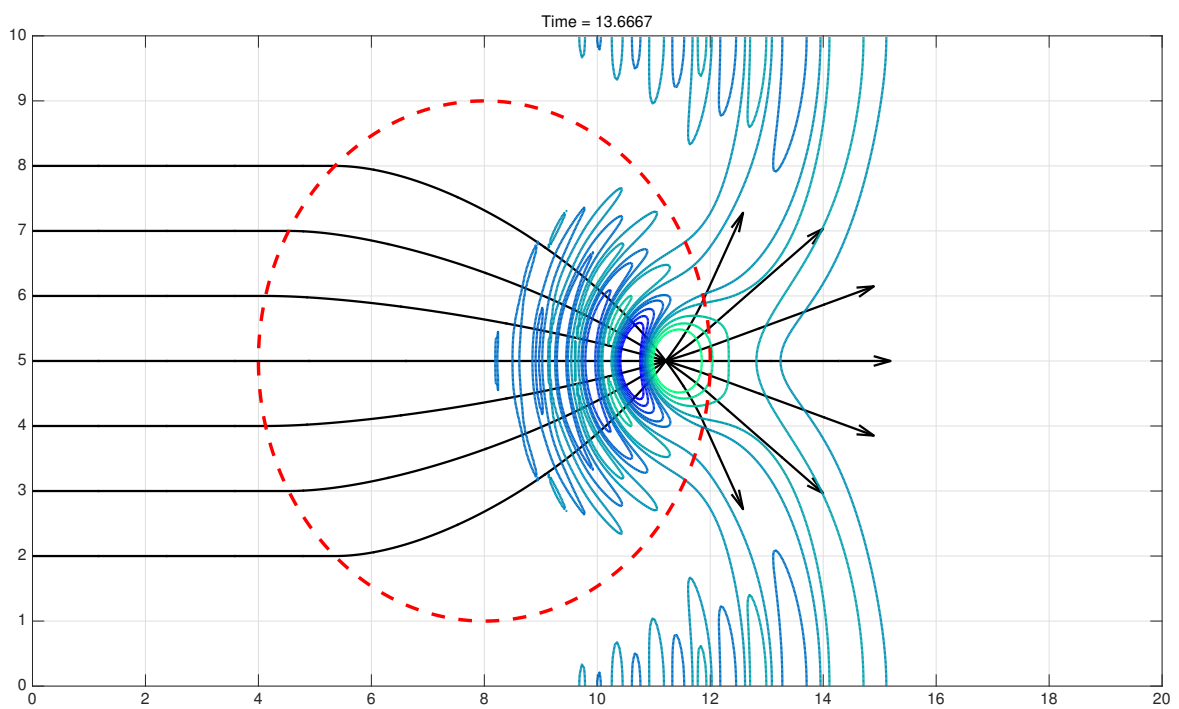


Fig. 3.10 Evolution of a Gaussian pulse over a Luneburg lens with parameters  $\alpha = 0.8$  and height 0.52, in the  $\mu = 0.1$  regime, at time 13.6 . The black lines correspond to the rays. Notice that the wave field focuses on top of the point where the rays meet.

# Chapter 4

## Related problems

### 4.1 A Three Dimensional Boussinesq System with Topography

The goal of this thesis is the study of the wave-topography interaction. In the first three chapters we studied the interaction from the linearized potential theory equations. Now in this chapter we propose a new approach by deriving an approximate model that combines the effects of the topography and non-linearity.

This model provides a generalization to the three dimensional case of the terrain following Boussinesq system proposed by Nachbin in [21].

This Boussinesq model differs from the numerical model presented before in essentially two different ways. The first difference is the inclusion of weak non-linearity, allowing the study of waves of moderate amplitude. The second is a restriction on the topography. We make the assumption that the underwater topography does not vary in the  $y$  direction. Exactly the same setting as in [3].

The derivation of the model is as follows, we begin with the full potential theory equations in cartesian  $x, y, z$  coordinates, 1.1.

$$\begin{aligned}\Delta\phi &= 0 \text{ in } -b(x) < z < \eta(x,y). \\ \frac{\partial\phi}{\partial\vec{n}} &= 0, \text{ on } z = -b(x). \\ \frac{\partial\eta}{\partial t} &= \frac{\partial\phi}{\partial z} - \frac{\partial\phi}{\partial x} \frac{\partial\eta}{\partial x} - \frac{\partial\phi}{\partial y} \frac{\partial\eta}{\partial y}, \text{ on } z = \eta(x,y). \\ \frac{\partial\phi}{\partial t} &= -g\eta - \frac{1}{2} \left( \frac{\partial\phi^2}{\partial x} + \frac{\partial\phi^2}{\partial y} + \frac{\partial\phi^2}{\partial z} \right), \text{ on } z = \eta(x,y).\end{aligned}\tag{4.1}$$

And let the underwater topography be given by

$$b(x) = -h - H(x). \quad (4.2)$$

We make the same assumption on the topography as in 1.3, so no islands nor beaches exist inside the fluid domain.

The first thing we do is to switch to dimensionless variables. This will be very helpful when deriving the approximate Boussinesq equations, in order to accomplish this we denote the physical variables by prime variables and then the dimensionless variables are given by:

$$\begin{aligned} x' &= lx, & y' &= \frac{l}{\gamma}y, & z' &= \frac{h^2}{l}z, & t' &= \frac{l}{\sqrt{gh}}t, \\ \eta' &= a\eta, & \varphi' &= \frac{gla}{\sqrt{gh}}\varphi, & h' &= h(1+H). \end{aligned} \quad (4.3)$$

In these equations  $l$  represents a typical wave length in the  $x$  direction and  $l/\gamma$  represents a typical length in the  $y$  direction.  $h$  denotes a constant depth of reference and variations are represented by the function  $H$ . We define  $\mu = h/l$  to be the dispersion parameter and  $\varepsilon = a/h$  is defined as the non linear parameter. The non dimensional equations become

$$\begin{aligned} \varphi_{xx} + \gamma^2 \varphi_{yy} + \varphi_{zz} &= 0, \quad \text{in } -\mu(1+H) < z < \varepsilon\mu\eta. \\ \varphi_z &= \mu H_x \varphi_x, \quad \text{on } z = -\mu(1+H). \\ \eta_t &= \frac{1}{\mu} \varphi_z - \varepsilon \varphi_x \eta_x - \varepsilon \gamma^2 \varphi_y \eta_y, \quad \text{on } z = \varepsilon\mu\eta. \\ \varphi_t &= -\eta - \varepsilon \frac{1}{2} (\varphi_x^2 + \gamma^2 \varphi_y^2 + \varphi_z^2), \quad \text{on } z = \varepsilon\mu\eta. \end{aligned} \quad (4.4)$$

Now we take advantage of the conformal mapping theory and the specific configuration of the bottom.

The first technical detail that has to be taken into account when using the conformal mapping technique of [21] is that the fluid domain has to be reflected along the rest position  $z = 0$ , so instead of the fluid domain we will consider a symmetric configuration of it.

$$\Omega_r = \{(x, y, z) \in \mathbb{R}^3 \mid -\mu(1+H(x)) < z < \mu(1+H(x))\}. \quad (4.5)$$

If we consider a vertical slice of the reflected fluid domain along the  $x$  axis, then by the special configuration of the bottom we obtain that for each  $y$  the corresponding slices are equal. Notice that each slice represents a simply connected domain because of the hypothesis 1.3.

Using the Riemann mapping theorem we can always find a conformal mapping from a canonical flat strip onto one of the slices of the reflected fluid domain, as the slices are equal for each  $y$  we can use the same conformal mapping and thus build up a diffeomorphism between the three dimensional reflected fluid domain and a three dimensional flat strip.

The diffeomorphism is the following

$$\begin{aligned} F : \{-\mu < z < \mu\} &\longrightarrow \Omega_r \\ F(\xi, y, \zeta) &= (x(\xi, \zeta), y, z(\xi, \zeta)). \end{aligned} \quad (4.6)$$

There is an interesting point here worth mentioning. The functions  $x$  and  $z$  are the real and imaginary parts of a conformal mapping  $x(\xi, \zeta) + iz(\xi, \zeta)$ . Therefore the functions  $x$  and  $z$  are harmonic, as well as the identity function  $y$ , so what we have done is to find harmonic coordinates for the reflected fluid domain  $\Omega_r$ .

In this new coordinates we write down the full potential theory equations.

$$\begin{aligned} \varphi_{\xi\xi} + \gamma^2 J\varphi_{yy} + \varphi_{\zeta\zeta} &= 0, \text{ in } -\mu < \zeta < \mu\epsilon N. \\ JN_t &= \frac{1}{\mu} \varphi_{\zeta} - \epsilon(\varphi_{\xi} N_{\xi} + \gamma^2 J\varphi_y N_y), \text{ on } \zeta = \epsilon\mu N. \\ \varphi_t &= -\eta - \frac{\epsilon}{2J}(\varphi_{\xi}^2 + \gamma^2 J\varphi_y^2 + \varphi_{\zeta}^2), \text{ on } \zeta = \epsilon\mu N. \\ \varphi_{\zeta} &= 0, \text{ on } \zeta = -\mu. \end{aligned} \quad (4.7)$$

In these equations the quantity  $J(\xi, \zeta) = z_{\xi}^2(\xi, \zeta) + z_{\zeta}^2(\xi, \zeta)$  denotes the Jacobian of the conformal application. Notice that the Cauchy-Riemann equations have been used. The function  $\epsilon\mu N(\xi, y)$  denotes the preimage of the free surface  $\epsilon\mu\eta(x, y)$  by the diffeomorphism  $F$ .

Finally we scale the vertical variable  $\zeta$  by  $\mu\zeta$  to get

$$\mu^2(\varphi_{\xi\xi} + \gamma^2 J\varphi_{yy}) + \varphi_{\zeta\zeta} = 0 \quad -1 < \zeta < \epsilon N, \quad (4.8)$$

$$JN_t + \epsilon(\varphi_{\xi} N_{\xi} + \gamma^2 J\varphi_y N_y) - \frac{1}{\mu^2} \varphi_{\zeta} = 0 \quad \zeta = \epsilon N, \quad (4.9)$$

$$J(\varphi_t + \eta) + \frac{\epsilon}{2}(\varphi_{\xi}^2 + \gamma^2 J\varphi_y^2 + \frac{1}{\mu^2} \varphi_{\zeta}^2) = 0 \quad \zeta = \epsilon N, \quad (4.10)$$

$$\varphi_{\zeta} = 0 \quad \zeta = -1. \quad (4.11)$$

It is from equations (4.8) that we begin our deduction of the Boussinesq system. This system is the three dimensional analog of potential theory equations over an  $x$  varying topography. We refer to [21] for the corresponding two dimensional analog which can be

recovered by letting  $\gamma = 0$ . Physically speaking the limit  $\gamma \rightarrow 0$  corresponds to waves that do not vary in the  $y$  direction thus recovering the two dimensional case.

The Boussinesq equations are a simplified model out of the full potential theory equations, that allow the modeling of waves of a moderate amplitude that propagate in the shallow water regime. However for the equations to be valid a certain balance between the dispersion and nonlinearity must be kept. This balance is the following:  $\mathcal{O}(\mu^2) = \varepsilon$ , and  $\varepsilon \ll 1$ .

With this balance at hand we begin the derivation of the model. Our derivation follows that of [22].

The first thing we do is to write down equation (4.9), using (4.8), as

$$JN_t + \frac{\partial}{\partial \xi} \int_{-1}^{\varepsilon N} \varphi_\xi d\zeta + \gamma^2 \frac{\partial}{\partial y} \int_{-1}^{\varepsilon N} J\varphi_y d\zeta = 0. \quad (4.12)$$

Our aim is to simplify the integrands in equation (4.12). In order to do so we use a Taylor series expansion of the velocity potential at the bottom.

$$\varphi(\xi, y, \zeta, t) = \varphi(\xi, y, -1, t) + \frac{(1 + \zeta)^2}{2} \varphi_{\zeta\zeta}(\xi, y, -1, t) + \dots \quad (4.13)$$

We retain up to the second order term  $\varphi_{\zeta\zeta}$ . Notice that the first order term  $\varphi_\zeta$  vanishes by virtue of (4.11), and by (4.8) we assume that  $\varphi_{\zeta\zeta}$  is of order  $\mathcal{O}(\mu^2)$ .

We introduce the following notation  $u_{1b} = \varphi_\xi(\xi, y, -1)$  and  $u_{2b} = \varphi_y(\xi, y, -1)$ , for the horizontal velocities of the fluid at the bottom, in the  $\xi, y, \zeta$  coordinates.

Using equations (4.11) and (4.8) the vertical velocity of the fluid can be represented as

$$\varphi_\zeta = -\mu^2 \left( \frac{\partial}{\partial \xi} \int_{-1}^{\zeta} \varphi_\xi d\zeta + \gamma^2 \frac{\partial}{\partial y} \int_{-1}^{\zeta} J\varphi_y d\zeta \right). \quad (4.14)$$

Usually in the derivation of Boussinesq models a simplification on the vertical velocity of the fluid is made. According to [25] in the classical derivation of the Boussinesq equations, the vertical velocity of the fluid is replaced by an average of the vertical velocities.

In [22] it is proposed a different technique, instead of taking a vertical average of vertical velocities, the vertical structure of the fluid is replaced by the vertical velocity at a fixed depth level. This gives rise to a new parameter, the depth level where the velocity is taken. With this parameter at hand Nwogu estimated the optimal depth level that makes the dispersion relation of the Boussinesq model the closest to the full dispersion relation and obtained an enhanced Boussinesq model.

Following [22] we fix a depth parameter  $\zeta_\alpha$  and denote by  $u_1 = \varphi_\xi(\xi, y, \zeta_\alpha, t)$  and by  $u_2 = \varphi_y(\xi, y, \zeta_\alpha, t)$  the corresponding horizontal velocities at that level. Notice that, because

of the topography, fixing a depth level in  $\zeta$  corresponds to a surface level in the physical domain and not a fixed depth level in the physical space.

In what follows we replace the integrand in (4.12) by  $u_1$  and  $u_2$  and by doing so an error term appears. The error term is estimated by means of (4.13) and (4.14) and from now on we retain terms up to order  $\varepsilon$  and  $\mu^2$ .

We estimate the following difference using (4.13) and the fundamental theorem of calculus

$$\begin{aligned}\varphi_\xi - u_1 &= \int_{\zeta_\alpha}^{\zeta} \varphi_{\xi s}(\xi, y, s, t) ds \\ &= -\mu^2 \left( \int_{\zeta_\alpha}^{\zeta} \frac{\partial}{\partial \xi} \frac{\partial}{\partial \xi} \int_{-1}^s u_{1b} dz + \gamma^2 \frac{\partial}{\partial \xi} \frac{\partial}{\partial y} \int_{-1}^s J(\xi, z) u_{2b} dz ds \right) + \mathcal{O}(\mu^4). \\ \varphi_y - u_2 &= \int_{\zeta_\alpha}^{\zeta} \varphi_{ys}(\xi, y, s, t) ds \\ &= -\mu^2 \left( \int_{\zeta_\alpha}^{\zeta} \frac{\partial}{\partial y} \frac{\partial}{\partial \xi} \int_{-1}^s u_{1b} dz + \gamma^2 \frac{\partial}{\partial y} \frac{\partial}{\partial y} \int_{-1}^s J(\xi, z) u_{2b} dz ds \right) + \mathcal{O}(\mu^4).\end{aligned}\tag{4.15}$$

In particular letting  $\zeta = -1$  we obtain

$$\begin{aligned}u_{1b} - u_1 &= \int_{-1}^{\zeta} \varphi_{\xi s}(\xi, y, s, t) ds \\ &= -\mu^2 \left( \int_{-1}^{\zeta} \frac{\partial}{\partial \xi} \frac{\partial}{\partial \xi} \int_{-1}^s u_{1b} dz + \gamma^2 \frac{\partial}{\partial \xi} \frac{\partial}{\partial y} \int_{-1}^s J(\xi, z) u_{2b} dz ds \right) + \mathcal{O}(\mu^4). \\ u_{2b} - u_2 &= \int_{-1}^{\zeta} \varphi_{ys}(\xi, y, s, t) ds \\ &= -\mu^2 \left( \int_{-1}^{\zeta} \frac{\partial}{\partial y} \frac{\partial}{\partial \xi} \int_{-1}^s u_{1b} dz + \gamma^2 \frac{\partial}{\partial y} \frac{\partial}{\partial y} \int_{-1}^s J(\xi, z) u_{2b} dz ds \right) + \mathcal{O}(\mu^4).\end{aligned}\tag{4.16}$$

Replacing (4.16) into (4.15) we obtain, up to an error term of order  $\mathcal{O}(\mu^4)$ , the estimate we need

$$\begin{aligned}\varphi_\xi &= u_1 + \mu^2 \left( \int_{\zeta_\alpha}^{\zeta} \frac{\partial}{\partial \xi} \frac{\partial}{\partial \xi} \int_{-1}^s u_1 dz + \gamma^2 \frac{\partial}{\partial \xi} \frac{\partial}{\partial y} \int_{-1}^s J(\xi, z) u_2 dz ds \right) + \mathcal{O}(\mu^4). \\ \varphi_y &= u_2 + \mu^2 \left( \int_{\zeta_\alpha}^{\zeta} \frac{\partial}{\partial y} \frac{\partial}{\partial \xi} \int_{-1}^s u_1 dz + \gamma^2 \frac{\partial}{\partial y} \frac{\partial}{\partial y} \int_{-1}^s J(\xi, z) u_2 dz ds \right) + \mathcal{O}(\mu^4).\end{aligned}\tag{4.17}$$

We drop all of the  $\mathcal{O}(\mu^4)$  order terms and substitute equations (4.17) into (4.12), this yields the following expression

$$\begin{aligned}
JN_t + \frac{\partial}{\partial \xi} \int_{-1}^{\varepsilon N} u_1 d\zeta + \gamma^2 \frac{\partial}{\partial y} \int_{-1}^{\varepsilon N} Ju_2 d\zeta &= \\
&= \mu^2 \int_{-1}^{\varepsilon N} \left( \frac{\partial}{\partial \xi} \int_{\zeta_\alpha}^{\zeta} \left( \frac{\partial}{\partial \xi} \frac{\partial}{\partial \xi} \int_{-1}^s u_1 dz + \gamma^2 \frac{\partial}{\partial \xi} \frac{\partial}{\partial y} \int_{-1}^s Ju_2 dz \right) ds \right) d\zeta \\
&+ \mu^2 \gamma^2 \int_{-1}^{\varepsilon N} \left( J \frac{\partial}{\partial y} \int_{\zeta_\alpha}^{\zeta} \left( \frac{\partial}{\partial y} \frac{\partial}{\partial \xi} \int_{-1}^s u_1 dz + \gamma^2 \frac{\partial}{\partial y} \frac{\partial}{\partial y} \int_{-1}^s Ju_2 dz \right) ds \right) d\zeta.
\end{aligned} \tag{4.18}$$

We simplify the right hand side of (4.18) by introducing the following functions

$$G_\alpha(\zeta) = \frac{1}{2} \left( (1 + \zeta)^2 - (1 + \zeta_\alpha)^2 \right), \text{ and } H_\alpha(\xi, \zeta) = \int_{\zeta_\alpha}^{\zeta} \int_{-1}^s J(\xi, z) dz ds, \tag{4.19}$$

and the following notation  $\tilde{\Delta} = \partial_\xi^2 + \gamma^2 J \partial_y^2$ .

$$JN_t + \frac{\partial}{\partial \xi} \int_{-1}^{\varepsilon N} u_1 d\zeta + \gamma^2 \frac{\partial}{\partial y} \int_{-1}^{\varepsilon N} Ju_2 d\zeta = \mu^2 \int_{-1}^{\varepsilon N} \tilde{\Delta}(u_{1\xi} G_\alpha) + \gamma^2 \tilde{\Delta}(u_{2y} H_\alpha) d\zeta. \tag{4.20}$$

The left hand side of this equation (4.20) can be simplified further by noticing that  $u_1$  and  $u_2$  do not depend on the variable  $\zeta$ . The simplified equation is

$$JN_t + (u_1(1 + \varepsilon N))_\xi + \gamma^2 (u_2 \int_{-1}^{\varepsilon N} J d\zeta)_y = \mu^2 \int_{-1}^{\varepsilon N} \tilde{\Delta}(u_{1\xi} G_\alpha) + \gamma^2 \tilde{\Delta}(u_{2y} H_\alpha) d\zeta. \tag{4.21}$$

This equation (4.21) is one of the equations that comprises our Boussinesq system. This equation is a simplified substitute for the kinematic equation (4.9) that takes into account the Laplace's equation with a Neumann boundary condition.

Now we treat the dynamic boundary condition (4.10), up to terms of order  $\mathcal{O}(\varepsilon, \mu^2)$ , the dynamic boundary condition (4.10) can be written as

$$\varphi_t + \eta + \frac{\varepsilon}{2} \left( \frac{u_1^2}{J} + \gamma^2 u_2^2 \right) = \mathcal{O}(\varepsilon \mu^2). \tag{4.22}$$

The time derivative of the potential along the reference level  $\zeta_\alpha$  is related to the potential along the free surface  $\varepsilon N$  as follows. Notice that equation (4.15) is being used in

$$\begin{aligned} \varphi_t(\varepsilon N) &= \varphi_t(\zeta_\alpha) + \int_{\zeta_\alpha}^{\varepsilon N} \varphi_{\zeta t} d\zeta = \\ \varphi_t(\zeta_\alpha) &- \mu^2 \int_{\zeta_\alpha}^{\varepsilon N} \left( \frac{\partial}{\partial \xi} \int_{-1}^{\zeta} u_{1t} d\zeta + \gamma^2 \frac{\partial}{\partial y} \int_{-1}^{\zeta} J u_{2t} d\zeta \right) + \mathcal{O}(\mu^4). \end{aligned} \quad (4.23)$$

Dropping all the higher order terms and retaining the  $\mathcal{O}(\varepsilon, \mu^2)$  terms we get to the following equation

$$(\varphi_\alpha)_t + \eta + \frac{\varepsilon}{2} \left( \frac{u_1^2}{J} + \gamma^2 u_2^2 \right) = \mu^2 \int_{\zeta_\alpha}^{\varepsilon N} \left( \frac{\partial}{\partial \xi} \int_{-1}^{\zeta} u_{1t} d\zeta + \gamma^2 \frac{\partial}{\partial y} \int_{-1}^{\zeta} J u_{2t} d\zeta \right). \quad (4.24)$$

Taking the horizontal gradient of equation (4.24) and retaining only the lower order terms we obtain the following system of equations for the horizontal velocities  $u_1$  and  $u_2$ .

$$\begin{bmatrix} u_{1t} \\ u_{2t} \end{bmatrix} + \begin{bmatrix} \eta_\xi \\ \eta_y \end{bmatrix} + \varepsilon \begin{bmatrix} \left(\frac{u_1^2}{J}\right)_\xi \\ \left(\frac{u_1^2}{J}\right)_y \end{bmatrix} + \varepsilon \gamma^2 \begin{bmatrix} u_2 u_{2\xi} \\ u_2 u_{2y} \end{bmatrix} = \mu^2 \int_{\zeta_\alpha}^{\varepsilon N} \begin{bmatrix} \frac{\partial}{\partial \xi} (u_1 \xi_t (1 + \zeta) + \gamma^2 u_{2yt} F) \\ \frac{\partial}{\partial y} (u_1 \xi_t (1 + \zeta) + \gamma^2 u_{2yt} F) \end{bmatrix} d\zeta. \quad (4.25)$$

In equation (4.25) the auxiliary function  $F$  is a primitive of the Jacobian  $J$ , it is defined via integration as

$$F(\xi, \zeta) = \int_{-1}^{\zeta} J(\xi, z) dz. \quad (4.26)$$

Equations (4.21) and (4.25) comprises our system of Boussines equations, however some further simplifications can be made in order to get a more appealing system of equations. One of the modifications that can be made concerns a simplification of the Jacobian along the free surface  $\varepsilon N$ , and a relation between the functions  $\eta$  and  $N$ .

In the work of [2] and in [21] a simplification for the Jacobian along the free surface is made by considering a Taylor expansion based at the rest position  $z = 0$ ,

$$J(\xi, \varepsilon N(\xi)) = z_\zeta^2(\xi, 0) + \mathcal{O}(\varepsilon^2). \quad (4.27)$$

Notice that the term  $z_\zeta(\xi, 0)$  is a time independent function that depends only on the conformal mapping that flattens out the topography. Also notice that there are no variation along the  $y$  direction because of the configuration of the topography.

The term  $z_\zeta(\xi, 0)$  can be computed directly from the conformal mapping, see [2], and it is usually denoted by  $M(\xi) = z_\zeta(\xi, 0)$ .

In [12] it is shown that the following approximation holds up to order  $\mathcal{O}(\varepsilon^2)$

$$N(\xi, y, t) = \frac{1}{M(\xi)} \eta(x(\xi, 0), y) + \mathcal{O}(\varepsilon^2). \quad (4.28)$$

With both simplifications (4.27) and (4.28) we can simplify our model which now comprises three equations for the three unknowns  $u_1$ ,  $u_2$  and  $\eta$  small,

$$\begin{aligned} M\eta_t + \left(u_1 \left(1 + \varepsilon \frac{\eta}{M}\right)\right)_\xi + \gamma^2 \left(u_2 \int_{-1}^{\varepsilon\eta/M} J d\zeta\right)_y &= \mu^2 \int_{-1}^{\varepsilon\eta/M} \tilde{\Delta}(u_{1\xi} G_\alpha) + \gamma^2 \tilde{\Delta}(u_{2y} H_\alpha) d\zeta, \\ u_{1t} + \eta_\xi + \varepsilon \frac{u_1}{M} \left(\frac{u_1}{M}\right)_\xi + \varepsilon \gamma^2 u_2 u_{2\xi} &= \mu^2 \int_{\zeta_\alpha}^{\varepsilon\eta/M} (u_{1\xi t} (1 + \zeta) + \gamma^2 u_{2yt} F)_\xi d\zeta, \\ u_{2t} + \eta_y + \varepsilon \frac{u_2}{M} \left(\frac{u_2}{M}\right)_y + \varepsilon \gamma^2 u_2 u_{2y} &= \mu^2 \int_{\zeta_\alpha}^{\varepsilon\eta/M} (u_{1\xi t} (1 + \zeta) + \gamma^2 u_{2yt} F)_y d\zeta. \end{aligned} \quad (4.29)$$

The system (4.29) is a generalization of the terrain following Boussinesq system of [21] to the three dimensional setting with a laminated (ridge-like) topography.

There are some good features about the system worth pointing out. The first one concerns the auxiliary functions  $F$ ,  $G_\alpha$  and  $H_\alpha$ . These functions depend on the variables  $\xi$  and  $\zeta$  only. Moreover we need  $-1 < \zeta < \varepsilon\eta/M$  only so we can think of the auxiliary functions as “submarine” known geometry-related coefficients.

In the derivation of (4.29) no assumption has been made on the parameter  $\gamma$ . Yet the limit  $\gamma \rightarrow 0$  is still of physical importance for the following reason.

The Boussinesq systems in general model the dynamics of waves of moderate amplitude in shallow water. In nature a good example where this situation arises is when waves approach the shoreline. This case lies outside the range of validity of the linearized potential theory equations.

As every day experience reveals, when waves approach the shoreline they lined up to the beach giving rise to a rather long lump on the surface of the water. This wave pattern arises when  $\gamma$  goes to zero, so it is reasonable to make further simplifications when assuming that  $\gamma$  is small.

When  $\gamma$  is set to zero we are in the two dimensional regime and if reduce the system (4.29) by removing its  $y$  dependence and putting  $\gamma = 0$ , up to  $\mathcal{O}(\varepsilon, \mu^2)$  terms, then the system (4.29) reduces to

$$\begin{aligned}
M\eta_t + \left(u_1(1 + \varepsilon \frac{\eta}{M})\right)_\xi &= \mu^2 \int_{-1}^{\varepsilon\eta/M} \tilde{\Delta}(u_{1\xi} G_\alpha) d\zeta = \frac{\mu^2}{2} u_{1\xi\xi\xi} \left(\frac{1}{3} - (1 + \zeta_\alpha)^2\right), \\
u_{1t} + \eta_\xi + \varepsilon \frac{u_1}{M} \left(\frac{u_1}{M}\right)_\xi &= \mu^2 \int_{\zeta_\alpha}^{\varepsilon\eta/M} (u_{1\xi t}(1 + \zeta))_\xi d\zeta = -\frac{\mu^2}{2} u_{1\xi\xi t} ((1 + \zeta_\alpha)^2 - 1).
\end{aligned} \tag{4.30}$$

This system is exactly the same system of Nachbin and Muñoz [13], where it is shown how to obtain an improved Boussinesq system by tuning the depth parameter  $\zeta_\alpha$  properly.

If we are back to the three dimensional setting but now we let the topography vanish then  $M = 1$ ,  $\xi = x$  and  $\zeta = z$ . Moreover in this case the auxiliary functions  $H_\alpha = G_\alpha$  and  $F = 1 + \zeta$ . Therefore the system (4.29) reduces to

$$\begin{aligned}
\eta_t + \nabla \cdot ((1 + \varepsilon\eta)\mathbf{u}) &= \frac{\mu^2}{2} (\Delta(\nabla \cdot \mathbf{u})) \left(\frac{1}{3} - (1 + z_\alpha)^2\right), \\
\mathbf{u}_t + \nabla\eta + \varepsilon(\mathbf{u} \cdot \nabla)\mathbf{u} &= \frac{\mu^2}{2} \nabla(\nabla \cdot \mathbf{u}) ((1 + z_\alpha)^2 - 1).
\end{aligned} \tag{4.31}$$

This system is exactly the same as the one in [22] for a flat bottom configuration.

These are relevant consistency checks regarding simpler models showing that these new reduced equations generalize previous known ones. A step in our future research is to compute solutions to these equations with periodic or randomly varying ridge heights. Of particular interest are the cases of wave with an oblique incidence angle regarding the ridge-structure.

## 4.2 The Bouncing Droplet Problem

When a drop of water falls into the surface of the fluid, it does not merge immediately, but a rather interesting process takes place. Instead of merging with the fluid the drop bounces off the surface of the fluid again and again, losing part of its mass at every jump until it fades away inside the fluid. This process happens very fast and that is the reason why it is commonly assumed that the drop merges immediately inside the fluid after contact.

It was found in the laboratory by Couder and his collaborators that when the fluid container was allowed to shake in the vertical direction at a specific frequency and at a specific *amplitude*, the drop never merged inside the fluid but remained bouncing on top of it for large periods of time. The specific forcing acceleration at which the container had to be shaken has to be below but close to the *Faraday threshold*.

The mechanism that keeps the droplet from merging into the fluid is a thin layer of air that remains trapped between the drop and the surface of the fluid. This thin layer of air, as the drop falls down, presses the surface of the fluid which reacts by pressing the air layer up.

When the air layer pushes the fluid surface down it deforms the surface of the fluid through a localized pressure field. So as the droplet oscillates up and down it generates a wave field on the surface of the fluid which in turn keeps the droplet in flight, thus obtaining a wave-particle system.

It was soon discovered that, by tuning the amplitude of the shaker, it was possible to set the droplet in motion at a constant speed along a straight line, it was studied the different *walking* modes at which the droplet moved and their corresponding wave fields.

The dynamics became richer when obstacles were placed in the container inside the fluid. For instance, when a circular corral was placed beneath the surface it reflected the particle back to the enclosed region. When a pillar was put, the incoming straight trajectory of the drop was revolved around the pillar. This interesting phenomena that arises from the interaction of the wave, the droplet and the topography demanded further experiments in order to reveal what other features could appear.

One of the most interesting wave-particle interactions are observed in the case of tunneling where there is a submerged barrier which confines the droplet's dynamics. Sometimes the droplet is able to overcome the barrier and escape the region of confinement. In order to shed some light into this peculiar behavior Eddie, Fort, Moisy and Couder in [10] device an experiment where they studied how the dimensions of the barrier, through its height and thickness, correlate to the tunneling probability.

At this point an important question rises, is it possible to derive a simple model capable of simulating the wave-particle dynamics and reproduce much of the complex behaviors seen in the laboratory.

Our starting point for our research is the model of Milewski, Galeano, Nachbin and Bush see [19], where a modification of the linearized potential theory equations, that includes surface tension and viscosity, is proposed and are very similar to the equations we have been working with. The equations that account for the wave dynamics are

$$\begin{aligned}
 \Delta\varphi &= 0, \quad \text{for } z \leq 0, \\
 \varphi &\rightarrow 0, \quad \text{as } z \rightarrow 0, \\
 \varphi_t &= -g(t)\eta + \frac{\sigma}{\rho} \Delta_H \eta + 2\nu \Delta_H \varphi - \frac{1}{\rho} P_D(x - X(t), t), \quad \text{on } z = 0, \\
 \eta_t &= \varphi_z + 2\nu \Delta_H \eta, \quad \text{on } z = 0.
 \end{aligned} \tag{4.32}$$

In equations (4.32) the vibrations of the container are given by an oscillatory gravity field  $g(t) = g(1 - \Gamma \cos(w_0 t))$ , where the frequency  $w_0 = 80$  Hz and the parameter  $\Gamma$  is the vertical acceleration.

The model of [19], (equations (4.32)), captures most of the effects that we have mentioned so far. It models *bouncers*, *walkers*, it provides a bifurcation diagram between the different walking regimes and it was capable of simulating the interaction between two droplets. The only thing that it is not capable of modeling is the interaction with underwater obstacles. Our goal is that our research, combined with the technique of [19], will give a model that incorporates the effects of the underwater obstacles.

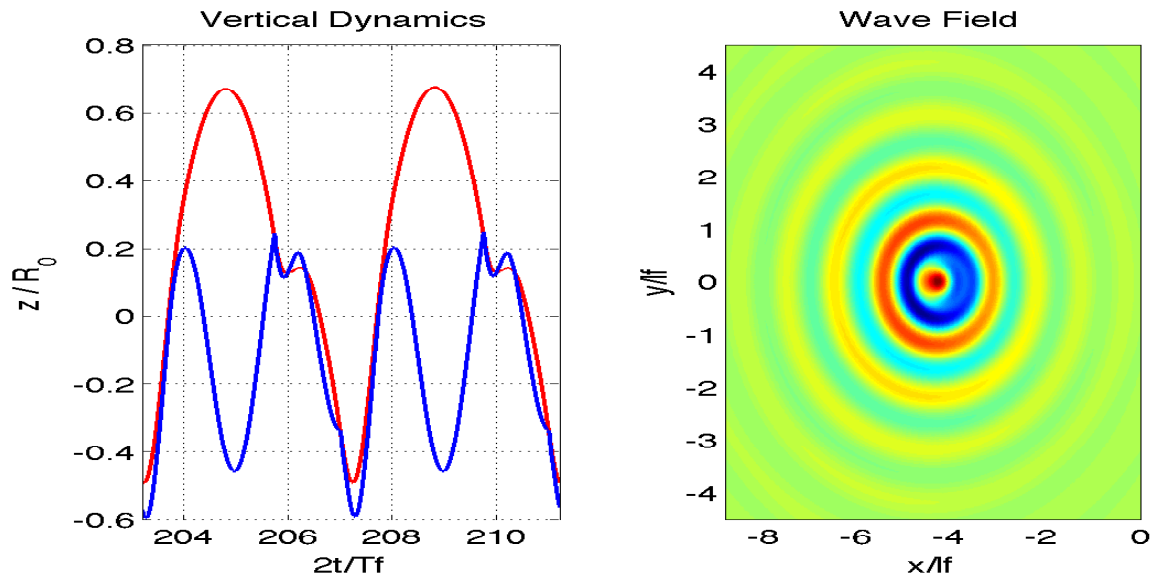
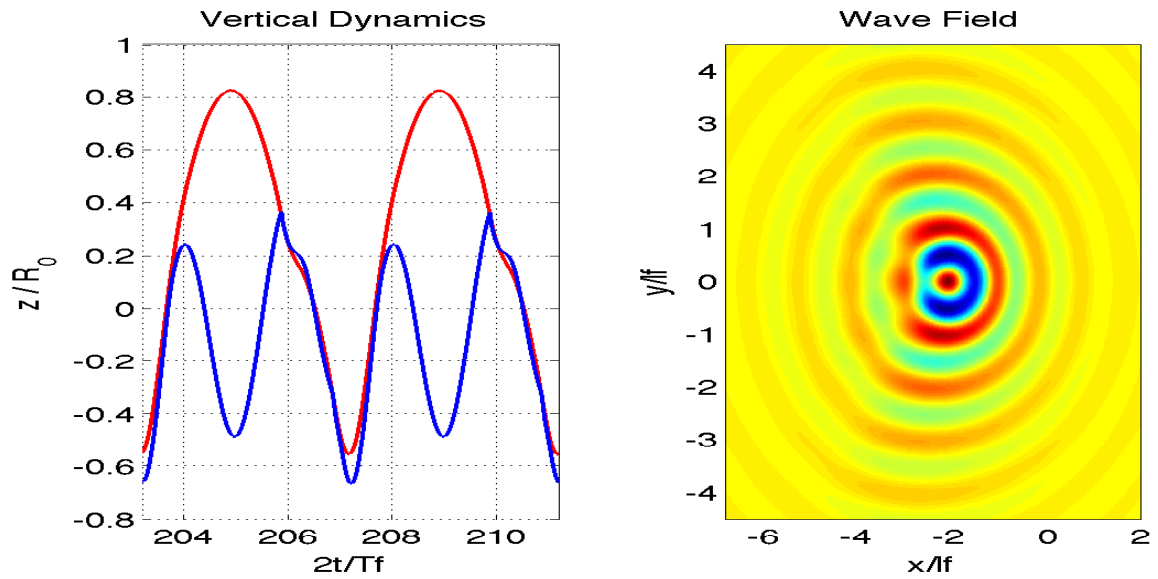
The main difference between the method of [19] and ours is the numerical routine used in computing the wave dynamics, in [19] a complexification of the water wave problem is introduced allowing the analytical integration of the Dirichlet to Neumann operator, surface tension and viscosity. This technique, introduced by Milewski in [20], does not carry over the case of a varying topography and so it was not implemented.

In place of the complexification technique, we used a fourth order Runge-Kutta method instead. However the surface tension term introduces stiffness in the problem forcing us to use a very small time step. This problem was overcome by switching from the fourth order Runge-Kutta routine to a Crank-Nicholson scheme and then another solution appeared by using an appropriate integration factor that let the surface tension and viscosity effects to be resolved analytically.

Our method captured walker regimes as shown in the bifurcation diagram in [19] and we are currently investigating other regimes of interest. We show in figures (4.1) and (4.2) two walking modes with their corresponding wave fields.

The  $x$  axis of the left panel of figures (4.1) and (4.2) is given in terms of forcing periods of the vibrating bath and the vertical axis is given in units of the drop radius  $R_0 = 0.38$  mm.

The right panel displays the wave field right before the drop hits the surface wave. The  $x$  axis and  $y$  axis are given in term of the Faraday wave length  $l_f = 0.5$  cm.

Fig. 4.1 A walker in the  $(2, 1)^2$  mode for  $\Gamma = 3.5$ .Fig. 4.2 A walker in the  $(2, 1)^2$  mode for  $\Gamma = 3.8$ .

# Chapter 5

## Conclusions and Future Applications

### 5.1 Conclusions

This thesis exploits the modeling capabilities provided by a new non-local formulation of the water wave problem that accounts for the interaction of a wave with arbitrary topographies. The non-local formulation we used was the one derived by Milewski in [18], where a formulation of the water wave problem in Fourier space was given. To the best of our knowledge no one has used this formulation to model linear fully dispersive waves under non-trivial topographies.

The non-local formulation led us to the development of an algorithm where the Dirichlet-to-Neumann operator was represented by means of a matrix decomposition that carries information about the vertical structure and the effects of the underwater topography. In this way the problem was reduced to the undisturbed free surface  $z = 0$ , and we got an efficient numerical routine.

We benchmarked our numerical algorithm with the conformal mapping technique and we obtained a very good agreement between both methods. However these comparisons were made in the two dimensional case because it is not possible to extend the conformal mapping technique to three dimensional topographies.

In the two dimensional case a similar non-local formulation was used by Vasan and Deconinck, see[24], in order to simulate waves over topographies. However we went one step forward by including periodic and rapidly varying topographies, a challenging configuration that has never been explored with this non-local formulation before.

By introducing periodic topographies we were able to capture the Bragg resonance phenomenon, our simulations were in agreement with the asymptotic theory of Mei, see [17], and we were able to compute the reflected wave with a wave number half of the wave number

of the bottom. Then we let the sinusoidal topography to vary rapidly entering into the regime where the Bragg resonance fades away giving rise to a homogenization of the wave field.

The homogenization phenomenon that arises when a wave moves over a rapidly varying topography was also captured by our simulations, moreover when we computed the speed of the wave we obtained that it was lower than the speed of the wave over a flat bottom configuration as the theory of Rosales and Papanicolaou predicts, see [23].

Chapter three of this thesis deals with the three dimensional problem, in this case, the theoretical results considering the wave-topography interactions are scarce so benchmarking our simulations was harder.

The simulations we made were meant to capture what is known as refraction of waves due to variations of the bottom topography. Our simulations captured how an incoming plane wave bends backwards as it passes over an underwater mountain, in accordance with Ray theory, then our simulations went one step further by showing how the interaction with a lens like obstacle is capable of focusing wave energy into a localized region.

We also made some simulations where the underwater obstacle was a hole instead of a mountain, in this case we capture how the incoming plane wavefront bends forwards, as Ray Theory predicts, and we capture a region of focalized wave energy around the edges of the cavity and not in front of it.

This thesis ends by exploring a new model that includes the interaction between a non linear three dimensional wave with a one dimensional topography, this non linear model is a generalization to the three dimensional case of the improved terrain following Boussinesq model of Nachbin and Muñoz, see [13], and to the best of our knowledge this is the first time a three dimensional non linear wave model with the topographic effects given by the conformal mapping theory of Nachbin, in [21], is proposed.

## **5.2 Future research.**

The list of problems and applications is very large however we mention what is coming next in our project.

### **5.2.1 Open questions**

There is a particular case of interest, from the point of view of applications, that can be explored with our three dimensional non-local method which corresponds to the interaction of waves with random topographies, for instance, in coastal regions the underwater topography is known in a statistical rather than deterministic way. The inclusion of statistical features

in the underwater topography allows for a more general model that can be used in a wider variety of cases.

A second case of interest is the inclusion of weaker non linear effects into our model as shown in the work of Milewski, [18], and Craig, Sulem, Nicholls and Guyenne, see [6]. In their work a weak non linearity can be included into the model by regarding the Dirichlet-to-Neumann operator as a first approximation of the normal velocity of the fluid along the free surface, the non linearity comes in by adding a first order correction term to the already computed vertical velocity of the fluid.

Regarding our three dimensional Boussinesq system, we can linearize it by letting  $\varepsilon \rightarrow 0$ , recovering a linear system of equations that models the interaction of a three dimensional wave with a one dimensional bottom topography, a case that can be simulated with our numerical non-local algorithm. It remains for future investigations to determine what features of the dynamics are kept in the reduced model and what other features would change.

We already know from the work of Artiles, see [2], that the wave front is well approximated by a Boussinesq system and discrepancies appear at the higher wave numbers, for example in the dispersive tail behind the head of the wave. This comparison was made for the flat bottom two dimensional case yet we expect a similar behavior because the Boussinesq system was derived as a long wave model.

Last but not least, for the bouncing droplet problem we have developed a numerical routine that is capable of modeling the effects of quite arbitrary topographies and we have adapted the technique of [19] so that it would be possible to include topographic effects into the modeling of bouncing drops and study their interactions with underwater obstacles.

# References

- [1] M. J. ABLOWITZ, A. S. FOKAS, AND Z. H. MUSSLIMANI, *On a new non-local formulation of water waves*, Journal of Fluid Mechanics, 562 (2006), pp. 313–343.
- [2] W. ARTILES, *Modelagem de ondas nao lineares atraves do operador Dirichlet-to-Neumann*, PhD thesis, IMPA, 2014.
- [3] K. A. BELIBASSAKIS AND G. A. ATHANASSOULIS, *Three-dimensional green's function for harmonic water waves over a bottom topography with different depths at infinity*, Journal of Fluid Mechanics, 510 (2004), pp. 267–302.
- [4] R. L. BURDEN AND J. D. FAIRES, *Numerical analysis*, Boston : PWS-Kent Pub. Co, 5th ed ed., 1993.
- [5] J. CHOI AND P. A. MILEWSKI, *Long nonlinear waves in resonance with topography*, Studies in Applied Mathematics, 110 (2003), pp. 21–47.
- [6] W. CRAIG, P. GUYENNE, D. NICHOLLS, AND C. SULEM, *Hamiltonian long-wave expansions for water waves over a rough bottom*, Proceedings of the royal society, 461 (2005), pp. 839–873.
- [7] B. DECONINCK AND K. OLIVERAS, *The instability of periodic surface gravity waves*, Journal of Fluid Mechanics, 675 (2011), pp. 141–167.
- [8] M. W. DINGEMANS, *Water wave propagation over uneven bottoms: Linear wave propagation*, vol. 13, World Scientific, 1997.
- [9] T. DRISCOLL, *The schwarz-christoffel toolbox for matlab*. <http://www.math.udel.edu/~driscoll/software/SC>.
- [10] A. EDDI, E. FORT, F. MOISY, AND Y. COUDER, *Unpredictable tunneling of a classical wave-particle association*, Physical review letters, 102 (2009), p. 240401.
- [11] L. EVANS, *Partial Differential Equations*, Graduate studies in mathematics, American Mathematical Society, 2010.
- [12] A. FOKAS AND A. NACHBIN, *Water waves over a variable bottom: a non-local formulation and conformal mappings*, Journal of Fluid Mechanics, 695 (2012), pp. 288–309.
- [13] J. C. M. GRAJALES AND A. NACHBIN, *Improved boussinesq-type equations for highly variable depth*, IMA journal of applied mathematics, 71 (2006), pp. 600–633.

- 
- [14] D. HIGHAM AND N. HIGHAM, *MATLAB Guide: Second Edition*, SIAM e-books, Society for Industrial and Applied Mathematics (SIAM, 3600 Market Street, Floor 6, Philadelphia, PA 19104), 2005.
- [15] R. JOHNSON, *A modern introduction to the mathematical theory of water waves*, vol. 19, Cambridge University Press, 1997.
- [16] D. LANNES, *Well-posedness of the water-waves equations*, Journal of the American Mathematical Society, 18 (2005), pp. 605–654.
- [17] C. C. MEI, *Resonant reflection of surface water waves by periodic sandbars*, Journal of Fluid Mechanics, 152 (1985), pp. 315–335.
- [18] P. A. MILEWSKI, *A formulation for water waves over topography*, STUDIES IN APPLIED MATHEMATICS, 100 (1998).
- [19] P. A. MILEWSKI, C. A. GALEANO-RIOS, A. NACHBIN, AND J. W. BUSH, *Faraday pilot-wave dynamics: modelling and computation*, Journal of Fluid Mechanics, 778 (2015), pp. 361–388.
- [20] P. A. MILEWSKI AND E. G. TABAK, *A pseudospectral procedure for the solution of nonlinear wave equations with examples from free-surface flows*, SIAM journal on scientific computing, 21 (1999), pp. 1102–1114.
- [21] A. NACHBIN, *A terrain-following boussinesq system*, SIAM J. APPL. MATH., 63 (2003), pp. 905–922.
- [22] O. NWOGU, *Alternative form of boussinesq equations for nearshore wave propagation*, Journal of waterway, port, coastal, and ocean engineering, (1993).
- [23] R. R. ROSALES AND G. C. PAPANICOLAOU, *Gravity waves in a channel with a rough bottom*, Studies in Applied Math., 68 (1983), pp. 89–102.
- [24] V. VASAN AND B. DECONINCK, *The inverse water wave problem of bathymetry detection*, Journal of Fluid Mechanics, 714 (2013), pp. 562–590.
- [25] G. B. WHITHAM, *Linear and Nonlinear Waves*, John Wiley & Sons, 1999.
- [26] J. WILKENING AND V. VASAN, *Comparison of five methods of computing the Dirichlet-Neumann operator for the water wave problem*, ArXiv e-prints, (2014).
- [27] S. WU, *Well-posedness in sobolev spaces of the full water wave problem in 3-d*, Journal of the American Mathematical Society, 12 (1999), pp. 445–495.

# Appendix A

The theory of refraction of linear water waves has been extensively studied in the literature under the name of geometric optics or ray theory. This asymptotic theory is obtained in the limit, when the wave varies on a length scale shorter than the typical scale of the topography in the shallow water regime.

We give a brief description of the theory, following the treatment given in [15].

First we introduce a small parameter  $\varepsilon$  and slow variables

$$X = \varepsilon x, \quad Y = \varepsilon y, \quad T = \varepsilon t. \quad (\text{A.1})$$

The parameter  $\varepsilon$  will control how slow are the variations on the length scale of the topography as compared to the variations on the wave field.

This theory is based upon the following description of a train of waves, a phase function  $\theta$  and an amplitude function  $A$ . The phase function tells us where the peaks and troughs of the wave are with regard to its level curves and the amplitude functions describes how large or small such vertical variations between crests and troughs are.

When the topography is flat, the linearized Potential Theory equations allows solutions in the form of monochromatic wave trains:

$$\varphi(x, y, z, t) = A e^{i(\mathbf{k} \cdot \mathbf{x} - \omega t)}.$$

This type of solutions have a constant amplitude  $|A|$  and a phase function  $\mathbf{k} \cdot \mathbf{x} - \omega t$ , that determine the solution completely.

In the context of slowly varying topography we use the following ansatz for the velocity potential:

$$\varphi(x, y, z, t) = A(X, Y, z, T) e^{i\theta(X, Y, t)/\varepsilon}. \quad (\text{A.2})$$

This ansatz for the velocity potential resembles a monochromatic wave train where the amplitude function is allowed to vary slower than the phase function  $\theta$ .

For this type of representations of the velocity potential it is usual to define a local wave number and a local frequency, see [25], as

$$k_1 = \theta_x(X, Y, T), \quad k_2 = \theta_y(X, Y, T), \quad w = -\theta_t(X, Y, T). \quad (\text{A.3})$$

And as usual we denote by  $\sigma = \|\mathbf{k}\| = \|(k_1, k_2)\|$ .

Then an asymptotic expansion for the amplitude function is used,

$$A = \sum_{n=0}^{\infty} \varepsilon^n A_n(X, Y, z, T). \quad (\text{A.4})$$

In the leading order approximation we obtain the following equations for  $A_0$ :

$$\begin{aligned} A_{0zz} - (k^2 + l^2)A_0 &= 0, \quad \text{in } -B(X, Y) < z < 0, \\ A_{0z} &= 0, \quad \text{on } z = -B(X, Y), \\ A_{0z} &= w^2 A_0, \quad \text{on } z = 0. \end{aligned}$$

The solution to these equations is given by

$$A_0(X, Y, z, T) = C(X, Y, T) \cosh(-\|k\|(z - B(X, Y))),$$

and the full dispersion relation for the slowly varying functions  $\mathbf{k}$ ,  $w$  and the varying bottom  $B$  must hold

$$w^2 = g\|\mathbf{k}\| \tanh(\|\mathbf{k}\|B). \quad (\text{A.5})$$

The second important equation that arises is a non linear hyperbolic equation of the form

$$\nabla w + \frac{\partial \mathbf{k}}{\partial T} = 0. \quad (\text{A.6})$$

This equation follows from the definition of local wave number and local frequency (A.3), it is a consistency condition that is necessary for the existence of the phase function  $\varphi$ .

It is interesting the fact that a simplified model out of a linear equation yields a *non-linear* hyperbolic equation.

The third equation is a statement about the conservation of the wave action. In oscillatory problems the wave action is defined as the ratio energy over frequency and in our case the energy is defined as

$$E = \frac{1}{2} w^2 A_0^2 \cosh^2(\|\mathbf{k}\|h). \quad (\text{A.7})$$

And the conservation equation is

$$\frac{\partial}{\partial T} \left( \frac{E}{w} \right) + \nabla \cdot \left( \frac{E}{w} \mathbf{c}_g \right) = 0. \quad (\text{A.8})$$

The derivation of this equation comes from the problem that determines the  $A_1$  function in the asymptotic expansion. The goal, by looking into the first order problem, is to determine the function  $C(X, Y, T)$  that appears in the solution for the leading amplitude coefficient  $A_0$ .

The derivation involves an integral equation which whose solution depends on the Fredholm alternative and can be found in [15].

In equation (A.8),  $\mathbf{c}_g = (\partial w / \partial k_1, \partial w / \partial k_2)$  is the group velocity, and this is the equation that actually allows the determination of the leading order approximation for the amplitude function. It states that the wave action is conserved as it is transported with group velocity.

From equations (A.6), (A.7) and (A.8) we are allowed to determine the unknown local wave numbers  $k_1, k_2$ , the local frequency  $w$  and the first approximation for the amplitude  $A_0$ .

In order to recover the phase function  $\theta$  we use the definition of local wave number (A.3) to get

$$\theta_x^2 + \theta_y^2 = k_1^2 + k_2^2. \quad (\text{A.9})$$

This is also a first order non linear partial differential equation known as the *eikonal* equation, it is an equation that allows the reconstruction of the phase function  $\theta$  given the function already determined local wave numbers  $k_1$  and  $k_2$ .